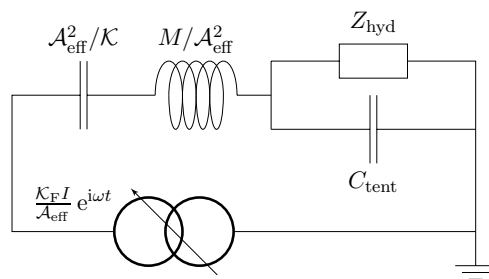
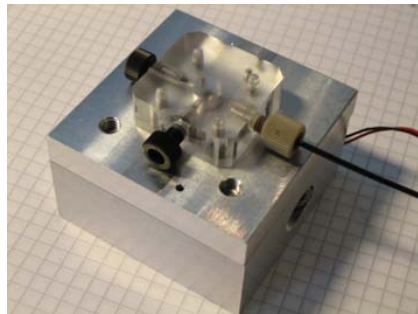


# Millisecond dynamics in microfluidics: Equivalent circuit theory and experiment

Søren Vedel



Supervisor:

Henrik Bruus  
Department of Micro- and Nanotechnology  
Technical University of Denmark

Industrial supervisor:

Laurits Højgaard Olesen  
Device Research and Technology  
Novo Nordisk A/S

February 17, 2009



# Abstract

A low-order modeling technique known as equivalent circuit (EC) theory is in widespread use within the field of microfluidics. Representing the studied microfluidic system as an equivalent electrical network due to mathematical similarity, the behavior of the fluidic system is found from simple ODEs rather than cumbersome field equations. This thesis suggests the exploitation of this analogy to the fullest, namely to use it as a predictive tool for deducing component or systems-level dynamics from simple experiments.

Currently, the equivalent circuit theory approach lacks experimental justification for dynamic systems, which is provided by this thesis for both the transient and pulsatile case. The origin of the circuit elements and their mathematical expressions have been derived from theoretical investigations of fluid mechanics, thermodynamics and solid mechanics, and a theoretical investigation of pulsatile flow in microfluidics revealed several interesting features including a frequency dependence of the resistance. Moreover, models of time-dependent viscous fluid flow (pulsatile and transient) in elastic tubes have been derived.

A pressure source capable of delivering a pulsatile pressure up to frequencies of 0.8 kHz has been developed based on a linear voice coil actuator. Using this, the pulsatile motion of an air bubble is studied and good agreement is found between EC model and experiment. The same is found for the transient flow in a highly elastic tube arising due to an abruptly started pressure difference.

The deduction of component dynamics from simple parameters failed, in part due to the presence of air bubbles, and in part because of an inadequate valve model. The proposed method still appears promising, although this first attempt clearly showed that much care must be taken for the method to work.



# Resumé

Til simpel analyse af mikrofluide systemer benyttes ofte en teknik kaldet ækvivalent kredsløbsteori, hvorved det modellerede system repræsenteres som et netværk af elektriske komponenter. Gyldigheden af metoden findes ud fra simple analyser af mikrofluide systemer samt antagelsen om inkompressibel strømning hvorved det kan vises, at disse systemer kan beskrives ud fra simple elementer, der er matematisk identiske til elektriske netværk. Opførslen af det mikrofluide system antages således at kunne bestemmes ud fra den matematiske løsning til det tilsvarende ækvivalente elektriske kredsløb, omend dette ikke er sandsynliggjort eksperimentelt. Det er målet med denne afhandling at bevise gyldigheden af metoden for både transiente og harmonisk oscillerende systemer, altså systemer hvor inertien ej kan negligeres.

Ud fra den analytiske løsning til harmonisk oscillerende strømning i stive rør udledes et ikke-lineært kredsløbselement, der er gyldigt for alle frekvenser. Der udledes desuden matematiske udtryk for eftergivigheden af elastiske vægge og luftbobler samt for den viskose modstand og de inertielle tab i Poiseuille strømning.

En konstrueret trykkilde baseret på en såkaldt lineær voice coil aktuator præsenteres, som kan levere pulserende tryk med frekvenser op til 0.8 kHz. Denne beskrives ud fra en simpel kredsløbsmodel, hvorved den kan kobles til de mikrofluide ligninger. Trykkilden er benyttet til at studere bevægelsen af en luftbobbel i frekvensintervallet 1-100 Hz, og det vises, at systemet kan beskrives fyldestgørende vha. ækvivalent kredsløbsteori. Det samme gør sig gældende for abrupt startet tryk-drevet strømning i et tyndvægget elastisk rør, hvor der også findes god overensstemmelse mellem den simple model og de eksperimentelle resultater.

Givet denne overensstemmelse foreslås i afhandlingens næstsidste kapitel at de dynamiske egenskaber af mikrofluide komponenter, så som eftergivighed (compliance) e.l., kan udledes fra studier af trykamplituden nedestrøms for komponenten som funktion af frekvens, meget lig metoderne kendt fra elektronikindustrien. Metoden illustreres med en kommercielt tilgængelig gummiventil (en såkaldt duckbill ventil), men dårlig overensstemmelse findes mellem de eksperimentelle resultater og modellen. Der argumenteres for den stadige gyldighed af metoden, men det erkendes, at dens anvendelse er sværere end oprindeligt antaget.



# Preface

This thesis is submitted in partial fulfillment of the requirements for the degree of Master of Science at the Technical University of Denmark. Its content is based on work carried out in the Theoretical Microfluidics (TMF) group at the Department of Micro- and Nanotechnology (DTU Nanotech) and in the Device Research and Technology unit of Novo Nordisk A/S, with a duration of 12 months corresponding to a credit of 50 ECTS points. It has emerged from a collaboration between these institutions entitled “Development and experimental verification of dynamic models of drug delivery systems”.

As much as I would like to pass this off as solely my work, many have contributed to the content. First, I wish to thank my advisors for their outstanding supervision, engagement (although not to each other) and seemingly limitless patience, as well as always finding the time to discuss any problems I encountered. Furthermore, I would like to express my gratitude to the manager of the Device Simulation and Prototyping department of the Device Research and Technology unit, Torben Storgaard-Larsen, for generous financial support and inclusion in the department. Henrik Ljunggren, Jan Jacobsen, Bo Bøgelund Pedersen, Ulrik Ullum, Lennart Berggren and Jan Lindhardt Petersen, all of Novo Nordisk, have provided invaluable assistance with the experimental work, for which I am truly indebted. Moreover, I would like to thank the TMF group for good discussions, encouragement and help when needed. During a one-year exchange study at Rensselaer Polytechnic Institute I worked in the experimental fluid mechanics group of Professor Timothy Wei; this experience taught me the process of scientific research in addition to the intricacies of experimental fluid dynamics, for which I am thankful. A grand and resounding “thanks” also goes to doctoral student Ben Cohen of this group for helping me with literature unavailable through domestic channels.

Finally, I wish to extend my thanks to family and friends for the toll the work of this thesis no doubt also has taken on them.

Søren Vedel  
Department of Micro- and Nanotechnology  
Technical University of Denmark  
February 17, 2009





# Contents

List of figures	xiv
List of tables	xv
List of symbols	xvii
<b>1 Introduction</b>	<b>1</b>
1.1 Time-dependent microfluidics . . . . .	1
1.2 Systems-level modeling in microfluidics . . . . .	2
1.3 Objective . . . . .	3
1.4 Notational convention . . . . .	3
1.5 Outline . . . . .	4
<b>2 Basics of microfluidics and equivalent circuit theory</b>	<b>5</b>
2.1 Fluid compressibility in kilohertz actuation . . . . .	5
2.2 Governing equations for fluid flow . . . . .	5
2.3 Pressure driven fluid flow . . . . .	6
2.3.1 Fluid flow driven by constant pressure gradient . . . . .	6
2.3.2 Pulsatile flow solution . . . . .	7
2.3.3 Notes on the Womersley number and its relation to the flow . . . . .	9
2.4 Equivalent circuit theory . . . . .	11
2.4.1 Inertia . . . . .	11
2.4.2 Compliance . . . . .	12
2.4.3 Coupling of several equivalent circuit components and applicability of the method . . . . .	13
2.5 Equivalent circuit description of Womersley flow . . . . .	13
2.5.1 Resistance in Womersley flow . . . . .	14
<b>3 Compliances and flow in elastic tubes</b>	<b>17</b>
3.1 Coupling compliance to flowrate and pressure . . . . .	17
3.2 Air bubble compliance . . . . .	18
3.3 Compliance of elastic vessels . . . . .	18
3.3.1 Effects of wall inertia . . . . .	19
3.3.2 Wall compliance . . . . .	19

3.4	Flow in elastic tubes . . . . .	21
3.4.1	Simple EC model . . . . .	21
3.4.2	Continuum model . . . . .	23
3.4.3	Continuum model in the pulsatile case . . . . .	24
3.5	Summary . . . . .	26
<b>4</b>	<b>Experimental flow in elastic tubes</b>	<b>27</b>
4.1	Measuring the hydraulic resistance of a tube . . . . .	27
4.1.1	Method . . . . .	28
4.1.2	Instrumentation . . . . .	28
4.1.3	Results . . . . .	29
4.1.4	Validation of result . . . . .	31
4.2	Transient build-up of pressure in an elastic tube . . . . .	32
4.2.1	Pressure generation considerations . . . . .	32
4.2.2	Experimental setup and procedure . . . . .	33
4.2.3	Instrumentation . . . . .	33
4.2.4	Equivalent circuit model of the system . . . . .	34
4.2.5	Statistical analysis . . . . .	35
4.2.6	Results . . . . .	36
4.3	Summary . . . . .	38
<b>5</b>	<b>The constructed pressure source</b>	<b>39</b>
5.1	Initial considerations . . . . .	39
5.2	Choice of actuator . . . . .	39
5.2.1	Actuator . . . . .	40
5.3	Pressure source design . . . . .	41
5.3.1	Holder and actuator guide . . . . .	42
5.3.2	Plunger . . . . .	43
5.3.3	Chamber . . . . .	43
5.4	Instrumentation used for driving the pressure source . . . . .	43
5.4.1	Electronics . . . . .	43
5.4.2	Data acquisition and handling . . . . .	44
5.4.3	Pressure detection . . . . .	44
5.5	Pressure source circuit model . . . . .	46
5.5.1	Coil mechanics . . . . .	46
5.5.2	Coil electric circuit . . . . .	47
5.5.3	Chamber fluidics . . . . .	47
5.5.4	Pulsatile case . . . . .	48
5.6	Pressure source performance . . . . .	48
5.6.1	Frequency capability . . . . .	49
5.6.2	Effective area $\mathcal{A}_{\text{eff}}$ . . . . .	49
5.6.3	Membrane spring stiffness $\mathcal{K}$ . . . . .	51
5.6.4	Membrane compliance $C_{\text{tent}}$ . . . . .	51
5.7	Summary . . . . .	52

<b>6</b>	<b>Pulsatile flow detected by bubble motion</b>	<b>55</b>
6.1	Experimental setup and method . . . . .	55
6.1.1	Setup . . . . .	55
6.1.2	Instrumentation . . . . .	56
6.1.3	Method . . . . .	57
6.2	Image processing routine . . . . .	57
6.2.1	Pixelation and resolution . . . . .	57
6.3	Motion of air-water interfaces . . . . .	59
6.3.1	Observed motion . . . . .	60
6.3.2	Physical interpretation of the observed motion . . . . .	60
6.4	Equivalent circuit model . . . . .	62
6.4.1	Model shortcomings . . . . .	65
6.4.2	Extending the model . . . . .	66
6.5	Comparison . . . . .	66
6.5.1	First attempt . . . . .	66
6.5.2	Correcting the model . . . . .	67
6.6	Summary . . . . .	70
<b>7</b>	<b>Characterization of component dynamics</b>	<b>71</b>
7.1	Proposed method . . . . .	71
7.2	An introduction to microvalves . . . . .	72
7.2.1	EC model . . . . .	73
7.3	Experimental method and setup . . . . .	74
7.3.1	Method . . . . .	74
7.3.2	Setup for pulsatile experiments . . . . .	74
7.3.3	Valve holder . . . . .	75
7.3.4	Steady state experiments leading to valve characteristics . . . . .	75
7.4	EC model . . . . .	77
7.5	Comparison . . . . .	78
7.5.1	Valve dynamics . . . . .	80
7.5.2	Frequency dependence . . . . .	82
7.5.3	Validation of method . . . . .	82
7.6	Summary . . . . .	84
<b>8</b>	<b>Conclusion and outlook</b>	<b>85</b>
8.1	Conclusion . . . . .	85
8.2	Outlook . . . . .	86
<b>A</b>	<b>Mathematical derivations for <math>Z_{\text{Wom}}</math></b>	<b>87</b>
A.1	Asymptotic behavior of $Z_{\text{Wom}}$ . . . . .	87
A.2	Dependence of $R_{\text{hyd}}^{\text{Wom}}$ on $\alpha$ . . . . .	88

---

<b>B</b>	<b>Additional topics in elastic tube flow</b>	<b>89</b>
B.1	Liquid compliance . . . . .	89
B.2	The Moens-Korteweg pressure equation . . . . .	90
B.3	Full solution to the governing fluid and solid equations . . . . .	90
B.3.1	Governing equations . . . . .	90
B.3.2	Boundary conditions . . . . .	91
B.3.3	Solving the fluid problem . . . . .	92
B.3.4	Solving the wall problem . . . . .	93
B.3.5	Determining the propagation constant $k_n$ . . . . .	95
B.4	The motion of the liquid . . . . .	97
B.4.1	Problems . . . . .	98
B.4.2	A note on turbulent pipe flow . . . . .	98
<b>C</b>	<b>BEI Kimco LA08-10-000A data sheet</b>	<b>99</b>

# List of Figures

2.1	Schematic of pulsatile flow . . . . .	8
2.2	Velocity profiles for Womersley flow for $\alpha_c = 1/5$ , $1, 5/2$ , and $5$ . . . . .	9
2.3	3D velocity profiles for Womersley flow for $\alpha_c = 5/2$ . . . . .	10
2.4	Hydraulic resistance in Womersley flow as a function of $\alpha_c$ . . . . .	16
3.1	Sketch of elastic tube for deriving $C_{\text{hyd}}$ for elastic walls . . . . .	19
3.2	Comparison of simple and corrected wall compliance for varied $h/a$ and Poisson ratio . . . . .	21
3.3	Three simple approaches for EC modeling of flow in elastic tubes . . . . .	22
3.4	Improved EC model of flow in elastic tube . . . . .	23
4.1	Measured viscosities . . . . .	30
4.2	Measurements of flowrate and pressure drop of a hollow glass fiber . . . . .	32
4.3	Experimental setup for transient Poiseuille measurements . . . . .	33
4.4	Measurement noise spectrum . . . . .	36
4.5	Transient Poiseuille flow results . . . . .	37
5.1	BEI Kimco LA08-10-000A voice coil actuator . . . . .	41
5.2	Working principle of the constructed pressure source . . . . .	41
5.3	Constructed pressure source . . . . .	42
5.4	The pressure source chamber . . . . .	43
5.5	LABVIEW program used for data acquisition . . . . .	44
5.6	Schematic illustration of the physical quantities in the pressure source circuit model . . . . .	46
5.7	EC diagram and symbol of pressure source . . . . .	49
5.8	Pressure source performance . . . . .	50
5.9	Measured pressure vs. DC coil current . . . . .	50
5.10	DC current vs. displacement of water front . . . . .	52
5.11	Experimental results for $C_{\text{tent}}$ . . . . .	53
6.1	Schematic illustration of the experimental setup used for the creation and detection of pulsatile bubble motion . . . . .	55
6.2	Example of raw bubble image . . . . .	56
6.3	Steps of the image processing routine . . . . .	58

6.4	Selected snapshots of bubble motion during one period at $f = 1$ Hz . . . . .	59
6.5	Motion of bubble interfaces as detected by the image processing routine . . .	61
6.6	Full EC model of bubble experiments . . . . .	64
6.7	Modeled bubble displacements using $C_{\text{sens}} = 1.67 \times 10^{-15} \text{ m}^3 \text{ Pa}^{-1}$ as estimated in sec. 5.4.3 . . . . .	67
6.8	Sensor pressure computed from EC model using electrical current . . . . .	68
6.9	Experimental and modeled bubble displacements with an added air bubble ( $C_{\text{sens}} = 4.10 \times 10^{-14} \text{ m}^3 \text{ Pa}^{-1}$ ) . . . . .	69
7.1	Duckbill valve . . . . .	72
7.2	EC model of elastomeric valve . . . . .	73
7.3	Experimental setup for pulsatile valve tests . . . . .	74
7.4	Duckbill valve holder . . . . .	75
7.5	Opening pressure of duckbill valve . . . . .	76
7.6	Compliance of duckbill valve . . . . .	77
7.7	EC model of pulsatile setup for the characterization of component dynamics	79
7.8	Pressures (measured and predicted) for downstream sensor . . . . .	81
7.9	Maximum pressure in sensors 1 and 2 as a function of frequency . . . . .	82
7.10	Frequency sweep of system without valve . . . . .	83

# List of Tables

2.1	Summary of equivalent circuit elements . . . . .	11
3.1	Properties for selected tube materials . . . . .	20
4.1	Relative deviations of the measured viscometer constants from the mean . .	29
4.2	Variations of the individual measurements and theoretical calculations of $R_{\text{hyd}}$ with temperature . . . . .	31
4.3	Values of EC elements for simple model of tube flow . . . . .	34
5.1	Results from simple experiment to determine pressure sensor compliance . .	45
6.1	Numerical values for circuit elements in simple EC model at $f = 1 \text{ Hz}$ . . .	63
7.1	Circuit elements for characterization of valve dynamic response . . . . .	78





# List of symbols

Symbol	Description	Unit
$\mathcal{A}$	Area	$\text{m}^2$
$\mathcal{A}_{\text{eff}}$	Effective area	$\text{m}^2$
$a$	Radius	$\text{m}$
$c$	Wave speed	$\text{m s}^{-1}$
$c_a$	Speed of sound	$\text{m s}^{-1}$
$\mathcal{D}$	Diffusivity	$\text{m}^2 \text{s}^{-1}$
$d$	Diameter	$\text{m}$
$E$	Young's modulus	$\text{Pa}$
$F$	Force	$\text{N}$
$f$	Frequency	$\text{Hz}$
$h$	Wall thickness	$\text{m}$
$I$	Electric current	$\text{A}$
$\mathcal{K}$	Spring constant	$\text{N m}^{-1}$
$\mathcal{K}_{\text{F}}$	Force constant	$\text{N A}^{-1}$
$\mathcal{K}_{\text{emf}}$	Back-EMF constant	$\text{N A}^{-1}$
$K_{\text{visc}}$	Viscometer constant	$\text{m}^4 \text{s}^{-2}$
$k$	Wave number	$\text{rad m}^{-1}$
$\ell$	Characteristic length	$\text{m}$
$M$	Plunger mass	$\text{kg}$
$N$	Number of pixels	pixel
$P$	Power	$\text{W}$
$p$	Pressure	$\text{N m}^{-2}$
$Q$	Volume flow rate	$\text{m}^3 \text{s}^{-1}$
$s$	Curve fit parameter	Varies
$q_{\text{el}}$	Electric charge	$\text{C}$
$\mathcal{T} = 1/f$	Period	$\text{s}$
$T$	Temperature	$\text{K}$
$U$	Voltage	$\text{V}$
$\mathbf{u}$	Displacement vector	$\text{m}$
$u$	Displacement	$\text{m}$
$\Delta u_v$	Valve opening height	$\text{m}$
$\mathcal{V}$	Volume	$\text{m}^3$
$\mathbf{v}$	Velocity vector	$\text{m s}^{-1}$
$v$	Velocity	$\text{m s}^{-1}$
$w$	Valve width	$\text{m}$

$\beta$	Wall compliance correction	
$\epsilon$	Relative error	
$\eta$	Dynamic viscosity	Pa s <sup>1</sup>
$\kappa$	Elastic constant	m Pa <sup>-1</sup>
$\lambda$	Wavelength	m
$\lambda_w$	Second Lamé coefficient	Pa
$\mu_w$	First Lamé coefficient	Pa
$\nu$	Kinematic viscosity	m <sup>2</sup> s <sup>-1</sup>
$\nu_w$	Poisson's ratio	
$\rho$	Mass density	kg m <sup>-3</sup>
$\tau$	Characteristic time	s
$\omega = 2\pi f$	Angular frequency	rad s <sup>-1</sup>
$C_{\text{hyd}}$	Compliance	m <sup>3</sup> Pa <sup>-1</sup>
$L_{\text{hyd}}$	Hydraulic inductance (inertia)	kg m <sup>-4</sup>
$R_{\text{hyd}}$	Hydraulic resistance	Pa m <sup>3</sup> kg <sup>-1</sup>
$Z_{\text{hyd}}$	Hydraulic impedance	Pa m <sup>3</sup> kg <sup>-1</sup>
$C_{\text{el}}$	Capacitance	C V <sup>-1</sup>
$L_{\text{el}}$	Electrical inductance	V s A <sup>-1</sup>
$R_{\text{el}}$	Electrical resistance	V A <sup>-1</sup>
$Re \equiv \rho \ell v / \eta$	Reynolds number	
$\alpha \equiv a \sqrt{\frac{\omega}{\nu}}$	Womersley number	
$\alpha_c \equiv \alpha / \gamma_1$	Critical Womersley number	
$\partial_i = \frac{\partial}{\partial i}$	Partial derivative with respect to direction $i$	
$\mathbf{e}_r, \mathbf{e}_\phi, \mathbf{e}_x$	Cylindrical unit vectors	
$(r, \phi, x)$	Cylindrical coordinates	
$y = r/a$	Non-dimensional radial coordinate	
$e$	Euler's number, ln(e)=1	
$\text{Re}[\dots]$	Real part of ...	
$\text{Im}[\dots]$	Imaginary part of ...	
$i$	Imaginary unit	
$J_n$	Bessel function of the first kind of order $n$	
$Y_n$	Modified Bessel function of the first kind of order $n$	
$\mathbf{n}$	Surface outward normal vector	
$\mathcal{O}(\dots)$	Order of ...	
$\gamma_n$	$n^{\text{th}}$ root of $J_0$	
$\langle \dots \rangle$	Time-average of ...	
$(\dots)^*$	Complex conjugate of (...)	
$\hat{\dots}$	... per unit length	
$\overline{\dots}$	Mean value of ...	
$ \dots $	Absolute value of ...	
$\tilde{\dots}$	Complex amplitude	

# Chapter 1

## Introduction

### 1.1 Time-dependent microfluidics

Microfluidics is the term used to describe fluid dynamics at the mm and sub-mm scale, although strictly speaking, the term only applies to flows in systems with a characteristic length scale of  $\mathcal{O}(1\text{ }\mu\text{m})$ . Fabricated microfluidic systems exploit the steady laminar flow properties to use a liquid as a transport medium for samples of e.g. biological material or liquid drug solutions, but capillary blood flow and other small-scale biological flows are also considered part of microfluidics. More advanced microfluidic systems known as “lab-on-a-chip” systems seek to miniaturize conventional laboratory equipment to produce a fully integrated analysis system on a single microchip. These chips combine microfluidics with microelectronics, optics, biotechnology and other scientific fields with the goal of mass-production of simple, reliable and disposable microchips with the potential to speed up the analysis while requiring much smaller sample sizes and eliminating the need for specialized laboratory personnel.

The inertial time-scale of microfluidics is approximately 1 ms and the viscous force dominates inertia, as will be shown in chapter 2, so the fluidics of most microfluidic systems operate in a steady state although time-dependent phenomena such as chemical reactions, diffusion, etc. still take place. Notable exceptions are pumps and valves along with AC electroosmosis and acoustofluidics<sup>1</sup>. Although the fluid can be thought of as quasi-static, full understanding and hence potential exploitation of the capabilities of a system cannot be achieved without considering the transient behavior. For a system of chemical reaction or a system delivering a liquid drug solution, knowing the exact amount delivered at any time is critical if the chemical system is to remain in equilibrium and the patient is to receive the correct amount of drug. Delivering too little and the chemical system/patient will not react as intended (cure in the patient’s case), while delivering too much may adversely affect the reaction or jeopardize the patient’s life. For systems performing more than one task, full understanding of the transient behavior is absolutely

---

<sup>1</sup>In both these cases, an AC phenomenon is used to generate a DC flow behavior, in an attempt to develop new pumping mechanisms for the disposable lab-on-a-chip systems: Acoustofluidics exploit the two forces arising when an acoustic field is applied to a liquid-filled microfluidic channel, see [1, 2], while AC electroosmosis uses the flow generated in an electrolyte by an applied electric voltage, see [3].

critical for the performance of the system; the success of the system of Thorsen et al, [4], consisting of 256 sub-nanoliter reaction chambers and 2056 microvalves, would not be possible without correct control of these valves and the flow around them. Apart from the few cases mentioned above, the field of time-dependent microfluidics is almost unexplored: This author has found only three accounts of the exploitation of such time-dependent effects, [5, 6, 7].

For a typical pressure driven microfluidic system consisting of elastic tubing, this elasticity of the fluid confinement along with the inertia and resistance of the fluid itself means that the system has several inherent characteristic time scales. These dynamic time scales set the upper limit on the time scale that can be probed by the system since for times faster than the slowest of these inherent time scales, the system has not reached equilibrium so the flow velocity will only reach a certain fraction of its maximum value. Thus, the correct prediction of these time scales is closely linked to the understanding of the transient behavior of the system.

A typical method for probing the dynamic time scale, in wide use in all branches of physics, is to expose the system to pulsatile<sup>2</sup> external fields. Unfortunately, the only work on pulsatile microfluidics into the inertially dominated region, i.e. the region where the inherent time scales of the system become important, appears to be by Morris and Forster, [8, 9], who considered a membrane pump and the flow it delivered. Reciprocating pumps are a large research field in itself and many theoretical investigations of the pulsatile flow delivered by such pumps in microsystems has been reported, e.g. [10, 11], but most are inadequate in their description of the fluid physics, as will be shown in chapter 2. Hence, even the basics of probing the time-dependence of microfluidics remains unexplored.

## 1.2 Systems-level modeling in microfluidics

A close mathematical similarity exists between electric circuits and low-order modeling of microfluidics, extending so far that the modeling technique is known as “equivalent circuit” (EC) modeling. In this lumped-parameter approach, the circuit elements represent viscous losses, inertial losses or compliance, which is sufficient to describe most flows. Such low-order models make obsolete the time-consuming numerical solution of the governing equations of fluid flow and are thus very attractive when developing microfluidic systems. Experimental and theoretical validation of the individual circuit elements is well-described, as is systems level modeling of steady state systems, e.g. [12], and while no such validation has been presented for dynamic systems, perfunctory use of the approach for time-dependent systems abounds, e.g. [6, 9, 10, 11, 13, 14, 15].

If valid, exploitation of the conceptual analogy to electronic circuits can be used to deduce the dynamic properties of microfluidic components. Not only will the computational time of a full numerical simulation be avoided in this case, but the parameters influencing component dynamics will be apparent and hence allowing for application-tuning of microfluidic components. One simple case has been reported, [6], where the compliance of a

---

<sup>2</sup>The word pulsatile will be used as a synonym to harmonically oscillating throughout the thesis to describe a temporal dependence of either  $\cos(\omega t)$  or  $\sin(\omega t)$ .

tube was deduced from the decay time of a pressure reading, but the analogy can be exploited much further by considering full systems and subsequently deducing the dynamic properties of any system component.

### 1.3 Objective

The current thesis has grown from a project entitled “Development and experimental verification of dynamic models of drug delivery systems”, with the goal of developing an experimental setup for the characterization of the dynamic properties of microfluidic components for Novo Nordisk A/S, while also devising simple yet accurate low-order models for the system. This setup would exploit the analogy to electronics to the fullest by deducing the characteristics from a comparison of EC model and experimental results.

The setup must deliver pulsatile pressures into the low kilohertz range to resolve the inertial time scale of about 1 ms previously alluded to. Given the lack of previous work in the field of pulsatile microfluidics, performance verification of the setup and thorough theoretical treatment of the fundamental physics are required, before turning the attention to the characterization of component dynamics. However, to get to this point, experimental verification of systems level EC modeling is necessary and will be provided.

The method will be applied to an elastomeric valve for illustration, but can be applied to any time-dependent component. No current method is able to predict the dynamic characteristics of a component from simple steady state variables, and the properties specified by the manufacturer are often insufficient for deriving these characteristics. It is hoped that the proposed method will be applied across the field in conjecture with systems-level EC modeling.

### 1.4 Notational convention

A consistent use of notation throughout the thesis has been attempted. Italics are used for scalar variables, such as the coordinate direction  $x$ , and bold face types for vectors, such as the velocity vector  $\mathbf{v}$ ; vector components are denoted by a coordinate subscript so that  $v_x$  is the velocity component in the  $x$ -direction. Exceptions are explicitly defined functions and operators, which are typeset in upright Roman type, e.g. the maximum operator  $\max$ . The shorthand notation  $d_S$  is used for derivatives with respect to some variable  $S$  of any function  $\varphi(S)$

$$d_S\varphi(S) \equiv \frac{d\varphi(S)}{dS}.$$

For partial derivatives this becomes  $\partial_S$ .

The author has adopted the convention of including radian in the unit for angular frequency and wave number, so that these have units  $[k]=\text{rad m}^{-1}$  and  $[\omega]=\text{rad s}^{-1}$ . Finally, relative error is denoted by  $\epsilon$ .

## 1.5 Outline

The work presented in the following is a selection of the work carried out during the project. The topics left out include various mathematical derivations, experimental verification of equipment and dynamics characterization of two Novo Nordisk components. In addition to this thesis, excerpts of chapter 2 have been presented at the Annual Meeting of the Danish Physical Society in June 2008.

The content of the following chapters is summarized in the following:

**Chapter 2** presents the theoretical background on which the thesis is built. The appropriate equations of fluid flow are introduced along with the basic solutions from which all thesis work is derived. Equivalent circuit modeling of microfluidic systems is derived and explained, and an EC description of pulsatile flow is presented. Most content of this chapter will be well-known to readers familiar with microfluidics.

**Chapter 3** is dedicated to the derivation of circuit elements specific to this work, namely the compliance of air bubbles and elastic walls. Pressure driven flow (both steady and pulsatile) in elastic tubes is discussed in the EC framework.

The experimental verification of the Hagen–Poiseuille law is presented in **chapter 4** along with the experimental investigation into the validity of an EC model of transient flow in an elastic tube. For this experiment, a Poiseuille flow is abruptly started in a water-filled thin-walled silicone rubber tube, and the pressure measured downstream of the pressure source. The model reproduces the experimental results, although there is not complete coincidence.

**Chapter 5** presents a pressure source developed for delivering pulsatile pressures into the low kilohertz range. The design and properties of the source are presented along with a low-order circuit model coupling the pressure source to the EC equations. Critical parameters for the model are determined from simple experiments.

The motion of an air bubble exposed to pulsatile pressures is studied in **chapter 6** as a test of the pressure source performance. The observed motion of the air-water interfaces are compared to the predictions of an EC model and good accordance is found.

The analogy between microfluidics and electronic circuits is exploited to the fullest in **chapter 7**, which details a method for the characterization of dynamics of microfluidic components based on pulsatile flow, much akin to the methods of component testing of electronics.

The thesis is rounded off with conclusions and outlook in **chapter 8**.

## Chapter 2

# Basics of microfluidics and equivalent circuit theory

### 2.1 Fluid compressibility in kilohertz actuation

When applying pressure fluctuations in the low kilohertz range the effects of acoustics must be considered. As argued by Landau and Lifshitz [16] the assumption of incompressibility is justified when the characteristic fluid velocity  $v$  is much smaller than the speed of sound  $c_a$  and if the characteristic dynamic length scale  $\ell_d$  is much smaller than the distance traveled by the sound waves during each oscillation cycle, i.e. the wavelength  $\lambda$ .

$$v \ll c_a, \quad (2.1a)$$

$$\ell_d \ll \lambda. \quad (2.1b)$$

Since the speed of sound can be rewritten as  $c_a = \lambda f$  where  $f$  is the frequency, eq. (2.1b) can be reformulated as

$$\ell_d \ll \frac{c_a}{f}. \quad (2.2)$$

The speed of sound in water at atmospheric pressure and 20 °C is  $c_a = 1483 \text{ m s}^{-1}$ , so the first criterion is inherently satisfied for all microfluidic systems with  $v \leq 1 \text{ m s}^{-1}$ . For a frequency of 1 kHz, the wavelength of the sound waves is  $\lambda \approx 1.5 \text{ m}$  while the characteristic length scale is  $\ell_d = \mathcal{O}(1 \times 10^{-3} \text{ m})$ , so the second criterion is also inherently satisfied. The assumption of incompressibility of water in kilohertz actuation is therefore valid.

### 2.2 Governing equations for fluid flow

Assuming the volume of fluid under consideration to have a characteristic length scale above  $\ell = 10 \text{ nm}$ , one can consider the fluid to be a continuum rather than consisting of a large but finite number of particles. Neglecting thermal effects, conservation of mass and momentum are sufficient to describe the fluid motion.

As argued in the previous section, the water of a microfluidic system in low kilohertz actuation may still be considered incompressible. Thus, conservation of mass is imposed

by the incompressible version of the so-called continuity equation, [1]:

$$\nabla \cdot \mathbf{v} = 0, \quad (2.3)$$

where  $\mathbf{v}$  is the fluid velocity.

The conservation of momentum for an incompressible and Newtonian fluid in a harmonically driven microfluidic system is given by the time-dependent Stokes equation, [1]

$$\rho \partial_t \mathbf{v} = -\nabla p + \eta \nabla^2 \mathbf{v}, \quad (2.4)$$

so long as the Reynolds number

$$Re \equiv \frac{\rho \ell v}{\eta}, \quad (2.5)$$

satisfies the condition  $Re < 1$ ;  $\rho$  denotes the density,  $v$  a characteristic scalar velocity,  $p$  the pressure and  $\eta$  the dynamic viscosity in these equations. The Reynolds number is a non-dimensional measure of inertial forces to viscous forces. Viscosity dominates at  $Re < 1$ , meaning that any perturbation to the velocity field quickly will be damped and the resulting flow is fully laminar. As the Reynolds number increases past 1 (but stays below 2000) inertial effects are no longer damped at the same rate so bends, kinks or other geometric changes to the confinement will introduce perturbations to the velocity field that are not immediately damped by the fluid viscosity. Overall the flow is still laminar, but inertial effects are not negligible. For  $Re \gtrsim 2300$  the fluid flow enters the turbulent regime where any perturbation in the velocity field may grow uncontrollably without immediate viscous damping, resulting in chaotic flow.

Gravity has been omitted from eq. (2.4) since the hydrostatic pressures on the millimeter and sub-millimeter scales are negligible compared to the externally applied pressure differences.

## 2.3 Pressure driven fluid flow

### 2.3.1 Fluid flow driven by constant pressure gradient

The analytical solution to the fluid flow driven by a constant pressure gradient is known as “Poiseuille” or “Hagen–Poiseuille” flow, and its derivation is thoroughly described in the literature, [1, 17, 18]. In a cylindrical reference frame away from tube inlet and outlet, the velocity field takes the form  $\mathbf{v}(r, \phi, x, t) \rightarrow v_x(r, t)\mathbf{e}_r$  under the assumption of azimuthal symmetry. The velocity in the start-up of such a fluid flow in a channel of circular cross-section of radius  $a$  and axial dimension  $\ell$ , where a pressure difference  $\Delta p$  is applied at  $x = 0$  is given by, [1]

$$v_x(r, t) = \frac{\Delta p a^2}{4\eta\ell} \left[ 1 - \frac{r^2}{a^2} - \sum_{n=1}^{\infty} \frac{8}{\gamma_n^3 J_1(\gamma_n)} J_0\left(\gamma_n \frac{r}{a}\right) \exp\left(-\frac{\gamma_n^2 \nu}{a^2} t\right) \right], \quad (2.6)$$

where  $J_s$  is the Bessel function of the first kind of order  $s$ ,  $\gamma_n$  are the roots to  $J_0$ , of which the first three are  $\gamma_1 = 2.4048$ ,  $\gamma_2 = 5.5201$  and  $\gamma_3 = 8.6537$  and  $\nu = \eta/\rho$  is the kinematic



viscosity. The steady state solution is obtained as time tends to infinity:

$$v_x(r, t) = \frac{\Delta p a^2}{4\eta\ell} \left(1 - \frac{r^2}{a^2}\right). \quad (2.7)$$

The volume flowrate<sup>1</sup> is defined as  $Q = \int_{\mathcal{A}} \mathbf{v} \cdot \mathbf{n} \, d\mathcal{A}$ , where  $\mathcal{A}$  is the cross-sectional area of the flow confinement and  $\mathbf{n}$  is an outward pointing normal vector. The flowrate in Poiseuille flow is

$$Q = \frac{1}{R_{\text{hyd}}} \Delta p, \quad (2.8)$$

where  $R_{\text{hyd}}$  is termed the hydraulic resistance, which for a tube of circular cross-section is given by, [1]

$$R_{\text{hyd}} = \frac{8\eta\ell}{\pi a^4}. \quad (2.9)$$

### Inertial time scale in Poiseuille flow

The analytical solution to the start-up of a Poiseuille flow, eq. (2.6), has an eigenfunction expansion which decays exponentially in time. The time constant for the  $n^{\text{th}}$  term in the expansion is

$$\tau_n = \frac{a^2}{\gamma_n^2 \nu}, \quad (2.10)$$

Since  $\gamma_n$ , the roots of  $J_0$ , appear in the denominator and  $\gamma_{n+1} > \gamma_n$  for all  $n$ , the first term of the expansion (that of  $n = 1$ ) last the longest. Thus, for a water-filled microfluidic system with  $a \approx 0.1 \text{ mm}$  and  $\nu \approx 10^{-6}$ , the flow reaches steady state on a time scale of

$$\tau \approx 1.7 \text{ ms}. \quad (2.11)$$

### 2.3.2 Pulsatile flow solution

The solution to flow in a straight tube of constant cross section exposed to a harmonically oscillating pressure gradient is usually credited to J. R. Womersley [19], although the problem also has been solved independently by S. Uchida [20], P. Lambossy [21] and T. SEXT [22].

The general setup differs from the regular Poiseuille problem only by the harmonically oscillating pressure difference,  $\Delta p \rightarrow \Delta p e^{i\omega t}$ , where the complex notation is used for convenience and  $\omega = 2\pi f$  is the angular frequency of the pressure oscillations. The actual, physical solution is found by taking the real part of the complex solution to the problem. The setup is sketched in fig. 2.1. The physics is described in a cylindrical reference frame  $(r, \phi, x)$  with  $x$  coinciding with the tube axis. Assuming no azimuthal dependence due to symmetry and fully developed flow so that  $\mathbf{v}(r, \phi, x, t) \rightarrow v_x(r, t)\mathbf{e}_r$ , the governing equation for the problem is

$$\rho \partial_t v_x(r, t) = -\partial_x p(x, t) + \eta \left[ \partial_r^2 + \frac{1}{r} \partial_r \right] v_x(r, t). \quad (2.12)$$

---

<sup>1</sup>The word ‘flowrate’ will be used throughout the thesis in the meaning volume flowrate.

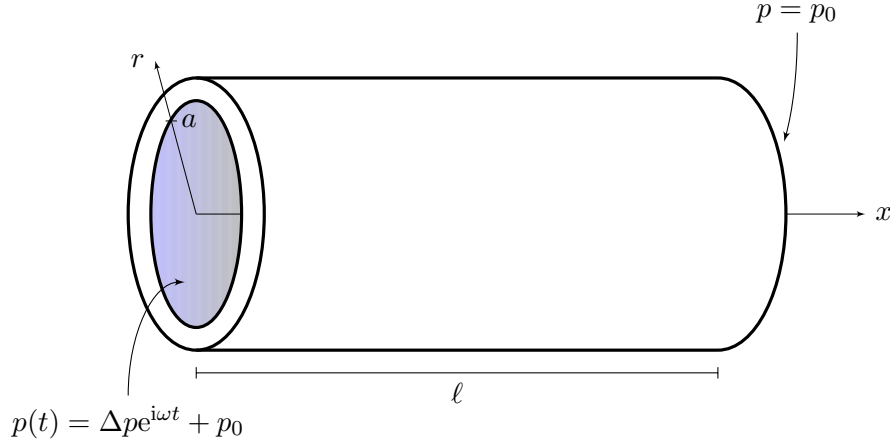


**Figure 2.1:** Schematic representation of pulsatile flow. The tube has inner radius  $a$  and axial dimension  $\ell$ .

The boundary conditions for the problem are the same as for the Poiseuille problem, only now with the harmonic oscillations of the applied pressure difference

$$p(0, t) = \Delta p e^{i\omega t} + p_0, \quad (2.13a)$$

$$p(\ell, t) = p_0, \quad (2.13b)$$

$$v_x(a, t) = 0, \quad (2.13c)$$

$$\partial_r v_x(0, t) = 0. \quad (2.13d)$$

Guessing of a harmonically oscillating solution void of start-up effects,  $v_x(r, t) = w(r) e^{i\omega t}$ , and inserting, one obtains a Bessel ODE for  $w(r)$ . Imposing the boundary conditions, the solution is found as:

$$v_x(r, t) = \frac{\Delta p}{i\rho\omega\ell} \left[ 1 - \frac{J_0\left(y\alpha i^{\frac{3}{2}}\right)}{J_0\left(\alpha i^{\frac{3}{2}}\right)} \right] e^{i\omega t}, \quad (2.14)$$

where the non-dimensional radial coordinate  $y = r/a$  has been introduced along with the Womersley number  $\alpha$  given by

$$\alpha \equiv \sqrt{\frac{a^2\omega}{\nu}}. \quad (2.15)$$

Examples of the velocity profiles at different values of the Womersley number is given in figs. 2.2 and 2.3, and the associated flowrate is found to

$$Q(t) = 2\pi \int_0^a v_x(r, t) r \, dr = \frac{\pi\Delta pa^2}{\rho i\omega\ell} \left[ 1 - \frac{2}{i^{\frac{3}{2}}\alpha} \frac{J_1\left(\alpha i^{\frac{3}{2}}\right)}{J_0\left(\alpha i^{\frac{3}{2}}\right)} \right] e^{i\omega t}. \quad (2.16)$$

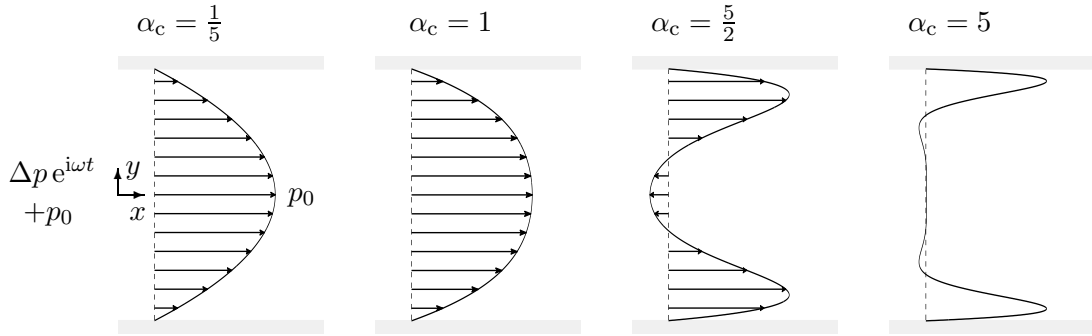


**Figure 2.2:** Snapshots of the velocity profiles for flow driven by a pulsatile pressure gradient at four values of the critical Womersley number  $\alpha_c = \alpha/\gamma_1$ , discussed in sec. 2.3.3. The snapshots are taken at the same time in the oscillation cycle, and the pressure differences are applied from left to right as shown for  $\alpha_c = 1/5$ , but are not drawn to scale. The full lines are the velocity profiles while the dashed lines mark the axial positions along which the velocities are obtained. The profiles oscillate harmonically in time, as shown in fig. 2.3 for  $\alpha_c = 5/2$ .  $\alpha_c$  strongly influences the profile shape.

### 2.3.3 Notes on the Womersley number and its relation to the flow

The Womersley number is a non-dimensional measure of the diffusion of momentum across the tube. The kinematic viscosity  $\nu$  is the diffusivity of momentum diffusion in Poiseuille flow, [1], while  $a^2\omega$  is the diffusivity required for the momentum to diffuse across the tube radius between pressure peaks. Thus, for  $\alpha \ll 1$  momentum has ample time to diffuse completely across the channel as in regular Poiseuille flow, while for  $\alpha > 1$  momentum does not have time to diffuse across the tube between pressure oscillations. Therefore, for  $\alpha \ll 1$  the velocity profile will be the regular Poiseuille parabola, while for  $\alpha > 1$  the profile will change since the no-slip boundary condition forces the velocity at the wall to be zero, while momentum does not have time to diffuse across the tube between pressure oscillations.

By considering the solution to the start-up of the Poiseuille problem, eq. (2.6), a critical Womersley number  $\alpha_c$  may be derived to determine the deviation from the Poiseuille parabola. Eq. (2.6) describes the time it takes the fluid to react to changes in pressure, given by the characteristic relaxation time for the fluid to reach a steady state  $\tau = a^2/(\gamma_1^2\nu)$ , as previously discussed. Thus, by defining the critical Womersley number as

$$\alpha_c \equiv \sqrt{\frac{a^2}{\gamma_1^2\nu}\omega} = \frac{\alpha}{\gamma_1}, \quad (2.17)$$

this is a measure of the fluid relaxation time versus the time scale of the pressure oscillations  $\omega$ .  $\alpha_c = 1$  marks the point where the fluid no longer has time to reach a steady state before the pressure varies, and the velocity profile begins to deviate from the Poiseuille parabola as shown in fig. 2.2. For  $\alpha_c \geq 1$  the flow never reaches a steady state before the pressure changes, so when the pressure gradient is reversed, the flow still has inertia acting in the opposite direction, and it will therefore take some time before the pressure gradi-

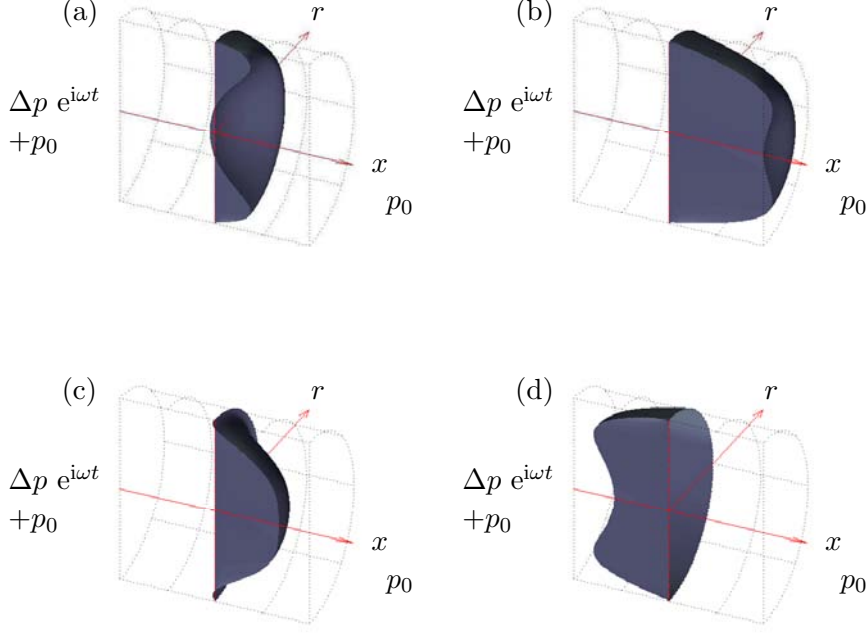


**Figure 2.3:** 3D snapshots of the velocity profile for Womersley flow for  $\alpha_c = 5/2$  taken at four different times over the oscillation period  $\mathcal{T}$  (plotted to scale). The pulsatile pressure gradient is applied from left to right in all snapshots; the profiles are only shown for half of the tube for clarity. The dotted black grid lines outline the tube wall and the full red lines the coordinate system; the velocity profiles of fig. 2.2 are obtained along the dashed red line. (a)  $t = 0$  (same as fig. 2.2). (b)  $t = \mathcal{T}/5$ . (c)  $t = 2\mathcal{T}/5$ . (d)  $t = 3\mathcal{T}/5$ .

ent can counteract and subsequently change the direction of the inertia. This introduces a phase-shift between the fluid and the pressure gradient. However, at the confinement walls, the no-slip boundary condition forces very low velocities with correspondingly low inertia, so fluid close to the walls have a smaller phase-shift than fluid in the center of the confinement, and at  $\alpha_c \gtrsim 5$  a full  $\pi/2$  phase-shift is observed between the flow close the walls and that at the center. These effects are observed in fig. 2.2: for  $\alpha_c < 1$  the normal Poiseuille parabola is retrieved, for  $\alpha_c > 1$  the profile deviates noticeably while at the critical value, the profile is almost parabolic.

As the critical Womersley number surpasses unity maximum velocity decreases, due to the constantly changing pressure gradient and the fact that there is a characteristic time needed to accelerate a fluid. The flowrate amplitude decreases accordingly so that less and less fluid is moved, until finally at high  $\alpha_c$  the fluid is completely dominated by inertia of constantly changing direction resulting in no fluid motion.

**Table 2.1:** Summary of equivalent circuit elements for microfluidic and electric circuits.

Fluidic circuits			Electric circuits		
Pressure drop	$\Delta p$	Pa	Voltage drop	$\Delta U$	V
Volume	$\mathcal{V}$	m <sup>3</sup>	Charge	$q_{\text{el}}$	C
Flowrate	$Q$	m <sup>3</sup> s <sup>-1</sup>	Current	$I$	C s <sup>-1</sup>
Resistance	$R_{\text{hyd}}$	Pa s m <sup>-3</sup>	Resistance	$R_{\text{el}}$	V A <sup>-1</sup>
Compliance	$C_{\text{hyd}}$	m <sup>3</sup> Pa <sup>-1</sup>	Capacitance	$C_{\text{el}}$	C V <sup>-1</sup>
Inertia	$L_{\text{hyd}}$	Pa s <sup>2</sup> m <sup>-3</sup>	Inductance	$L_{\text{el}}$	V s A <sup>-1</sup>

## 2.4 Equivalent circuit theory

Most branches of physics are governed by field equations, such as the Stokes equation, eq. (2.4), for fluid pressure and velocity in a microfluidic system, or Maxwell's equations for the electromagnetic fields. The recent advent of high-performance computing finally allows scientists to solve these field equations for (almost) arbitrary systems in reasonable time, but going back just two decades, such luxury was rarely allow mere mortals. Instead, several approximation techniques were developed yielding various degrees of accuracy. Among these is lumped-parameter modeling known from electric circuits, where the governing electromagnetic equations are supplanted by networks of idealized electric components, each exhibiting only one property, e.g. resistance or inductance. These low order models proved very effective in describing the observed effects and in addition have very attractive mathematical properties and highly intuitive applicability. Apart from electronics the lumped-parameter approach has also been successfully applied to thermal transport, optics, solid state mechanics, electron transport and acoustics.

Equivalent circuit theory in the context of microfluidics is such a lumped-parameter modeling approach. It derives its name from the 1:1 mathematical similarity between microfluidic components and the equivalent electronic component. The basic assumption of EC theory is that the flow is incompressible and pressure driven with  $Re < 1$ .

Eq. (2.8) forms the backbone of EC modeling of microfluidic systems. It predicts a linear relationship between an applied constant pressure difference  $\Delta p$  and the resultant flowrate  $Q$  as  $\Delta p = R_{\text{hyd}} Q$ . Comparing to Ohm's law which describes the drop in electrical potential,  $\Delta U$ , across a resistor with resistance  $R_{\text{el}}$  in which a current  $I$  is running, [23]

$$\Delta U = R_{\text{el}} I, \quad (2.18)$$

the analogy is obvious. However, the analogy extends further and also includes inertia and compliant effects of the fluid or its surroundings. The basic microfluidic components will be derived in the following, with a summary given in table 2.1.

### 2.4.1 Inertia

The hydraulic resistance is caused by the internal fluid friction known as viscosity, and is ultimately a result of the conversion of mechanical (kinetic) energy into heat, [1], just as

the Ohmic resistance in electric circuits is caused by the conversion of electrical energy into heat. As only steady state considerations led to the concept of hydraulic resistance, it does not account for inertial effects.

Consider a volume of fluid  $\mathcal{V}$  of density  $\rho$  confined in some geometry of constant cross-section of area  $\mathcal{A}$ , where  $\mathcal{V} = \ell \mathcal{A}$ . Assuming the only force acting on the fluid is a pressure difference  $\Delta p$  along the axis of  $\ell$  — and thus neglecting viscosity, which has already been accounted for in the hydraulic resistance — Newton’s second law reads  $F = m \, \mathrm{d}_t \bar{v}$ , where  $\bar{v}$  is the average velocity. With the pressure force and  $m = \rho \mathcal{A} \ell$  this becomes

$$\Delta p \mathcal{A} = \rho \mathcal{A} \ell \, \mathrm{d}_t \bar{v}, \quad (2.19)$$

and since  $\mathcal{A} \bar{v} = Q$ , one finds

$$\Delta p = L_{\text{hyd}} \mathrm{d}_t Q, \quad (2.20)$$

where the proportionality constant

$$L_{\text{hyd}} = \frac{\rho \ell}{\mathcal{A}}, \quad (2.21)$$

is termed the “hydraulic inductance”, since the following holds for an inductor with inductance  $L_{\text{el}}$  in an electrical circuit, [23]

$$\Delta U = L_{\text{el}} \mathrm{d}_t I. \quad (2.22)$$

As expected, inertia in EC theory is found to be a time-dependent phenomena giving rise to a pressure drop.

### 2.4.2 Compliance

The term compliance is used to describe any deviation from incompressibility in the fluidic system, i.e. compressibility of the liquid, any trapped air bubbles or the yielding of the confinement caused by a pressure increase. Following [1], any compliance in the fluidic system is defined as the negative change in volume with a change in pressure:

$$C_{\text{hyd}} = -\frac{\mathrm{d}\mathcal{V}}{\mathrm{d}p}. \quad (2.23)$$

Again, an exact electric equivalent exists namely the capacitor, which stores charge in the circuit. It is characterized by its capacitance  $C_{\text{el}}$ , which is a measure of the capacitor’s ability to store charge and is defined by, [23]

$$C_{\text{el}} = \frac{\mathrm{d}q_{\text{el}}}{\mathrm{d}U}, \quad (2.24)$$

where  $q_{\text{el}}$  is the electric charge. Hydraulic compliance can be thought of as a storage of volume in the hydraulic circuit since change in pressure will cause a change in volume according to eq. (2.23), just as capacitance is a storage of electric charge.

### 2.4.3 Coupling of several equivalent circuit components and applicability of the method

Due to the assumption of  $Re < 1$ , the governing equation — the Stokes equation — is linear and superposition is valid. Hence, if the fluid in a system experiences e.g. both resistance and inertia, the two elements (resistor and inductor) are simply superposed to describe the physics. In the EC framework this is a series coupling. Moreover, if fluid flow branches off (e.g. in a T-junction) the total flowrate leaving and entering the junction must be identical because of the assumption of incompressible flow. These simple arguments illustrate the EC framework: understanding a microfluidic system as a network of parameters. The two arguments for series and parallel coupling are identical to Kirchhoff's laws from electric circuits, so Kirchhoffian network analysis is applied to EC models of microfluidics, and it is customary to represent the system using a diagram of the EC network.

For  $Re \not\ll 1$ , perturbations to the flow are not readily damped out so the assumption of fully axial flow underlining the idealized Poiseuille and Womersley solutions of sec. 2.3 are violated and losses not included in the models will be inflicted on the fluidic system. Consequently, the method is only applicable for microfluidics or the fluid flow of very low velocity usually referred to as “creeping flow”, [18].

## 2.5 Equivalent circuit description of Womersley flow

In addition to viscous drag, Womersley flow also has a ever-present inertial contribution because of the pulsatile pressure gradient, and the simplest EC model of this flow would therefore consist of a linear combination of resistance and inductance. Using complex notation and assuming all fields oscillate harmonically one finds the following relation for the amplitudes

$$\Delta p = (R_{\text{hyd}} + i\omega L_{\text{hyd}}) Q, \quad (2.25)$$

or, introducing the notion of hydraulic impedance,  $\Delta p = Z_{\text{hyd}} Q$ , where  $Z_{\text{hyd}} = R_{\text{hyd}} + i\omega L_{\text{hyd}}$ . Noting the proportionality between the pressure gradient amplitude and flowrate in Womersley's solution, a correct impedance for pulsatile flow certain to include all inertial and resistive effects is found directly from eq. (2.16) as

$$Z_{\text{Wom}} = \frac{\rho\omega\ell}{\pi a^2} i \left[ 1 - \frac{2 J_1 \left( \alpha i^{\frac{3}{2}} \right)}{i^{\frac{3}{2}} \alpha J_0 \left( \alpha i^{\frac{3}{2}} \right)} \right]^{-1}, \quad (2.26)$$

where the subscript ‘Wom’ is introduced to distinguish from a “regular” fluidic impedance, such as  $Z_{\text{hyd}} = R_{\text{hyd}} + i\omega L_{\text{hyd}}$  above. Upon the introduction of this impedance, this author later found that Morris and Forster already has introduced it, [9].

The simple impedance of pulsatile flow  $Z_{\text{hyd}} = R_{\text{hyd}} + i\omega L_{\text{hyd}}$  and  $Z_{\text{Wom}}$  both predict dominating inertia with increasing frequency (and thus increasing Womersley number  $\alpha$ ). This is obvious for the simple case, and becomes apparent for  $Z_{\text{Wom}}$  by using the asymptotic expansion for  $J_n$  for large arguments and in turn the first two terms of a series

expansion of cosine for both  $J_0$  and  $J_1$  in eq. (2.26), see appendix A. The fraction in the square bracket of eq. (2.26) then becomes to second order accuracy

$$\frac{2 J_1 \left( \alpha i^{\frac{3}{2}} \right)}{i^{\frac{3}{2}} \alpha J_0 \left( \alpha i^{\frac{3}{2}} \right)} \approx \frac{2}{\alpha i^{\frac{3}{2}}}. \quad (2.27)$$

Noting that the prefactor to eq. (2.26) is in fact  $i\omega L_{\text{hyd}}$  for a tube of circular cross section, the full equation for  $Z_{\text{Wom}}$  may now be rewritten as

$$Z_{\text{Wom}} = i\omega L_{\text{hyd}} \frac{1}{1 - \frac{2}{\alpha i^{\frac{3}{2}}}}. \quad (2.28)$$

The fraction tends to unity as  $\omega \rightarrow \infty$  since  $\alpha \propto \sqrt{\omega}$ . Hence, both the simple and the Womersley impedances become increasingly dominated by inertia as the frequency is increased, which should come as no surprise, given sec. 2.3.3. However, it is noteworthy that the simple expression for inertia in Poiseuille flow also appears in the EC description of Womersley flow.

### 2.5.1 Resistance in Womersley flow

Following the arguments in [1], the time rate of change of the dissipation of mechanical energy into heat (which is the fluidic power consumption due to viscosity, i.e. the amount of kinetic energy converted to heat) for a fluidic system consisting of tubes of circular cross section of radius  $a$  and total length  $\ell$  is given by

$$P = \partial_t W_{\text{visc}} = 2\pi\ell\eta \int_0^a [\partial_r v_x(r, t)]^2 dr = Q(t) \Delta p(t). \quad (2.29)$$

For Poiseuille flow, the relation between power consumption and resistance is found by rearranging and inserting eq. (2.8) to obtain

$$P = \frac{\Delta p^2}{R_{\text{hyd}}^{\text{Pois}}}, \quad (2.30)$$

where the superscript ‘Pois’ is included to remind the reader of the temporal behavior of the pressure.

Because of its pulsatile behavior, the time-averaged resistance over an oscillation period for Womersley flow is the proper measure of resistance; this in turn, is calculated from the time-averaged hydraulic power consumption. To compute the time-average over one period of the product of two harmonically oscillating quantities  $f(t)$  and  $g(t)$ , where  $f(t) = \tilde{f} e^{i\omega t}$  and  $g(t) = \tilde{g} e^{i\omega t}$  and  $\tilde{f}$  and  $\tilde{g}$  are the complex amplitudes, one relies on the following classical theorem from complex analysis:

$$\langle f(t)g(t) \rangle = \frac{1}{2} \text{Re} \left[ \tilde{f} \tilde{g}^* \right], \quad (2.31)$$



where the asterisk indicates the complex conjugate and the brackets  $\langle \rangle$  the time-average over one period. Hence, the time-averaged fluidic power consumption in Womersley flow is

$$\langle P \rangle = \frac{1}{2} \text{Re} \left[ \tilde{Q} \Delta p^* \right], \quad (2.32)$$

where  $\tilde{Q}$  is the complex amplitude of the pulsatile flowrate,  $Q(t) = \tilde{Q} e^{i\omega t}$  and  $\Delta p$  is the (real) amplitude of the applied oscillatory pressure<sup>2</sup>,  $\Delta p(t) = \Delta p e^{i\omega t}$ . Since in general  $\tilde{Q} = \Delta p / Z_{\text{hyd}}$ , eq. (2.32) may be rewritten as

$$\langle P \rangle = \frac{1}{2} \text{Re} \left[ \frac{1}{Z_{\text{Wom}}} \right] \Delta p^2. \quad (2.33)$$

The difference from a regular equivalent circuit resistance derived from Poiseuille flow is found by inserting the same pressure difference in the two expressions. Thus, inserting the root mean square pressure amplitude<sup>3</sup>  $\Delta p_{\text{rms}} = \Delta p / \sqrt{2}$  into the expression for the power consumption in Poiseuille flow, eq. (2.30), one finds

$$P = \frac{1}{2} \frac{\Delta p^2}{R_{\text{hyd}}^{\text{Pois}}}. \quad (2.34)$$

Comparing eqs. (2.33) and (2.34), the hydraulic resistance for Womersley flow may be obtained as

$$R_{\text{hyd}}^{\text{Wom}} = \frac{1}{\text{Re} \left[ \frac{1}{Z_{\text{Wom}}} \right]}. \quad (2.35)$$

Unlike the hydraulic resistance of Poiseuille flow,  $R_{\text{hyd}}^{\text{Wom}}$  is frequency dependent since  $Z_{\text{Wom}}$  has this property. This result has been presented by Zielke in his dissertation<sup>4</sup>, [24], and hinted at by Uchida, [20], although he only focused on the excess work of pulsatile flow. The time-averaged Womersley resistance normalized by the Poiseuille resistance is shown in fig. 2.4(a) as a function of the critical Womersley number. The Poiseuille and Womersley resistances agree until  $\alpha_c \approx 1/\gamma_1$  (equivalent to  $\alpha = 1$ ), whereafter the Womersley resistance increases because of the increasing velocity profile gradients as already shown in fig. 2.2. At  $\alpha_c \geq 1$ , i.e. from the point where the velocity profile begins to deviate noticeably from the Poiseuille parabola, the resistance is proportional to  $\alpha_c^3$ ; a mathematical derivation of this dependence is given in appendix A.

The velocity profile gradient and thus the hydraulic resistance increases with the Womersley number<sup>5</sup>, while the profile itself is confined to an increasingly more narrow band close to the confinement walls. Again is a similar effect observed in AC electric circuits where the effective resistance increases with frequency caused by a decrease of the electric current density away from the surface of the conductor. Even though the effects are caused by different physical phenomena, it is remarkable that the hydraulic analogies extend as far as a increasing resistance in AC flow caused by a “hydraulic skin effect”.

<sup>2</sup>The pressure amplitude may, of course, be complex as a consequence of a phase-shift, however, when considering a single tube, any phase-shift is removed so that the pressure amplitude is a real number.

<sup>3</sup>By the mathematical similarity to voltage the root mean square of  $p(t) = \Delta p e^{i\omega t}$  is  $\Delta p_{\text{rms}} = \Delta p / \sqrt{2}$ .

<sup>4</sup>His results are expressed in a somewhat different form.

<sup>5</sup>And thus the critical Womersley number.

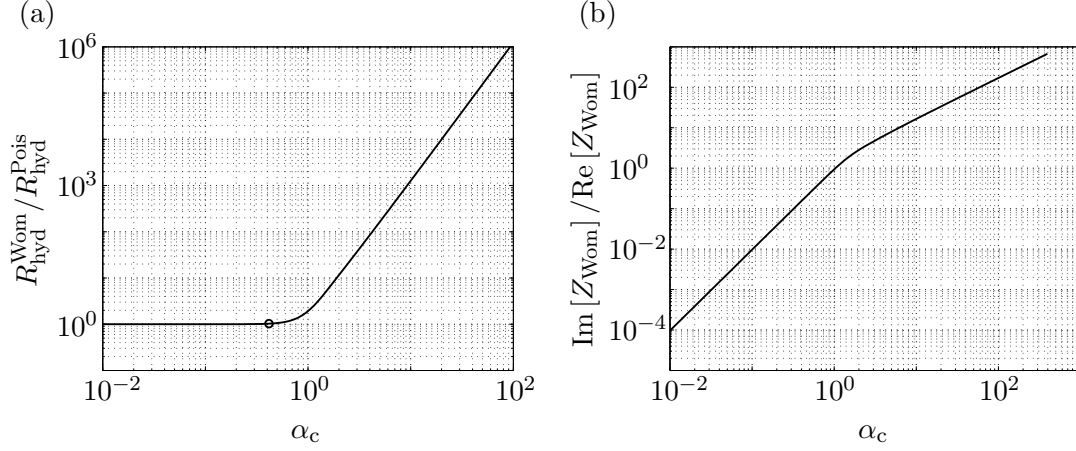


**Figure 2.4:** (a) Hydraulic resistance in Womersley flow normalized by the regular Poiseuille resistance. For  $\alpha_c < 1/\gamma_1$  the Poiseuille and Womersley resistances are identical, but for  $\alpha_c > 1/\gamma_1$  the Womersley resistance increases due to the change in velocity profile gradient. The circle marks the point of  $\alpha = 1$  where the resistance begins to deviate from the hydraulic resistance of Poiseuille flow.  $\alpha_c = 1$  is observed to mark the onset of the regime regime of  $R_{\text{hyd}}^{\text{Wom}} \propto \alpha_c^3$ . (b) Inertial contribution to  $Z_{\text{Wom}}$  divided by the resistive contribution as a function of  $\alpha_c$ . As expected, the two are identical for  $\alpha_c = 1$ . The decrease in slope above  $\alpha_c = 1$  is caused by the frequency dependence of the resistive contribution shown in (a).

### Resistance to inertia measured by $\alpha_c$

It was argued in sec. (2.3.3) that  $\alpha_c = 1$  marked the point where the fluid no longer has time to reach a steady state before the pressure varies, and the velocity profile begins to deviate from the Poiseuille parabola, that is, when inertial effects begin to be on the same order as the resistive effects. With the EC formalism in place, it is evident from the simple hydraulic resistance for Womersley flow,  $Z_{\text{hyd}} = R_{\text{hyd}} + i\omega L_{\text{hyd}}$ , that the resistive losses inflicted by the flow at any point in time are found as the real part of the impedance and the inertial losses are the imaginary part of the impedance. These resistive effects should not be confused with the time-averaged resistance derived above, which compares the effective resistive loss over one oscillation period to the loss the system would have experienced, had the pressure gradient been constant in time.

Fig. 2.4(b) shows the imaginary part of  $Z_{\text{Wom}}$  normalized by its real part, as a measure of the ratio of inertial to resistive effects in the flow. The resistive effects dominate for  $\alpha_c < 1$  while inertia dominates for  $\alpha_c > 1$  and the two effects are identical for  $\alpha_c = 1$ . This is further proof that  $\alpha_c$ , and not Womersley's  $\alpha$ , is the proper measure for describing the behavior of the flow. The decrease in slope for their ratio above unity is caused by the frequency dependence of the resistance.

## Chapter 3

# Compliances and flow in elastic tubes

The results of sec. 2.3 are only valid for flow in infinitely stiff tubes which is unfortunately a case rarely encountered. Most tubing has some compliance stemming from the elasticity of the tube wall, which not only will cause the flow to deviate from the idealized solutions, but also will introduce new time scales to the physics. These effects must be accounted for if one is to deduce the dynamic response of a component inserted into the system.

The first part of this chapter is devoted to the derivation of appropriate circuit elements, to be used in EC analysis in the following work, while two new equations along with modeling techniques for elastic tubes will be presented in the second part. Additional work in this field not relevant for the thesis is included in appendix B for the benefit of future students.

### 3.1 Coupling compliance to flowrate and pressure

Consider a compliant medium in a liquid-filled microfluidic system. Assuming the volume of the medium obeys a thermodynamical equation of state as

$$\mathcal{V}_{\text{med}} = \mathcal{V}_{\text{med}}(p_{\text{med}}), \quad (3.1)$$

which is the case for e.g. air and linearly elastic solids, the medium will expand when a pressure difference is applied across it. This change in medium volume will be filled with a flow of incoming liquid, so the negative time-rate of change of volume of the medium equals a positive liquid flowrate

$$Q_{\text{liq}} = -\frac{d\mathcal{V}_{\text{med}}}{dt}, \quad (3.2)$$

since  $Q_{\text{liq}} = d_t \mathcal{V}_{\text{liq}}$ . The chain-rule of differentiation yields

$$Q_{\text{liq}} = -\partial_p \mathcal{V}_{\text{med}} \partial_t p_{\text{med}}, \quad (3.3)$$

where the factor  $-\partial_p \mathcal{V}_{\text{med}}$  is recognized as the definition of compliance, so eq. (3.1) may be reformulated as

$$Q_{\text{liq}} = C_{\text{hyd}} \partial_t p_{\text{med}}. \quad (3.4)$$

### 3.2 Air bubble compliance

If present in the microfluidic system, air bubbles are often the most compliant parts, and as any experimentalist working in the field of microfluidics can attest to, air bubbles seem to always find ways to get stuck inside the system. Furthermore, the laminar flow conditions makes air bubble removal a daunting task.

Assuming the isothermal ideal gas law applies to the air bubbles, the product of the bubble volume and pressure is constant,  $p\mathcal{V} = p_0\mathcal{V}_0$ , where the subscript ‘0’ indicates a reference state. The compliance of the air bubble is then

$$C_{\text{hyd}} = -\partial_p \frac{p_0\mathcal{V}_0}{p} = \frac{p_0\mathcal{V}_0}{p^2}. \quad (3.5)$$

Expanding the bubble pressure in a Taylor series about  $p_0$  one finds to lowest order

$$C_{\text{hyd}} \approx \frac{\mathcal{V}_0}{p_0}. \quad (3.6)$$

Changes to the bubble volume removes it from thermal equilibrium and the isothermal version of the ideal gas law only applies to systems, in which the heat generated by the bubble volume change is transported away from the system on time scales significantly faster than the time scale of the volume changes. The temperature difference between the bubble and the surrounding liquid reaches equilibrium as a decaying exponential with time constant

$$\tau = \frac{\rho C_{\text{th}} \ell_{\text{th}}^2}{\kappa_{\text{th}}}, \quad (3.7)$$

according to [25]. Here,  $\rho$  is the density of the surrounding liquid and  $\ell_{\text{th}}$  the characteristic length of the conduction path, while  $C_{\text{th}}$  is the specific heat and  $\kappa_{\text{th}}$  the thermal conductivity. Typical values for air in water at room temperature in a microfluidic system are  $\rho = 998 \text{ kg m}^{-3}$ ,  $C_{\text{th}} = 4.2 \times 10^{-3} \text{ J kg}^{-1}$ ,  $\ell_{\text{th}} = 0.5 \times 10^{-4} \text{ m}$  and  $\kappa_{\text{th}} = 56.1 \times 10^{-2} \text{ W m}^{-1} \text{ K}^{-1}$  leading to a characteristic time of  $\tau \approx 2 \times 10^{-8} \text{ s}$ . Thus, the volume changes to a small bubble in a microfluidic system can be considered isothermal for a pulsating pressure even in the low kilohertz range.

At the other extreme, where the time scale of the volume change is significantly faster than the time scale of the heat transfer, the adiabatic version of the ideal gas law applies with  $p\mathcal{V}^\gamma = p_0\mathcal{V}_0^\gamma$  where  $\gamma = c_p/c_v$  is the ratio of specific heats, so  $C_{\text{hyd}} \approx \frac{\mathcal{V}_0}{\gamma p_0}$ .

### 3.3 Compliance of elastic vessels

Consider one half of a linearly elastic tube of Young’s Modulus  $E$ , circular cross section of inner radius  $a$ , thickness  $h$ , and axial length  $\ell$ , see fig. 3.1. Inside the tube, an added pressure  $p$  works to expand it while the wall stress counteracts the tube radial expansion.

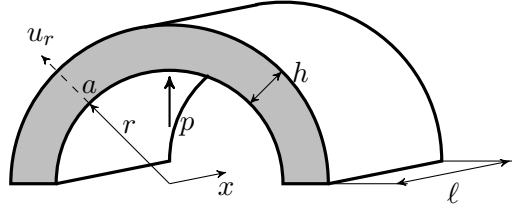


**Figure 3.1:** Sketch of the upper half of a segment of elastic tube of axial length  $\ell$ , inner radius  $a$  before pressure is applied and wall thickness  $h$ . The pressure  $p$  from the liquid acts on the tube walls which have Young's Modulus  $E$ .

### 3.3.1 Effects of wall inertia

Assuming only radial wall displacements, the displacement field becomes  $\mathbf{u}(r, \phi, x, t) = u_r(r, t) \mathbf{e}_r$  in a cylindrical reference frame and the elastodynamic equation governing  $\mathbf{u}$  for an arbitrary wall thickness  $h$  is, [26]

$$\rho_w \partial_t^2 \mathbf{u} = (2\mu_w + \lambda_w) \nabla^2 \mathbf{u}, \quad (3.8)$$

where  $\rho_w$  is the wall density and  $\mu_w$  and  $\lambda_w$  are the Lamé coefficients, which in terms of Young's Modulus and Poisson's ratio  $\nu_w$  are given by

$$\mu_w = \frac{E}{2(1 + \nu_w)}, \quad (3.9a)$$

$$\lambda_w = \frac{E\nu_w}{(1 + \nu_w)(1 - 2\nu_w)}. \quad (3.9b)$$

Eq. (3.8) is recognized as the regular wave equation with wave speed  $c = \sqrt{(2\mu_w + \lambda_w) / \rho_w}$ , and the wave will traverse the tube radius in the time  $t = h/c$ . With the parameters listed in table 3.1 and a wall thickness of  $h \approx 5 \times 10^{-4}$  m, the time for the motion of the wave across the wall thickness ranges from  $t \approx 2.86 \times 10^{-6}$  s for silicone rubber to  $t \approx 2.10 \times 10^{-7}$  s for PEEK<sup>1</sup>. Pressure oscillations in the low kilohertz regime will thus be several orders of magnitude slower than the time it takes for the wall to reach its equilibrium position as a result of the change in fluid pressure and consequently, the inertia of the wall may be neglected.

### 3.3.2 Wall compliance

Since wall inertia can be neglected, only the solution to the associated equilibrium equation to eq. (3.8) is needed to derive a wall compliance. Under the assumption  $\mathbf{u} = u_r(r) \mathbf{e}_r$  with the pressure  $p$  inside the tube, the solution to this equilibrium equation is given by Lautrup, [29]

$$u_r(r) = (1 + \nu_w) \left[ (1 - \nu_w) + \frac{(a + h)^2}{r^2} \right] \frac{a^2}{(a + h)^2 - a^2} \frac{p}{E} r, \quad (3.10)$$

<sup>1</sup>PEEK (Polyetheretherketone) is a very hard polymer material in wide use in experimental microfluidics.

**Table 3.1:** Properties for selected tube materials as listed by [27] for the polymer materials and [28] for stainless steel.

Material	$E$ [MPa]	$\nu_w$	$\rho_w$ [kg m <sup>-3</sup> ]	$c$ [m s <sup>-1</sup> ]
Silicone rubber	2.05	0.49	$1.15 \times 10^3$	174.7
Teflon	$5.00 \times 10^2$	0.45	$2.14 \times 10^3$	941.4
PEEK	$3.60 \times 10^3$	0.40	$1.31 \times 10^3$	2375.6
Stainless steel	$2.10 \times 10^5$	0.30	$7.75 \times 10^3$	6039.6

and the volume increase associated with the wall displacement is

$$\mathcal{V} = 2\pi a u_r(a) \ell. \quad (3.11)$$

As for the air bubbles, the time-rate of change of the volumetric expansion is the flowrate

$$Q = \frac{2\pi a^3 \ell}{Eh} \frac{a}{h+2a} (1 + \nu_w) \left[ 2(1 - \nu_w) + 2\frac{h}{a} + \frac{h^2}{a^2} \right] \partial_t p, \quad (3.12)$$

from which the wall compliance may be read off immediately as

$$C_{\text{hyd}} = \frac{2\pi a^3 \ell}{Eh} \beta. \quad (3.13)$$

The factor  $\beta$  is comprised of geometric and material variables and is given by

$$\beta = \frac{a}{h+2a} (1 + \nu_w) \left[ 2(1 - \nu_w) + 2\frac{h}{a} + \frac{h^2}{a^2} \right]. \quad (3.14)$$

In the limit of very thin walls  $h \ll a$  this factor becomes  $\beta \approx 1 - \nu_w^2$ . The term of  $\nu_w^2$  is negligible since  $0 \leq \nu_w \leq 0.5$ , which yields a well-known result for thin walls, [30]:

$$C_{\text{hyd}} \approx \frac{2\pi a^3 \ell}{Eh} \quad \text{for } h \ll a, \quad (3.15)$$

used in many instances to model the compliance of the arterial wall, e.g. [31, 32, 33, 34, 35]. In the other limit of  $h \gg a$  which is usually found in experimental microfluidics, eq. (3.13) tends to

$$C_{\text{hyd}} \approx \frac{2\pi a^2 \ell}{E} (1 + \nu_w) \quad \text{for } h \gg a, \quad (3.16)$$

where all dependence on  $h$  vanishes. Both these limits are found in fig. 3.2 which shows the compliance for a silicone rubber tube ( $E = 2.05 \times 10^6$  Pa) and three different values of  $\nu_w$  as a function of  $h/a$ .

## Limitations

It is an underlying assumption of the elastodynamic equation, eq. (3.8), that the displacement fields are small, while the solutions to said equation used in deriving the expressions for  $C_{\text{hyd}}$  assume no axial deformation of the tube. Deviations from these assumptions would obviously make the derived expressions invalid.

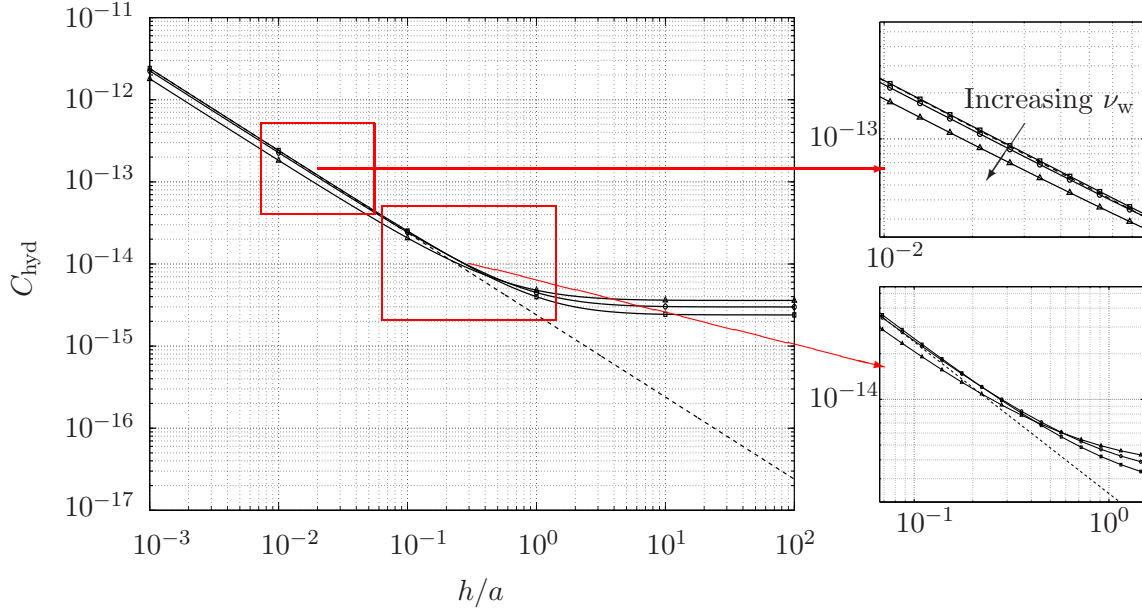


**Figure 3.2:** Wall compliance for varied Poisson ratio as a function of  $h/a$ . The dashed line is the limit of  $h/a \ll 1$ . Squares ( $\square$ ):  $\nu_w = 0.00$ . Circles ( $\circ$ ):  $\nu_w = 0.25$ . Triangles ( $\triangle$ ):  $\nu_w = 0.50$ . The remaining parameters are  $E = 2.05 \times 10^6$  Pa,  $a = 0.125 \times 10^{-3}$  m and  $\ell = 5.0$  cm.

### 3.4 Flow in elastic tubes

Viscous flow in elastic tubes is a coupled fluid-solid interaction problem which is very difficult to solve analytically. In the pulsatile case its solution would yield great insight into the physics of arterial blood flow, prompting the interest of scores of workers, while the transient case is of great interest in systems where a prescribed volume of fluid is to be delivered in a specified time.

#### 3.4.1 Simple EC model

The fluid flow in an elastic tube experiences resistance and inertia along with the compliance caused by the elastic wall. In the simplest EC model, these three circuit elements each act in a point, so the positioning of the three relative to each other may become important, depending on their relative magnitude. Three approaches are illustrated in fig. 3.3, where in each case the flowrate enters at  $p_{\text{enter}}$  and exits at  $p_{\text{exit}}$  with a total pressure drop of  $\Delta p = p_{\text{enter}} - p_{\text{exit}}$ . The compliances are relative to atmospheric pressure (i.e. ground in the EC diagram), since the tube over-pressure relative to atmospheric pressure determines the displacement of the elastic tube wall. When the flowrate meets a compliance, some of it inflates the tube while the rest continues downstream, so the compliance branches the flowrate into an inflating flowrate and a flowrate exiting the tube.

In (a), the compliance is placed upstream of the resistance and inertia, so that all incoming flowrate experiences both resistive and inertial losses before some of it is used to

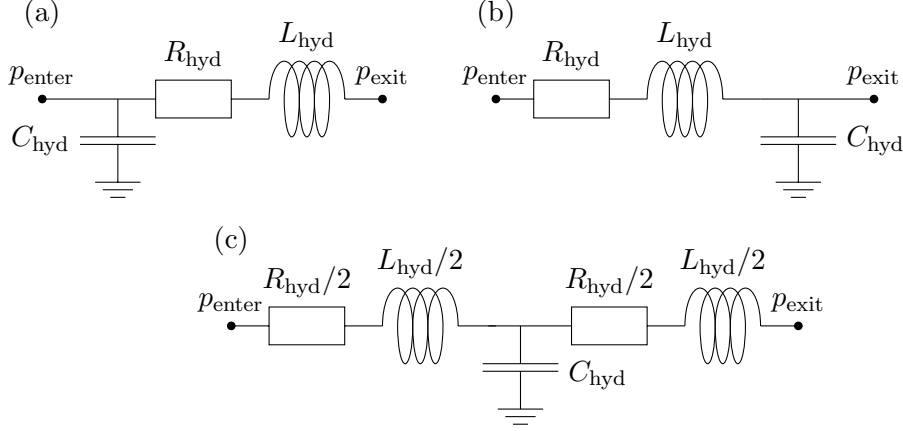


**Figure 3.3:** Three simple approaches for EC modeling of flow in elastic tubes. The flow enters at  $p_{\text{enter}}$  and leaves at  $p_{\text{exit}}$ , in all three cases, which only differ in the positioning of the wall compliance  $C_{\text{hyd}}$ . (a) The compliance is placed downstream of the resistance and inertia, meaning that all incoming flow experiences drag and inertial losses. (b) The compliance is placed upstream of  $R_{\text{hyd}}$  and  $L_{\text{hyd}}$ , so some of the incoming flowrate is branched off into the compliance without experiencing losses. (c) The original tube of axial length  $\ell$  is modeled as two segments of length  $\ell/2$ , with the compliance placed in between. The circuit elements of these tube segments have half the numerical value of the original elements due to the linear dependence of all circuit elements on axial length  $\ell$ .

inflate the wall. The situation is reversed in (b), where the inflation takes place before the flowrate experiences any losses, so only some of the incoming flowrate experiences losses. In the case of a very hard wall, only a very small volume will be used to inflate the wall, and these two approaches will yield almost the same result, but in the other extreme of a very soft wall, the two models will strongly disagree. The first model will over-predict the losses since it assumes all incoming flowrate is exposed to the resistance and inertia, while the second model will under-predict the losses as the inflationary flowrate is branched off before any losses are applied to the it.

Compliance, resistance, and inertial losses are continuously distributed at every axial position in the actual tube, so the further downstream one goes, the more of the flowrate is stored in the inflating tube walls and less continues downstream to be inflicted resistive and inertial losses. To lowest order, this is captured by splitting the original tube of axial length  $\ell$  into two segments of length  $\ell/2$ , and then place the compliance of the original tube in between the resistances and inductances of the new tube segments, as shown in (c). Since all circuit elements depend linearly on axial length  $\ell$  (see eqs. (2.9), (2.21), (3.6) and (3.13)), the elements of the new tube segments have half the numerical value of the original tube circuit elements. In this case, the incoming flowrate experiences both inertial and resistive losses, before some is used to inflate the tube while the rest continues downstream towards the tube exit while being exposed to the resistive and inertial losses of the second tube segment. This last modeling approach has been used in the present work as a low-order model of flow in elastic tubes unless otherwise stated, since a similar approach for heat transfer has been shown to be in very good accordance with the analytical solution, [1]. It may easily be extended to pulsatile flow by exchanging the resistance and inertia



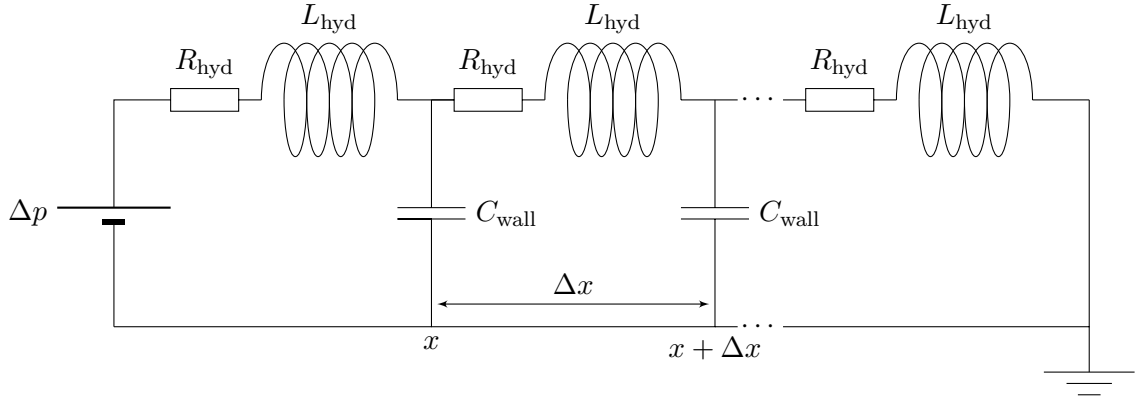


**Figure 3.4:** Improved EC model of flow in elastic tube. The tube has been divided into  $N_{\text{EC}}$  segments, each of axial length  $\Delta x = \ell/N_{\text{EC}}$ . All circuit elements listed are for these new segments, so that e.g. the resistance  $R_{\text{hyd}}$  is given in terms of  $\Delta x$  and not the length of the entire tube,  $\ell$ .

with a Womersley-type impedance  $Z_{\text{Wom}}$ .

### 3.4.2 Continuum model

The physiological interest in understanding the physics governing arterial blood flow has been the driving factor behind most of the theoretical work in the field of inertially dominated flow in elastic tubes. Many models have been presented to various degree of accuracy, but few have proved well against experimental data, arguably due to the tapering and branching of the arterial network. Of special note is the extensions of the theory for pulsatile flow in a rigid confinement by Womersley summarized in [31], the work of Morgan and various co-workers, [32, 33], and the solution of the full wall equations coupled with the fluid equations by Cox, [36], who in addition required the wall to be incompressible and viscoelastic. A good overview of existing blood flow models may be found in [37, 38]. The general problem of pressure driven flow in elastic tubing has drawn comparatively little attention. Work of note is Iberall's derivation of a Laplacian for pressure, [39], and the work by Olsen and Shapiro, [40], who considered large-amplitude oscillations theoretically and experimentally. Unfortunately, none of the presented models are appropriate for the present work due to their assumptions of either thin or viscoelastic walls, neither of which are good approximations in experimental microfluidics: a tube of inner diameter  $a \approx 0.25$  mm usually has a wall thickness of  $h \approx 0.60$  mm corresponding to  $h/a \approx 2$  which cannot be considered thin, and the tube walls show no signs of pronounced viscoelastic behavior.

The accuracy of the model introduced in the section above for flow in elastic tubes may be improved by dividing the tube into more than two segments. Fig. 3.4 shows the tube split into  $N_{\text{EC}}$  segments each of axial length  $\Delta x = \ell/N_{\text{EC}}$ . Considering one mask of this model, the incoming flowrate  $Q(x)$  splits into an inflationary flowrate  $Q_{\text{comp}}^{\text{wall}}(x)$  and a flowrate continuing downstream,  $Q(x + \Delta x)$ , i.e.

$$Q(x) = Q_{\text{comp}}^{\text{wall}}(x) + Q(x + \Delta x). \quad (3.17)$$

$Q_{\text{comp}}^{\text{wall}}(x)$  is given in terms of the pressure at  $x$  in the usual manner as  $Q_{\text{comp}}^{\text{wall}}(x) = C_{\text{wall}} \partial_t p(x)$ . Meanwhile, the pressure drop along one tube segment is given by

$$p(x) - p(x + \Delta x) = R_{\text{hyd}} Q(x + \Delta x) + L_{\text{hyd}} \partial_t Q(x + \Delta x). \quad (3.18)$$

The circuit elements  $R_{\text{hyd}}$ ,  $L_{\text{hyd}}$  and  $C_{\text{wall}}$  all depend linearly on the axial dimension of the element, in this case  $\Delta x$  for each tube segment. Collecting and rearranging eqs. (3.17) and (3.18) yields

$$\frac{Q(x) - Q(x + \Delta x)}{\Delta x} = \hat{C}_{\text{wall}} \partial_t p(x), \quad (3.19a)$$

$$\frac{p(x) - p(x + \Delta x)}{\Delta x} = \hat{R}_{\text{hyd}} Q(x + \Delta x) + \hat{L}_{\text{hyd}} \partial_t Q(x + \Delta x), \quad (3.19b)$$

where the hat is used to indicate an element per axial length, i.e.  $\hat{R}_{\text{hyd}} \Delta x = R_{\text{hyd}}$ . The resolution of the model increases as  $N_{\text{EC}} \rightarrow \infty$  corresponding to  $\Delta x \rightarrow 0$ . In this continuum limit the equations become

$$-\partial_x Q(x, t) = \hat{C}_{\text{wall}} \partial_t p(x), \quad (3.20a)$$

$$-\partial_x p(x, t) = \hat{R}_{\text{hyd}} Q(x) + \hat{L}_{\text{hyd}} \partial_t Q(x). \quad (3.20b)$$

Combining these two equations, one arrives at the following damped wave PDE for the pressure

$$\partial_x^2 p(x, t) = \frac{1}{\mathcal{D}} \partial_t p(x, t) + \frac{1}{c^2} \partial_t^2 p(x, t), \quad (3.21)$$

where the constants are

$$\mathcal{D} = \frac{1}{\hat{R}_{\text{hyd}} \hat{C}_{\text{wall}}} = \frac{a E h}{16 \eta \beta} \quad \text{and} \quad c = \frac{1}{\sqrt{\hat{L}_{\text{hyd}} \hat{C}_{\text{wall}}}} = \sqrt{\frac{E h}{2 \rho a \beta}}. \quad (3.22)$$

$\mathcal{D}$  has units of a diffusion constant ( $\text{m}^2 \text{s}^{-1}$ ) while  $c$  is the speed of the pressure waves. The energy losses associated with the resistance causes the damping of the wave motion which is intuitively correct, as one always finds a pressure wave traveling in an elastic tube to die out at some point downstream of the source.

### 3.4.3 Continuum model in the pulsatile case

The arguments leading to eq. (3.20) may be repeated for the case of pulsatile flow, where a Womersley impedance is used instead of a resistor and inductor in series. Eq. (3.20b) then becomes

$$-\partial_x p(x, t) = \hat{Z}_{\text{hyd}} Q(x), \quad (3.23)$$

and the governing equation for the pressure is

$$\partial_x^2 p(x, t) = \hat{Z}_{\text{Wom}} \hat{C}_{\text{wall}} \partial_t p(x, t), \quad (3.24)$$

while the flowrate is the found from eq. (3.23). At first glance this looks like a diffusion equation, but since  $\hat{Z}_{\text{Wom}}$  is a complex number, this is also a damped wave equation. One solution to this equation is a pair of traveling waves

$$p(x, t) = \psi_1 e^{i(kx - \omega t)} + \psi_2 e^{-i(kx + \omega t)} + p_0, \quad (3.25)$$

where the constants  $\psi_1$  and  $\psi_2$  are determined by the boundary conditions, and  $p_0$  is a reference pressure. The wave number  $k$  is found by plugging eq. (3.25) into the governing equation:

$$k = \pm \sqrt{i\omega \hat{Z}_{\text{Wom}} \hat{C}_{\text{wall}}} \quad (3.26a)$$

$$= \pm \frac{\omega}{c} \left[ \frac{2J_1\left(\alpha i^{\frac{3}{2}}\right)}{\alpha i^{\frac{3}{2}} J_0\left(\alpha i^{\frac{3}{2}}\right)} - 1 \right]^{-\frac{1}{2}}, \quad (3.26b)$$

which is recognized as the regular dispersion relation  $k = \omega/c$  multiplied by a factor comprising effects pertaining to the change in velocity profile for pulsatile flow. The associated flowrate is

$$Q(x, t) = \frac{ik}{\hat{Z}_{\text{Wom}}} \left[ \psi_1 e^{i(kx - \omega t)} - \psi_2 e^{-i(kx + \omega t)} \right]. \quad (3.27)$$

Considering the case of pulsatile flow entering the tube at  $x = 0$  and leaving the tube at  $x = \ell$  with the boundary conditions

$$p(0, t) = \Delta p_{\text{enter}} e^{-i\omega t} + p_0, \quad (3.28a)$$

$$p(\ell, t) = \Delta p_{\text{exit}} e^{-i\omega t} + p_0, \quad (3.28b)$$

the traveling wave solution satisfies these conditions if the constants are given by

$$\psi_1 = \Delta p_{\text{enter}} \left( 1 - \frac{e^{ik\ell}}{2i \sin(k\ell)} \right) + \frac{\Delta p_{\text{exit}}}{2i \sin(k\ell)}, \quad (3.29a)$$

$$\psi_2 = \frac{\Delta p_{\text{enter}} e^{ik\ell} - \Delta p_{\text{exit}}}{2i \sin(k\ell)}, \quad (3.29b)$$

where use has been made of the complex sine function. The flowrate at  $x = 0$  and  $x = \ell$  of this system is given by

$$Q(0, t) = \frac{k}{\hat{Z}_{\text{Wom}}} \left[ \frac{\Delta p_{\text{exit}}}{\sin(k\ell)} - \Delta p_{\text{enter}} \cot(k\ell) \right] e^{-i\omega t}, \quad (3.30a)$$

$$Q(\ell, t) = \frac{k}{\hat{Z}_{\text{Wom}}} \left[ \Delta p_{\text{exit}} \cot(k\ell) - \frac{\Delta p_{\text{enter}}}{\sin(k\ell)} \right] e^{-i\omega t}. \quad (3.30b)$$

The attractive mathematical property of proportionality between flowrate and pressure difference so far encountered has been lost in this continuum limit, and speaking of a linear impedance relating pressure to flowrate is no longer meaningful. A 1:1 mathematical

relation still exists, although the algebraic operations required to arrive at the expressions are more cumbersome than for the idealized case of single circuit elements. However, these new expressions do relate flowrate and pressure difference at every single axial position, and knowing one of the variables, the other can be computed directly. Various other transmission line models for the pressure in elastic tubes has been presented, [41, 42, 43, 44], but none have included the exact Womersley impedance of eq. (2.26).

### 3.5 Summary

Appropriate compliances for the work of the thesis have been derived from quasi-equilibrium expressions, and the validity of these compliances have been justified. Low order modeling of flow in elastic tubes has been discussed, and continuum equations governing damped wave motion have been derived for the over-pressure for both regular and pulsatile flow.

## Chapter 4

# Experimental flow in elastic tubes

As a first step towards full systems-level modeling, the simpler case of tube flow is studied. Two separate experiments have been conducted: verification of the Hagen–Poiseuille law, eq. (2.8) for a very stiff tube, and the transient pressure build-up towards a steady state in an elastic tube exposed to an abruptly applied pressure gradient.

The hydraulic resistance of a hollow fiberglass tube is determined in the first case. Fiberglass has very high Young’s Modulus<sup>1</sup> with small variation in wall thickness and inner radius when pulled into hollow fibers, and meanwhile, the hydraulic resistance is the easiest circuit element to determine experimentally, so this experiment will set the upper limit for the attainable accuracy between theory and experiment for the thesis. All steps will be detailed for this simplest of experiments to illustrate the care taken in all experimental work presented in the thesis.

The second experiment will be used to investigate a transient phenomenon and from this, determine the agreement between EC model and experiment for said dynamic system. In addition to insight into the characteristic dynamic time scales of microflow in elastic tubing, this also serves as a first step towards experimental treatment of pulsatile flow.

### 4.1 Measuring the hydraulic resistance of a tube

Of the three basic circuit elements of inductance, resistance and compliance,  $R_{\text{hyd}}$  is the only which is independent of time, so the hydraulic resistance of a component is by far the easiest circuit element to determine experimentally. This is usually done by simultaneously measuring flowrate through and pressure difference across the component once the flowrate is constant and hence void of transient effects; its resistance is found as the ratio of the two. The experimentally determined resistance may be compared to the theoretically derived expression of eq. (2.9). A hollow glass-fiber was used as the component due to the high accuracy of its inner radius as well as its very low compliance.

Although simple in theory, much care must be taken when conducting this experiment. The theoretical expression for  $R_{\text{hyd}}$  is a function of viscosity which in turn depends heav-

---

<sup>1</sup> $E = 6.03 \times 10^{11}$  Pa, according to [28].

ily on temperature<sup>2</sup> thus necessitating accurate temperature measurements. Moreover, flowrates are rarely measured directly, rather, the mass of fluid exiting the component is continuously measured and divided by the sample time. In microfluidic systems where only small volumes of liquid exit the component, evaporation at the mass measurement station must be prevented or quantified for this method to work.

All experiments in this thesis have been conducted under controlled thermodynamic conditions of  $T = 20.00 \pm 1.00$  °C and  $45.0 \pm 5.0$  % relative humidity.

#### 4.1.1 Method

Prior to experimentation, the water for the measurements (approximately 100 mL) was left undisturbed in a glass in the laboratory for approximately 30 minutes to ensure laboratory and water temperatures were identical. The viscosity was measured with a falling ball viscometer in which a spherical object of known size and density is dropped into a tube of well-known length and diameter, filled with the fluid of consideration. Only gravity and viscous drag are acting on the ball, so the steady state velocity of the ball can be related to the viscosity of the fluid, from the time it takes the ball to drop between two sets of markings on the viscometer tube.

A reference liquid of known viscosity is required for the viscometer. Using DI water as the reference fluid for the viscosity measurements since tabulated values for this are readily available in the literature, e.g. the CRC Handbook of Chemistry and Physics [45], the viscosity of the tap water for the experiments was measured a number of times before the  $\Delta p - Q$  measurements for  $R_{\text{hyd}}$ , and again after the conclusion of these. In both cases, the temperature was taken before and after each individual viscosity measurement. Recording the exact drop time of the viscometer ball was very difficult leading to small errors.

A syringe pump mounted with a 10 cm<sup>3</sup> plastic syringe filled with tap water was used to generate flowrates. The pressure was measured at the tip of the syringe, right before the fiberglass tube, which was press fitted to the fluidic system using a small piece of thick-walled silicone rubber tubing. The free end of the fiber was directed into a laboratory cup on a precision scale, without the fiber glass tube touching the cup walls. Finally, a piece of aluminum foil was placed on the cup as a lid to prevent evaporation, leaving only a small hole for the glass fiber to enter.

To conduct a measurement series, a flowrate was set on the pump and the mass detected by the scale was read out every second. Once the pressure sensor reached a constant level, the average pressure was recorded over a period of about 20 s. The laboratory temperature was measured before and after each experiment.

#### 4.1.2 Instrumentation

**Pressure sensor:** Comark C9551 Pressure Meter (silicon sealed) (Comark Instruments, Beaverton, Oregon, USA), differential pressure meter. Pressure range: 0 – 14 kPa with

---

<sup>2</sup>The viscosity of water varies roughly 2 % per degree celsius, [45].

**Table 4.1:** Relative deviations of the measured viscometer constants from the mean,  $K_{\text{visc}} = 5.4547 \times 10^{-8} \text{ m}^4 \text{ s}^{-2}$ , without correcting for temperature variations. Obtained using DI water.

Exp. #	1	2	3	4	5	6	7	8
$\epsilon_K$ [%]	0.99	0.32	0.83	0.82	0.86	0.16	0.30	0.30

resolution of 10 Pa.

**Viscosity measurements:** Gilmont Instruments GV-2200 Falling Ball Viscometer, using size 2 ball. Fall times measured using a Bonett stop watch with 0.01 s resolution.

**Syringe pump:** Cole-Parmer (Vernon Hills, Illinois, USA), catalog # 789200C.

**Scale:** Mettler-Toledo (Mettler-Toledo, New York, USA) Ax105 DeltaRange, readability 0.01 mg.

**Syringe and tubing:** A BD 10 mL syringe (14.48 mm inner diameter) with Luer-Lok fitting system. Hollow fiber glass tubing (fused silica,  $\ell = 84.7 \text{ cm}$ ,  $a = 0.53 \text{ mm}$  by Supelco, Pennsylvania, USA), fitted to the syringe via a press fit in a small piece of thick-walled silicone rubber tubing.

**Data acquisition and handling:** IBM T41 ThinkPad for acquisition using BalanceLink software by Mettler-Toledo and Dell Inspiron 6400 with MATLAB 7.0.1 (The MathWorks Inc., Natick, Massachusetts, USA) for handling.

### 4.1.3 Results

#### Viscosity experiment

Using DI water as the reference fluid, 8 measurements of the viscometer constant was completed. The temperature variations for each measurement was at most  $0.1^\circ\text{C}$ , so the temperatures recorded before and after was averaged for each measurement. The viscometer constant was computed for each measurement using the interpolated values of the rheological constants from [45] at this average temperature; the average of these viscometer constants for all eight measurements was  $K_{\text{visc}} = 5.4547 \times 10^{-8} \text{ m}^4 \text{ s}^{-2}$ . Deviations of less than 1 % from the mean value of the viscometer constant  $K_{\text{visc}}$  was found for the results of the individual measurements, see table 4.1, even without corrections for temperature variations, so  $K_{\text{visc}}$  is used for all viscosity computations in the following.

The viscosity of tap water was determined from  $K_{\text{visc}}$  and the results are given in fig. 4.1. As before, only variations of up to  $0.1^\circ\text{C}$  were observed during each measurement, so the mean temperature is used in the figure. The data is distributed evenly about the data for DI water, which has been obtained by interpolation using a fifth order polynomial curvefit to the data from CRC Handbook of Chemistry and Physics, [45]. The measured viscosities of tap water deviate around 1 % from the interpolated data for DI water when

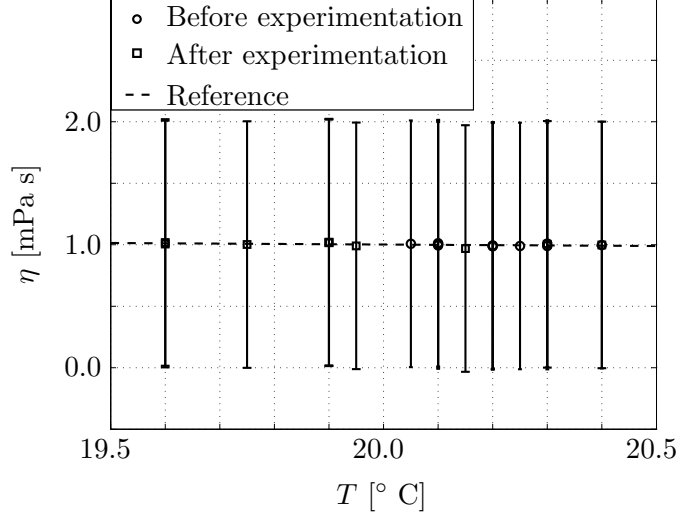


**Figure 4.1:** Measured viscosities, computed using the average viscometer constant  $K_{\text{visc}}$ . “Before” and “After” in the legend indicates when each measurement was made in reference to the  $\Delta P-Q$  measurements, and the reference is obtained by interpolation using a fifth order polynomial curvefit to the data for DI water from CRC Handbook of Chemistry and Physics, [45]. The errorbars are a result of the previously mentioned timing difficulties when measuring the drop time of the viscometer ball.

taking temperature into account, but due to the even distribution about the data for DI water, the viscosity variation between DI and tap water is neglected and the interpolated data for DI water is used for all computations in the following.

### $\Delta p - Q$ experiments

Using different flowrates, the recorded relation between specified flow rate and measured pressure drop is given in fig. 4.2. Without correcting for temperature variations, a linear relation passing through the origin is observed and the slope of a linear curve fit to the data is  $\bar{R}_{\text{hyd}}^{\text{meas}} = 419.08 \times 10^9 \text{ Pa s m}^{-3}$ , where the superscript ‘meas’ is included to distinguish between theoretically calculated and measured hydraulic resistance. The relative error between  $\bar{R}_{\text{hyd}}^{\text{meas}}$  and the individual measurements conducted at different temperatures is low as shown in table 4.2, validating the use of the linear approximation. The theoretical values of the hydraulic resistance at all measurement temperatures have been computed using the interpolated data for DI water for the viscosity, also given in table 4.2, and the mean value,  $\bar{R}_{\text{hyd}}^{\text{theo}} = 435.61 \times 10^9 \text{ Pa s m}^{-3}$ , has been used in fig. 4.2. The relative variations from the mean of less than 0.1 % for  $\bar{R}_{\text{hyd}}^{\text{theo}}$  can be attributed to the low temperature variations resulting in small variations of the viscosity.

The results indicate good agreement between theory and experiment even without the negligible temperature variations initially thought to introduce deviations, but the data is not completely coinciding; rather, the same overshooting of the theoretical values exceeding the errors on the viscosity measurements is observed throughout. The relative



**Table 4.2:** Variations of the individual measurements and theoretical calculations of  $R_{\text{hyd}}$  with temperature. All entries of  $R_{\text{hyd}}$  has the unit  $\text{GPa s m}^{-3}$ .  $\epsilon_{R_{\text{hyd}}^{\text{meas}}}$  is the relative variation between the slope of the linear curvefit in fig. 4.2 given by  $\overline{R}_{\text{hyd}}^{\text{meas}} = 419.08 \times 10^9 \text{ Pa s m}^{-3}$ , and each measurement. No corrections for temperature have been made. For the theoretically determined values,  $\epsilon_{R_{\text{hyd}}^{\text{theo}}}$  is the relative deviation from the mean  $\overline{R}_{\text{hyd}}^{\text{theo}} = 435.61 \times 10^9 \text{ Pa s m}^{-3}$ , of which the latter also is given in fig. 4.2.

$T$ [ $^{\circ}\text{C}$ ]	20.30	20.20	20.10	20.20	20.15	20.40	20.30	20.25
$R_{\text{hyd}}^{\text{meas}}$	432.30	400.19	405.13	419.95	419.95	407.60	416.99	419.95
$\epsilon_{R_{\text{hyd}}^{\text{meas}}} [\%]$	3.15	4.51	3.33	0.21	0.21	2.74	0.50	0.21
$R_{\text{hyd}}^{\text{theo}}$	434.95	436.01	437.08	436.01	436.55	433.89	434.95	435.48
$\epsilon_{R_{\text{hyd}}^{\text{theo}}} [\%]$	0.15	0.09	0.34	0.09	0.21	0.40	0.15	0.03

error between  $\overline{R}_{\text{hyd}}^{\text{meas}}$  and  $\overline{R}_{\text{hyd}}^{\text{theo}}$  is 3.80 %, which is more than what can be attributed to the errors introduced by the simplifications above, and the repetitiveness of the error suggests a wrong numerical value has been used in the theoretical calculations. Having eliminated viscosity as the source of error, eq. (2.9) suggests a variation of the tube inner radius to be the source: such a variation of 1.40 % on the tube radius, which is equivalent to 3.6  $\mu\text{m}$ , would be sufficient to account for the deviation. The manufacturer has specified the tube inner diameter to 0.53 mm, so the above variation is below the given tolerances and the experiment cannot be conducted to higher precision with the available equipment.

#### 4.1.4 Validation of result

The Reynolds number depends on the selected flowrate; for the above experiments the Reynolds number based on the diameter lies in the range 4-80, meaning that inertial effects dominate viscous effects and that the flow of tap water does not fully satisfy the Stokes flow assumption. However, the flow is still in the lower end of the laminar regime and the tube has no kinks, bends etc., so the Hagen–Poiseuille law is valid.

The flow is fully developed at a distance  $\ell_{\text{ent}}$  downstream of the inlet according to Shah and London, [46]

$$\ell_{\text{ent}} \approx \frac{0.6}{1 + 0.035 Re_d} d + 0.056 Re_d d, \quad (4.1)$$

where  $Re_d$  is the Reynolds number based on the tube inner diameter  $d$ . For the present  $\Delta p - Q$  experiments using the largest value of  $Re_d$  above, this distance is no more than  $\ell_{\text{ent}} \approx 2.46 \text{ mm}$ , and since the fiber glass pipe has a total length of 84.7 cm, only small errors are introduced by assuming fully developed flow throughout the tube. The observed variation between theory and experiment in fig. 4.2 is likely caused by variations in the tube radius.

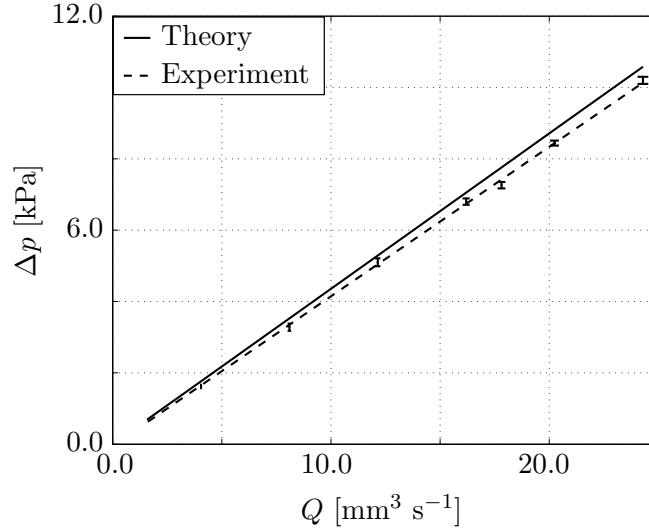


**Figure 4.2:** Measurements (dashed) and theoretically determined (solid) flowrate and pressure drop. The errorbars are a result of the viscosity error. A small, but constant, overshooting of the theoretically determined  $R_{\text{hyd}}$  exceeding the errorbars is observed.

## 4.2 Transient build-up of pressure in an elastic tube

The fairly complex physics of transient viscous fluid flow in an elastic tube contains all three basic EC elements: fluid resistance, fluid inertia and compliance of the elastic wall. The simple case of only a tube is used to gauge the validity of EC modeling of dynamic flow, and allows for estimating the characteristic relaxation<sup>3</sup> time when wall elasticity is introduced.

### 4.2.1 Pressure generation considerations

Ideally, the pressure increase driving the flow should be applied instantly to ensure that only the effects of transient flow in an elastic tube are observed, but due to the inherent time-lag in any pressure generating device this is not physically achievable. However, applying the pressure difference on a time-scale significantly faster than the temporal resolution of the pressure sensor (which is 1 ms), the pressure will appear to have been added abruptly to the sensor. This, too, is unfortunately also not possible with conventional electromagnetic, piezoelectric, or servo valves which all have a temporal resolution of about 2 ms, [47, 48, 49].

A simple way of generating a pressure difference on time scales faster than 1 ms is to drop a weight on the outside of the tube. As soon as the falling weight hits the elastic tube, a pressure increase propagates through the tube wall, but the water contained in the tube will not experience the pressure increase before it has traveled across the tube. Relying on the usual assumption of incompressibility for the water, the only elastic part of the

<sup>3</sup>Recall that the characteristic relaxation time is circa 1 ms for rigid walls as discussed in sec. 2.3.1.

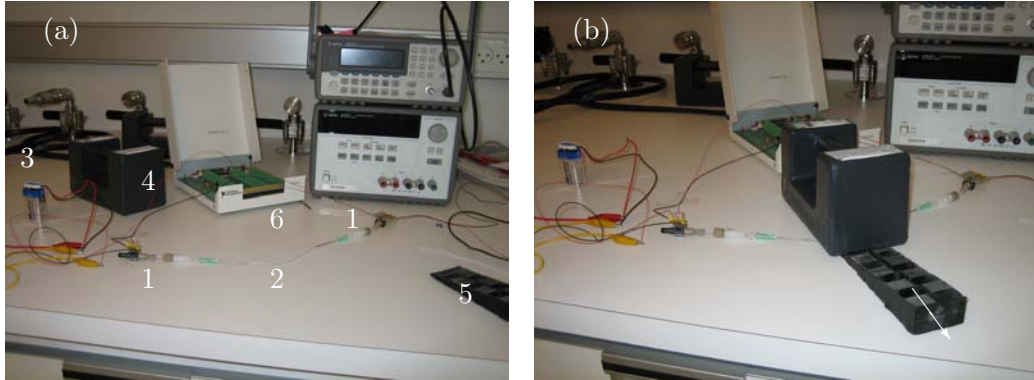


**Figure 4.3:** Setup for the transient Poiseuille experiment. (a) The constituent parts. (b) The setup ready for experimentation. The pressure difference is generated by swiftly yanking the wedge in the direction of the arrow. **Legend** (1): Pressure sensors, (2): Tube, (3): 9 V battery, (4): Weight, (5): Wedge, (6): Data acquisition connector unit.

system is the silicone rubber tube<sup>4</sup>. Solely the elastic  $p$ -waves are of interest since these transfer the pressure increase to the contained water, so the wave speed may be taken directly from table<sup>5</sup> 3.1. Since the wall thickness is  $h = 0.3$  mm, the pressure increase is deposited in the water in  $t = h/c \approx 2 \times 10^{-6}$  s after the weight is dropped, much faster than the 1 ms temporal resolution of the pressure sensor.

#### 4.2.2 Experimental setup and procedure

For these experiments, a primed pressure sensor was connected to each end of a water-filled silicone rubber tube segment, and an over-pressure was suddenly generated by dropping a 5 kg weight on the tube. Prior to generating the over-pressure, the weight was leaned onto a common door stopper wedge keeping the bottom of the weight just above the tube. By swiftly pulling the wedge out it drops onto the tube and compresses it, thus generating an over-pressure. The experimental setup is shown in fig. 4.3.

The pressure sensors were connected to common 9 V batteries for voltage supply in an effort to minimize readout noise. Data was sampled for 5 s from both pressure sensors at a rate of 100 kHz, to ensure the capture of all time scales, and the weight was dropped roughly 1 s after the commencement of data logging.

#### 4.2.3 Instrumentation

**Pressure sensors:** Sensortechinics (Puchheim, Germany) 26PC02K0D6A differential pressure sensors with a range of 0-2 bar and a manufacturer specified temporal resolution of 1 ms. The sensors are fitted with Upchurch Scientific (Oak Harbor, Washington,

<sup>4</sup>This is of course an approximation, but since the bulk modulus of water is  $K = 2.2 \times 10^9$  Pa while Young's Modulus of silicone rubber is  $E = 2.05 \times 10^6$  Pa the approximation is justified.

<sup>5</sup>Strictly speaking, the simplifications leading to eq. (3.8), on which the table is based, are not valid since all wave motion along the axis of the tube has been ignored. Including this motion yields a slightly different  $p$ -wave speed given by  $c = \sqrt{(\lambda_w + \mu_w)/\rho_w}$ , but for estimates, this is not of importance.

**Table 4.3:** Values of EC elements for the simple model of tube flow of eq. (4.2).

Element	Value
$R_{\text{hyd}}$	$1.97 \times 10^9 \text{ Pa s m}^{-3}$
$L_{\text{hyd}}$	$8.82 \times 10^7 \text{ Pa s}^2 \text{ m}^{-3}$
$C_{\text{wall}}$	$2.99 \times 10^{-13} \text{ m}^3 \text{ Pa}^{-1}$

USA) NanoPort fittings, which are glued on using Loctite (part of Henkel Corporation, Düsseldorf, Germany) 495 glue. One end of each sensor is left in ambient conditions so the sensors measure relative to atmospheric pressure.

**Batteries:** Regular 9 V batteries by Memorex (Imation Electronic Products, Weston, Florida, USA).

**Tubing:** Silicone rubber tubing ( $\ell = 20 \text{ cm}$ ,  $a = 0.6 \text{ mm}$ ,  $h = 0.3 \text{ mm}$ ).

**Data acquisition and handling:** National Instruments (National Instruments Inc., Austin, Texas, USA) DAQCard-6062E with 500.000 samples/s connected to pressure sensors by a National Instruments SCB-68 Connection Unit. Data acquisition on an IMB T43 laptop using a simple program developed in National Instruments LABVIEW 8.5.1. based on ExpressVIs and handling using MATLAB 7.0.1 on a Dell Inspiron 6400 laptop.

#### 4.2.4 Equivalent circuit model of the system

The (almost) abruptly generated pressure difference starts a Poiseuille flow of the water towards the pressure sensors. The flow cannot enter the pressure sensors as these are already liquid filled and have no open ends, so the flowrate at the pressure sensors is zero. The EC model for this system has already been presented in sec. 3.4.1, and since the weight was placed at the middle of the tube, the two sensors experience the same pressure build-up, and consequently, behave according to the same model. The model of fig. 3.3(b) has been used instead of the more correct model of fig. 3.3(c) because the condition of no flow to the sensor would require no flow through the elements downstream of the wall compliance in the latter case, resulting in the model of fig. 3.3(b). The following relation is readily found from the normal relations

$$\Delta p_{\text{sens}}(t) + R_{\text{hyd}} C_{\text{wall}} \partial_t \Delta p_{\text{sens}}(t) + L_{\text{hyd}} C_{\text{wall}} \partial_t^2 \Delta p_{\text{sens}}(t) = \Delta p, \quad (4.2)$$

where  $\Delta p_{\text{sens}}(t)$  and  $\Delta p$  are the sensor and applied over-pressures respectively. This second order ODE governs a damped oscillatory motion. The values of the circuit elements are listed in table 4.3. As for an  $RCL$ -circuit in electronics, this system has three inherent

time-scales

$$\tau = R_{\text{hyd}} C_{\text{wall}} = 3.33 \times 10^{-4} \text{ s}, \quad (4.3a)$$

$$\tau = \sqrt{L_{\text{hyd}} C_{\text{wall}}} = 3.86 \times 10^{-3} \text{ s}, \quad (4.3b)$$

$$\tau = \frac{L_{\text{hyd}}}{R_{\text{hyd}}} = 4.48 \times 10^{-2} \text{ s}, \quad (4.3c)$$

of which only the latter two can be resolved by the sensors. The  $RC$ -time is related to the oscillation period as  $T = 2\pi\sqrt{L_{\text{hyd}}C_{\text{wall}}} \approx 24 \text{ ms}$ , while the  $LR$ -time relates to the decay of the pressure amplitude for each oscillation. However, for a system of no compliance, the  $LR$ -time corresponds to the characteristic relaxation time and is thus the EC version of the characteristic inertial relaxation time  $\tau = a^2/(\gamma_1^2\nu)$  of sec. 2.3.1. This latter is  $\tau = 62.0 \text{ ms}$  for the present case, so the EC result is close.

As already discussed, this model may be improved by dividing the tube into more than two segments, or using the continuum limit of infinitely many segments. In this limit, the governing equation is exactly that given in eq. (3.21), with the boundary conditions of  $\Delta p_{\text{sens}}(0, t) = \Delta p$  and  $\partial_x \Delta p_{\text{sens}}(\ell, t) = 0$ , where this latter follows from setting  $Q(\ell, t) = 0$  in eq. (3.20b).

#### 4.2.5 Statistical analysis

Noise from the pressure sensor output signals are removed by filtering. Although batteries are used to supply the pressure sensor input voltage, noticeable noise is still present in the output signals. A frequency analysis of the pressure sensor output revealed several noise peaks at frequencies around 3 kHz and one large peak at  $f \approx 8.1 \text{ kHz}$ , see fig. 4.4, corresponding to time scales of approximately  $5.9 \times 10^{-4} \text{ s}$  and  $1.2 \times 10^{-4} \text{ s}$ , respectively. These frequencies are faster than the specified sensor resolution and have been removed by filtering.

A lowpass Butterworth filter has been chosen as it, contrary to most filters, has no ripples in the passband, but still rolls off fairly steeply in the stopband<sup>6</sup>. Butterworth filters are characterized by their order  $o$  and the cutoff-frequency  $\omega_c$  (the angular frequency above which no output is desired). The higher the order, the steeper the roll-off at the cutoff-frequency, but unfortunately higher order filters are more time-consuming to employ as more computation is needed. An undesirable property of filters is their propensity of introducing a phase-shift to the filtered signal, although this may be minimized by first filtering the signal in the direction of its acquisition, i.e. from time  $t_0$  to time  $t_{\text{end}}$ , and subsequently filtering the just filtered signal in reverse, i.e. from time  $t_{\text{end}}$  to time  $t_0$ . For an in-depth discussion of signal filters the reader is referred to [50].

For all results in this chapter a Butterworth filter of order  $o = 7$  with a cutoff-frequency of  $\omega_c = 2 \times 10^3 \text{ rad s}^{-1}$  has been employed, and filtering has been carried out “in both directions” to minimize phase-shifts.

<sup>6</sup>The “passband” is the frequencies allowed to pass and the “stopband” is the blocked frequencies. For a lowpass filter this constitutes the frequencies above the cutoff-frequency, the first of the unwanted frequencies.

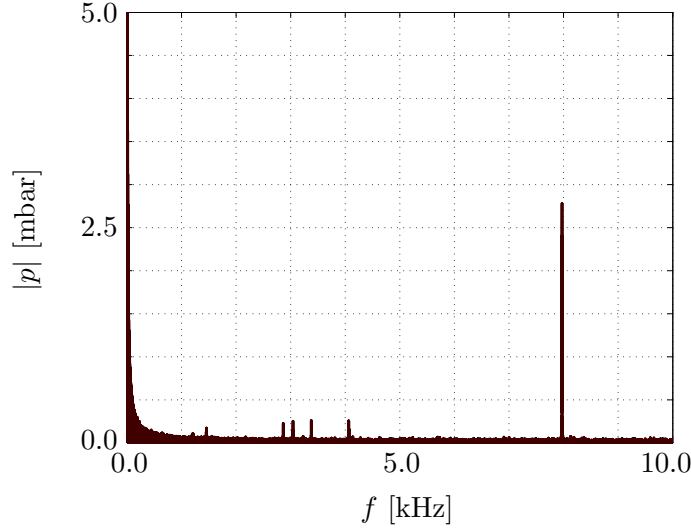


**Figure 4.4:** Measurement noise spectrum obtained by performing a fast Fourier transform on a reference measurements of the primed system sans the over pressure.

#### 4.2.6 Results

The measured pressures from each sensor as a function of time is shown in fig. 4.5. Following a curve somewhat resembling the characteristic curve of damped oscillations, the pressure reaches a constant value of  $\Delta p = 7.3 \times 10^4$  Pa roughly 0.4 s after the weight is dropped. Only half of the mass of the weight will go to the fluid pressure increase since one end of the weight continuously rests on the table, and assuming the contact area between the weight and the tube to be  $\mathcal{A} \approx 1 \times 10^{-1} \text{ m} \times 2 \times 10^{-3} \text{ m} \approx 2 \times 10^{-4} \text{ m}^2$ , the maximally attainable fluid pressure is  $\Delta p \approx 1.2$  bar. Since some of this pressure is used to compress the wall and given the level of uncertainty in the estimated value of the area, the found pressure increase of  $7.3 \times 10^4$  Pa is probable. The input signal was cutoff above 4.25 bar due to limitations on maximum input voltage on the data acquisition card, causing the abrupt cutoff of the first pressure peak in fig. 4.5(a).

The results of the EC model using either one or four terms are also shown in the figure along with a numerical solution to the continuum equation. The low-order models have been solved using MATLAB's `ode45` ODE solver. The PDE governing the continuum model is easily solved analytically for a traveling pressure pulse, but the startup problem considered here is more demanding and has therefore been solved numerically with the generic finite element solver of COMSOL MULTIPHYSICS using a first order BDF method in time and second order Lagrange elements in space.

All three models agree with the experimentally observed behavior of a damped harmonic oscillatory pressure reaching a steady state  $\sim 0.4$  s after the weight was dropped. The oscillation period from the one-term EC model is roughly 24 ms, while the higher-order EC models have oscillation periods of about 20 ms; both of these compare favorably to the oscillation period of about 27 ms found in the experimental data.

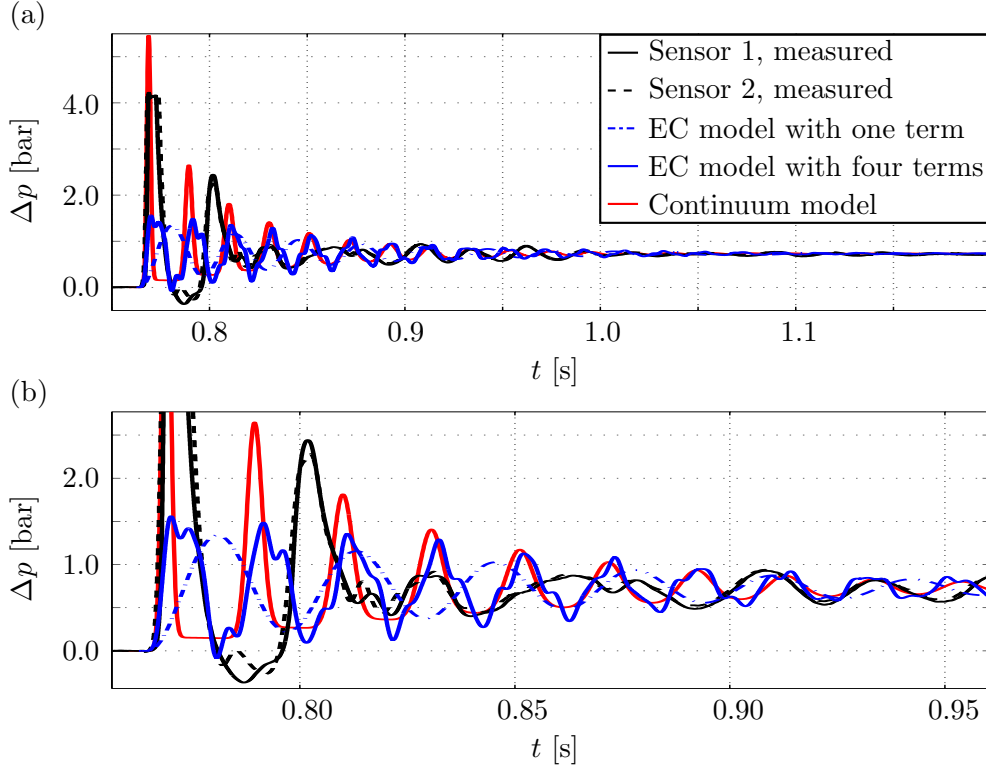


**Figure 4.5:** Transient Poiseuille flow results. Pressure builds very quickly after the weight is dropped, and goes to a constant value of  $\Delta p = 7.3 \times 10^4$  Pa in a manner somewhat resembling a damped harmonic oscillator. Also included are the results of the simple EC model of eq. (4.2) (solid blue), a slightly more elaborate EC model in which the original tube is divided into four segments with compliances positioned in between them (blue dash-dot), and the continuum limit of infinitely many such tube segments (solid red). The four-term EC model and continuum model only have slight disagreements. (a) The full measurement of sensor pressure shows a rapid increase at first followed by a relaxation to a constant value in approximately 0.4 s. The pressure sensor input was cut off at 4.25 bar, so the prediction of the continuum model of 5.45 bar pressure at the initial peak cannot be verified. (b) Zoom on the pressure oscillations following the initial peak. Although none of the three models reproduce the measurements exactly, they all capture the essential behavior, the total relaxation time and the frequency of the damped oscillations. In addition, the continuum model also captures the amplitude peaks of the subsequent waves.

The fluid can only flow when the compliant wall yields due to the blockage at each end, and it is found that only the time scales where inertia enters are found in the model results; the  $RC$ -time is not dominant while the  $LR$  and  $LC$  times are. Comparing to the simple cases of sec. 2.3 where the walls were assumed infinitely stiff, the inclusion of elastic walls has introduced a second time-scale to the physics, which all the models account for. The shortcomings of the EC model are many, with the most glaring being disregard of wall inertia, so the fact that the model fairly well captures the measured physics using a maximum of four terms, indicates that the dominating physical phenomena are accounted for.

### 4.3 Summary

The simplest microfluidic experiment was conducted by experimentally determining the hydraulic resistance of a hollow glass fiber tube. Much care was taken to account for temperature variations when conducting the experiments, as it was expected the strong dependence of viscosity on temperature would yield noticeable deviations. Theory and experimental data was found to be in good agreement, even without correcting for the small temperature variations during experimentation, but the theoretical and experimental results did not completely coincide. It was argued that deviation of the tube inner radius below the specified tolerance would explain this discrepancy, so the attainable resolution of the lumped-parameter EC models is set by the manufacturer-specified tolerance of the inner radius of the tube used.

A transient experiment of abruptly started pressure driven flow in an elastic tube was conducted. A simple EC model was used to model the system, and was found to be in fair agreement with the experimental data. A difference in characteristic time for the fluid pressure to reach a steady state was found to increase by roughly one order of magnitude by inclusion of the elastic walls, and a second time scale was observed as the pressure approached a constant value. It was discovered that the continuum model, thought to exceed the simple low-order models in accuracy, was only slightly better in capturing this transient phenomenon.



## Chapter 5

# The constructed pressure source

An experimental setup capable of probing the low kilohertz range is required for the characterization of component dynamics that is the ultimate goal of the thesis. This chapter presents a driving mechanism constructed for said purpose.

### 5.1 Initial considerations

A microfluidic driving mechanism delivers either a specified volume (flowrate) or a specified pressure. However, one cannot arbitrarily select both pressure and flowrate for a given system since the Stokes equation governing microfluidic flow, eq. (2.4), must be satisfied, and flowrate is a manifestation of fluid velocity. Rather, pressure or flowrate may be specified while the other is determined by the system. Independently of the choice of specified physical quantity in the setup, properties such as frequency and amplitude ranges are critical and should be maximized. The driving mechanism will be used to expose compliant media to pulsatile pressure and flowrate, so although the inertial time scale is believed to be about 1 ms from theoretical considerations, the transient experiment of chapter 4 suggests that the relaxation time scale of the system might be closer to 10 ms. Microfluidic tubing has an inner radius of approximately 0.2 mm, so in order to observe the pulsatility, displacements of minimum 2 mm in the tubing is desirable. This, in turn, requires that the setup delivers stroke volumes of about 0.1 mm<sup>3</sup>.

A thorough survey of micropumps and flow generators, both commercially available and documented in scientific literature, [51, 52], show that while few can operate in the low kilohertz range, none have been developed for this purpose. Those capable are all pressure generators displaying an interdependence between amplitude and frequency while generating very small flowrates, so a new driving mechanism has been developed to better probe the desired frequency range.

### 5.2 Choice of actuator

Actuators deliver either a torque or a force. The first category of actuators include, but is not limited to, rotating electro motors known from a wide variety of commercial

applications e.g. automatic car windows, kitchen blenders, radio-controlled toy cars. Due to their construction, the controlling parameter is the angular velocity rather than the torque; this latter simply adjusts itself to deliver the specified angular velocity, as long as the required torque is below the maximum torque capability of the motor. Thus, electro motors are well-suited as the driving mechanism in a flow generator, since they will adjust the torque (which will determine the pressure in the fluidic system) to the system on which they operate while delivering a specified number of rotations per unit time. This latter can be related to a specified stroke volume of fluid per unit time, i.e. a flowrate. However, no electro motors with an angular velocity above  $10 \times 10^3 \text{ rpm} \approx 160 \text{ Hz}$  are available, so the required frequency range is not attainable with these devices.

Two types of force-delivering actuators are appropriate for oscillations in the low kilohertz range: linear electromagnetic actuators and piezoelectric<sup>1</sup> actuators. Piezoelectric actuators are most appropriate as pressure generators due to the proportionality between voltage and stress, however, very high voltages are required for even minute deflections ( $20 \text{ V}_{\text{pp}}$  usually causes deflections of  $\mathcal{O}(1 \text{ nm})$ ), which in turn yields high temporal resolution. It is thus a trivial task to produce oscillations of about  $5 \text{ MHz}$ , but the very limited amplitude of the oscillations means that very low volumes of fluid can be displaced. This problem may be overcome by stacking the piezoelectric material in layers and hence amplifying the deflection, since the total deflection of the stack is the sum of the deflection of all layers. Even still, a very large stack (about  $1 \text{ m}$  thickness) is required for a deflection of  $1 \text{ mm}$ , and such a stack should not be operated above  $160 \text{ Hz}$ , [53], so piezoelectric actuation is also not a viable option for the present work.

Of the linear electromagnetic actuators, a simple type is the “voice coil actuator” which is the traditional actuator used in loud speakers. It consists of a permanent magnet fixed behind a coil of electrically conducting wire, which moves, when an electrical current is sent through the wire. To concentrate the energy of the magnetic field, a soft iron core attached to the permanent magnet fills the middle of the coil, without impeding its movement. The force generated is proportional to the current in the coil, and frequencies up to about  $20 \text{ kHz}$  are known to be achieved by some commercial loud speakers. Thus, having a voice coil actuator deliver a well-known force  $F$  on specified area of fluid  $\mathcal{A}$ , a known pressure  $p = F/\mathcal{A}$  is generated, well into the low kilohertz range. Additionally, by varying the current in the coil, the force and hence the pressure amplitude is varied independently of the frequency. This type of actuator has been chosen for the driving mechanism, which then acts as a pressure source.

### 5.2.1 Actuator

The actuator used in the source is a LA08-10-000A voice coil actuator (BEI Kimco Magnetics, San Marcos, California, USA). The permanent magnet and the coil assembly are not held together but are two separate pieces, as shown in fig. 5.1. The actuator delivers  $\mathcal{K}_F = 1.1 \text{ N A}^{-1}$  and has a characteristic electrical time of  $\tau = 160 \text{ }\mu\text{s}$ , corresponding

---

<sup>1</sup>The piezoelectric effect exhibited by certain materials (notably crystals and certain ceramics) is the ability to generate an electric potential in response to an applied stress. The effect is reversible since the materials experience a stress when a voltage drop is applied.

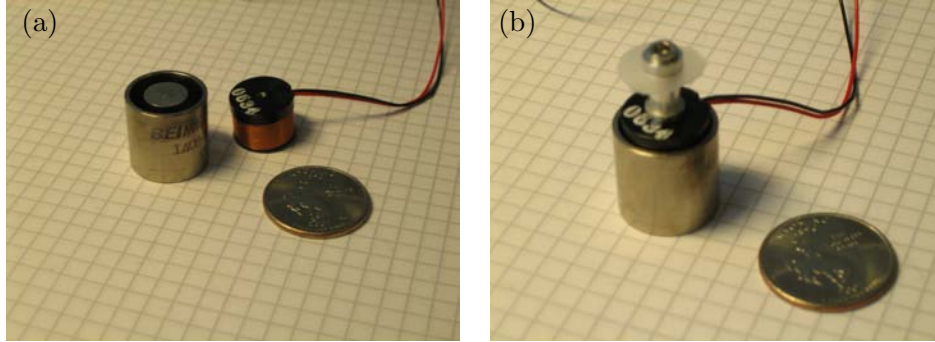


**Figure 5.1:** BEI Kimco LA08-10-000A voice coil actuator next to an American quarter dollar coin. The grid lines intersect every 5 mm. (a) The two parts constituting the actuator: The coil (with the wires exiting) and the permanent magnet. (b) The assembled actuator, mounted with the plunger and membrane (see sec. 5.3.2 for details on the plunger).

to a characteristic frequency of  $f = 0.99 \text{ kHz}$ . The peak force of this actuator is 6.7 N, the “continuous stall force” (the maximum continuous force the actuator is capable of delivering for a sustained period of time) is 1.97 N and the stroke length is maximally 2.03 mm. Since the force depends linearly on the current,  $F = \mathcal{K}_F I$ , the following holds for the generated pressure

$$p = \frac{\mathcal{K}_F}{\mathcal{A}} I. \quad (5.1)$$

With an area of circa  $40 \text{ mm}^2$ , the actuator will be able to deliver a volume per stroke up to  $80 \text{ mm}^3$ , while the pressure can be varied independently through the current. The actuator data sheet is included in appendix C.

### 5.3 Pressure source design

The basic pressure source design is shown in fig. 5.2. A liquid-filled chamber is separated from the actuator by a thin silicone rubber membrane. The actuator delivers its force on

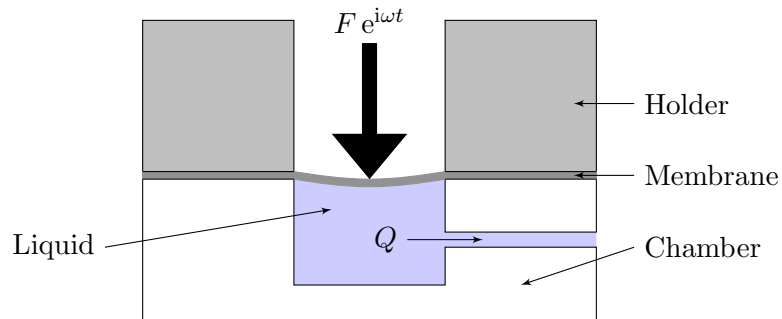


**Figure 5.2:** Working principle of the constructed pressure source. A silicone rubber membrane separates the liquid-filled chamber from the actuator, and the actuator acts on the membrane. A holder fixates the actuator in the setup.

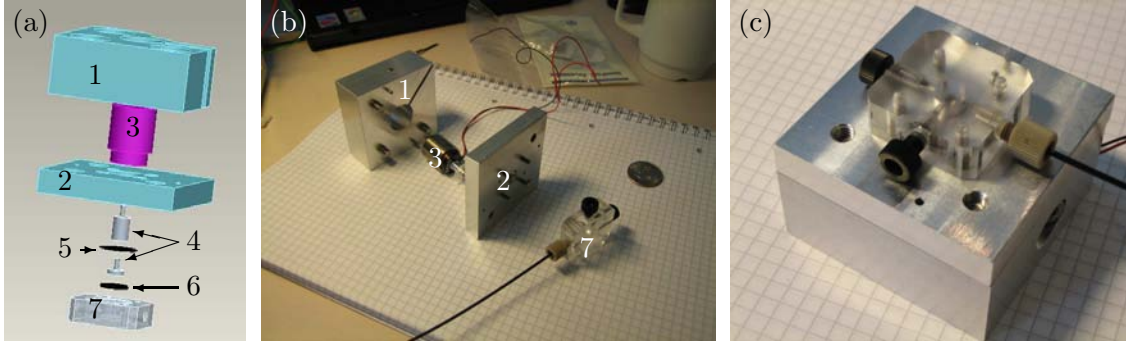


**Figure 5.3:** Constructed pressure source. (a) CAD drawing showing the parts of the pressure source. (b) The fabricated parts prior to assembly. An American quarter is placed to the right of the device for scale and the grid lines intersect every 5 mm. The actuator (3) has been mounted with the plunger and membrane. (c) The assembled pressure source with two of the three exits blocked. **Legend** (1): Actuator holder, (2): actuator guide, (3): actuator, (4): plunger, (5): membrane, (6): O-ring and (7): chamber.

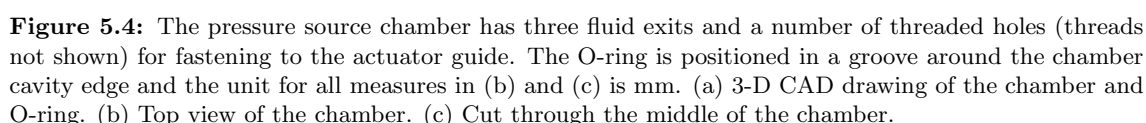
said membrane, and is held in place by a rigid holder. The membrane is clamped between the holder and chamber, which are held together by screws. The pressure source was designed in close collaboration with workshop director Henrik Ljunggren of Novo Nordisk A/S, Hillerød, who also fabricated the device. CAD drawings and photos of the source are given in fig. 5.3.

### 5.3.1 Holder and actuator guide

The holder consists of two parts. One part holds the permanent magnet of the actuator, while the other is used to guide the motion of the actuator. Both parts are made of aluminum.

The permanent magnet and iron core of the actuator have an outer casing of circular cross section (diameter 19.05 mm). The holder, made from a slab of aluminum of height 3 cm, width 6 cm and length 6 cm, has a throughhole in the center of the slab of diameter 19.50 mm, slightly larger than the actuator magnet. A cut of roughly 2 mm thickness for the height of the slab is made from the throughhole to one of the corners, and a screw is inserted normal to the cut. The actuator magnet is placed in this holder and fastened using this screw. The permanent magnet holder is labeled ‘1’ in fig. 5.3(a)-(b), and the cut is visible in (b).

The actuator guide is mounted underneath the magnet holder. Also made from aluminum of same length and width but of height 1 cm, the guide has a throughhole of circular cross section and radius 4 mm along the same axis as the holder throughhole. Another hole of diameter 19.50 mm and of depth 2.5 mm, is made in the top of the guide along the same axis to allow the coil to move back and forth during operation. The coil should then move only in the axis of the holes and not move sideways. A groove is milled to lead out the electric wires to the coil, and the guide and holder are held together by screws.



The actuator coil and membrane are connected via a steel plunger, which is lead through the guide throughhole. The plunger is fastened into the a threaded hole in the top of the actuator coil assembly as shown in fig. 5.1(b). A hole is made in the membrane through which the plunger is drawn. Two cylindrical titanium spacers (outer diameter 7.05 mm) clamp the membrane when the plunger is fastened into the actuator coil.

The chamber, shown in fig. (5.4), is made of a transparent acrylic polymer with a 6.5 mm deep cavity of circular cross section of radius 4.5 mm. A small indentation of 0.4 mm depth and 8.5 mm radius is made at the top of the chamber around the cavity, to make room for the membrane, which itself is 0.2 mm thick and roughly 8 mm radius. A rubber O-ring (9.0 mm inner diameter) is used to seal the membrane against the holder. It is placed in a groove around the edge of the cavity.

## 5.4 Instrumentation used for driving the pressure source

### 5.4.1 Electronics

Two voltage generators have been used: Agilent E3632A DC generator (Agilent Technologies, Santa Barbara, California, USA) and an Agilent 33250A AC generator in connection with a LPA01 power amplifier (Newtons4th Ltd., Mountsorrel, Loughborough, UK).

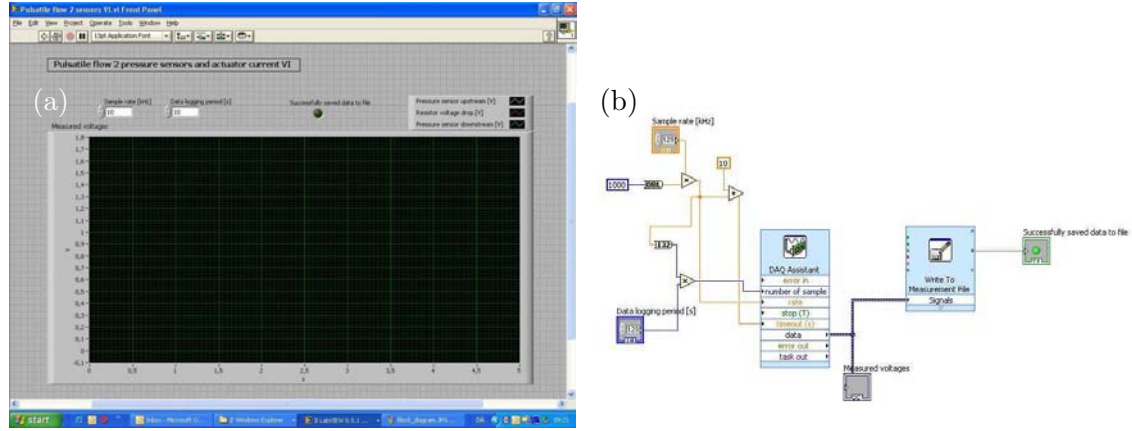


**Figure 5.5:** LABVIEW program used for data acquisition. (a) Front panel. (b) Block diagram.

The pressure source can operate in both DC and AC mode, depending on the current. The DC generator allows the user to set an upper limit on both current and voltage. Whichever of the two is reached first dictates the generator performance; even though the coil current dictates the applied force, the current itself depends on the voltage. The AC generator does not have this property. One may specify an output voltage on the instrument, but the output current depends on the system and the internal electrical impedance of the instrument. A power amplifier was used to drive the pressure source at the desired current.

A small electrical resistance of  $R_{el} = 1.1512 \, \Omega$  was connected in series to the actuator coil, and the voltage drop  $\Delta U$  across said resistance was measured. The resultant current in the system during operation was then found from Ohm's law, eq. (2.18), as  $I = \Delta U / R_{el}$ .

#### 5.4.2 Data acquisition and handling

Data acquisition from pressure sensors and the electrical resistance mentioned above was realized using the same equipment as in the previous chapter (DAQCard-6062E data acquisition card along an SCB-68 Connector Unit). A simple LABVIEW program based on ExpressVIs was developed for the acquisition. The front panel and block diagram of this program is shown in fig. 5.5. All data handling has been carried out in MATLAB on a Dell Inspiron 6400 laptop.

#### 5.4.3 Pressure detection

Pressure was measured using Honeywell 40PC series pressure sensors (Honeywell International Inc., Morristown, New Jersey, USA). These sensors measure change in electric resistance of a silicon membrane as it deflects due to pressure changes, and relates this change in resistance to the pressure difference. Sensors of limit 15 psi (40PC015G) and of  $\pm 50 \, \text{mmHg}$  (40PC001B) were used. Using a DC input voltage of 5 V, the sensors have a built-in amplifier so the output voltage from both sensors is in the range 0.5-4.5 V. The

**Table 5.1:** Results from simple experiment to determine pressure sensor compliance. The pressure difference was in all cases  $\Delta p \approx 1$  bar and the tube radius  $a = 0.254$  mm. The mean compliance for each sensor was determined to  $C_{\text{hyd}}^{15 \text{ psi}} = 1.67 \times 10^{-15} \text{ m}^3 \text{ Pa}^{-1}$  and  $C_{\text{hyd}}^{\pm 50 \text{ mmHg}} = 5.66 \times 10^{-15} \text{ m}^3 \text{ Pa}^{-1}$ .

		15 psi			$\pm 50 \text{ mmHg}$		
Meas.	#	1	2	3	1	2	3
$\Delta x$	[mm]	0.5	1.0	1.0	3.0	3.0	2.5
$C_{\text{hyd}}$	$[10^{-15} \text{ m}^3 \text{ Pa}^{-1}]$	1.00	2.00	2.00	6.00	6.00	4.99

pressure sensors were coupled to the fluidic tubing using a silicone rubber sleeve mounted over both tubing and sensor inlet. The silicone rubber sleeve has an undeformed inner diameter of  $d = 1$  mm and a wall thickness of  $h = 1$  mm.

### Pressure sensor compliance

Pressure sensor compliance stems from both the silicon membrane and the sleeve mentioned above. This compliance has been estimated by the following experiment: A water-filled syringe is coupled to the primed sensor, which has been vacated of air, via transparent teflon tubing of dimensions  $\ell = 10$  cm,  $a = 0.254$  mm and  $h = 0.540$  mm, with a millimeter scale placed right next to the tubing. An air-bubble of about 10 mm length is placed in the tube, and pressure is applied manually with the syringe. Noting the initial position of the bubble front as well as the bubble length, the bubble front position is noted again once the bubble axial length has halved. Assuming negligible effects of curvature at the bubble fronts, the bubble volume is estimated from the bubble length using the known tube radius, and since a halving of volume is associated with a doubling of pressure according to the ideal gas law, the bubble pressure is then twice atmospheric pressure.

Any motion of the bubble (as indicated by a difference in position of the bubble front prior to and after the pressure difference has been applied) will be the consequence of a compliant medium expanding to accommodate the pressure increase. The increase in volume is then  $\Delta \mathcal{V} = \pi a^2 \Delta x$ , where  $\Delta x$  is the change in position of the bubble front. From the coupling of compliance to flowrate, eq. (3.4), one finds  $\partial_t \mathcal{V} = C_{\text{hyd}} \partial_t p$ , so the following holds

$$C_{\text{hyd}} = \frac{\Delta \mathcal{V}}{\Delta p}. \quad (5.2)$$

This has been used for the estimates. The experiment was redone three times and the mean value of the compliance taken as a good estimate. Table 5.1 lists the result of the individual experiments; the mean values of the compliances are  $C_{\text{hyd}}^{15 \text{ psi}} = 1.67 \times 10^{-15} \text{ m}^3 \text{ Pa}^{-1}$  and  $C_{\text{hyd}}^{\pm 50 \text{ mmHg}} = 5.66 \times 10^{-15} \text{ m}^3 \text{ Pa}^{-1}$ .

### Air bubble trapping in the sensors

Priming the sensors without trapping small air bubbles is very difficult. Not only are the sensors not transparent, but the internal volume of the sensors appears to expand away

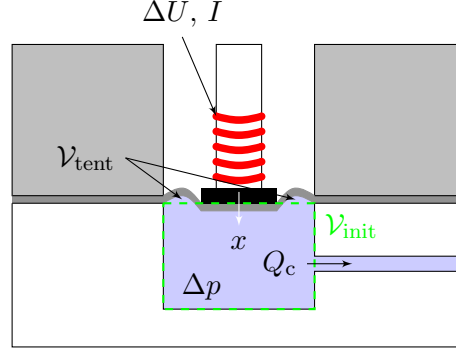


**Figure 5.6:** Schematic illustration of the physical quantities in the pressure source circuit model. A voltage drop is applied to the coil (red wires) giving rise to an electrical current. This current generates a force on the coil, which in turn moves in the direction  $x$ . The displacement of the coil inflates the free part of the membrane with water of volume  $V_{tent}$  since it is easier to expand the membrane than leave the chamber, but a flowrate  $Q_c$  exits the source nonetheless, all the while the pressure difference  $\Delta p$  is generated in the pressure source chamber.

from the inlet towards the membrane, so once an air bubble is trapped inside, it is almost impossible to remove it.

The sensors have been primed using a syringe with a small-diameter needle inserted into the sensor inlet as far down as possible without breaking the delicate silicon membrane, and although much care has been taken, it cannot be ruled out that small bubbles have been present inside the sensors during experimentation. An upper limit to the size of these bubbles is the total internal volume of the sensors, which has been estimated by noting the volume of water needed to fill each of them. The total internal volume of both sensors is estimated to  $1.0 \times 10^{-7} \text{ m}^3$ .

## 5.5 Pressure source circuit model

To fully understand the performance of the pressure source, one must consider the electric circuit of the actuator and the mechanics of the coil motion in addition to the microfluidics of the system. A circuit model of the entire pressure source is presented in the following as a low-order model coupling it to the EC equations, and a schematic drawing is given in fig. 5.6.

### 5.5.1 Coil mechanics

The motion of the coil is governed by Newton's second law, where the external forces are the electromagnetic force on the actuator  $F_{act}$ , the spring force of the membrane  $F_m$ , and the force arising when a pressure difference exists across the membrane  $F_p$ . Denoting the mass of the coil, plunger and membrane  $M$  and letting  $x$  be the coordinate of displacement for the coil (positive when a positive pressure difference is generated in the chamber, i.e.



when liquid is pushed out), the three forces are given by

$$F_{\text{act}}(t) = \mathcal{K}_F I(t), \quad (5.3a)$$

$$F_m(t) = -\mathcal{K}x(t), \quad (5.3b)$$

$$F_p(t) = -\mathcal{A}_{\text{eff}}\Delta p(t), \quad (5.3c)$$

where the membrane is assumed to act as a linear spring with constant  $\mathcal{K}$ ,  $\Delta p(t)$  is the pressure difference across the membrane, i.e. the pressure difference relative to atmospheric pressure, and  $\mathcal{A}_{\text{eff}}$  is the effective plunger area. The plunger motion is then given by

$$M d_t^2 x(t) = \mathcal{K}_F I(t) - \mathcal{K}x(t) - \mathcal{A}_{\text{eff}}\Delta p(t), \quad (5.4)$$

and the coil velocity is found as  $v(t) = d_t x(t)$ .

### 5.5.2 Coil electric circuit

The coil electric circuit obeys the equation

$$\Delta U(t) = R_{\text{el}} I(t) + L_{\text{el}} \partial_t I(t) + \mathcal{E}(t), \quad (5.5)$$

where the resistance is the sum of the coil resistance  $R_{\text{el}}^{\text{coil}}$  and the outer resistance of  $R_{\text{el}}^{\text{out}} = 1.1512 \, \Omega$ , and  $\mathcal{E}(t)$  is the back-EMF arising from the moving coil, which is approximately given by  $\mathcal{E}(t) = \mathcal{K}_{\text{emf}} v(t)$ . The resistance and inductance of the coil are  $R_{\text{el}}^{\text{coil}} = 1.28 \, \Omega$  and  $L_{\text{el}} = 2.05 \times 10^{-4} \, \text{H}$  according to the data sheet, appendix C, which also lists  $\mathcal{K}_{\text{emf}} = 1.1 \, \text{V s m}^{-1}$ .

### 5.5.3 Chamber fluidics

During operation, the volume of the chamber  $\mathcal{V}_c$  depends on the position of the plunger and the expansion of the membrane due to the generated over-pressure in the chamber, but when the system is at rest, the volume of the chamber is  $\mathcal{V}_c = \mathcal{V}_{\text{init}}$ , see fig. 5.6. The plunger diameter is  $d = 7.05 \, \text{mm}$  while the chamber diameter is  $d = 9.00 \, \text{mm}$ , so a small free membrane area exists between the plunger and the chamber/holder walls. This part of the membrane will expand when a pressure difference is present across it due to the elastic nature of the membrane, and the expanded volume will be filled with fluid. Denoting the volume of fluid stored in the expanded membrane  $\mathcal{V}_{\text{tent}}$  — so named due to the resemblance of the expanded membrane to a tent — and noting that the volume displaced by the actuator is  $\mathcal{V}_{\text{disp}} = \mathcal{A}_{\text{eff}}x$ , the chamber volume is given by

$$\mathcal{V}_c = \mathcal{V}_{\text{tent}} - \mathcal{A}_{\text{eff}}x + \mathcal{V}_{\text{init}}. \quad (5.6)$$

The negative sign arises since a positive displacement of the plunger pushes liquid out of the chamber. Using arguments similar to those leading to eq. (5.2), the volume  $\mathcal{V}_{\text{tent}}$  is related to the generated over-pressure through a compliance as

$$\mathcal{V}_{\text{tent}} = C_{\text{tent}} \Delta p. \quad (5.7)$$

A positive flowrate  $Q_c$  exits the chamber when its volume is diminished, so this flowrate is found as the negative time-rate of change of eq. (5.6),

$$Q_c(t) = \mathcal{A}_{\text{eff}}v(t) - C_{\text{tent}} \partial_t \Delta p(t). \quad (5.8)$$

### 5.5.4 Pulsatile case

When run in AC mode — generating a pulsatile pressure and flowrate — the governing ODEs listed above simplify greatly. Assuming all time-dependent variables to vary harmonically, the governing equations become

$$Mi\omega v = \mathcal{K}_F I - \mathcal{K}x - \Delta p \mathcal{A}_{\text{eff}}, \quad (5.9a)$$

$$v = i\omega x, \quad (5.9b)$$

$$\Delta U = R_{\text{el}} I + i\omega L_{\text{el}} I + \mathcal{K}_{\text{emf}} v, \quad (5.9c)$$

$$Q_c = \mathcal{A}_{\text{eff}} v - i\omega C_{\text{tent}} \Delta p. \quad (5.9d)$$

These are four equations for the six unknown amplitudes  $x$ ,  $v$ ,  $\Delta U$ ,  $I$ ,  $\Delta p$  and  $Q_c$ , so two additional equations is required to solve the system. These equations are derived from the “fluidic loading” on the source, i.e. expressions for the flowrate and total pressure difference of the system driven by the source. However, the following equation for the generated over-pressure may be deduced from eq. (5.9)

$$\Delta p = \frac{\mathcal{K}_F I}{\mathcal{A}_{\text{eff}}} - \left( \frac{\mathcal{K}}{\mathcal{A}_{\text{eff}}^2} \frac{1}{i\omega} + \frac{M}{\mathcal{A}_{\text{eff}}^2} i\omega \right) v \mathcal{A}_{\text{eff}}, \quad (5.10)$$

which reveals that the actuator acts as a pressure source — as expected — with a maximum pressure of  $\Delta p_{\text{max}} = \mathcal{K}_F I / \mathcal{A}_{\text{eff}}$ . However, not all of the actuator force is deposited as pressure in the fluid, as some is used to accelerate the plunger and membrane. These time-dependent losses are observed to enter the fluid equations as a hydraulic inductance  $M/\mathcal{A}_{\text{eff}}^2$  and compliance  $\mathcal{A}_{\text{eff}}^2/\mathcal{K}$ . The compliance is a consequence of the spring behavior of the membrane but should not be confused with the aforementioned  $C_{\text{tent}}$ . Rather,  $\mathcal{A}_{\text{eff}}^2/\mathcal{K}$  should be thought of as another compliance in addition to  $C_{\text{tent}}$ , which arises because some of the coil force is required to elongate the (assumed Hookean) membrane, meaning that not all coil force is deposited in the fluidic system. Hence, the flowrate leaving the chamber is less than what would have been the case, if no force was required to elongate the membrane. This, in the view of the microfluidics, is the same as a storage of volume inside the chamber, and it is therefore not surprising to find the membrane elasticity enter into the equations as an additional compliance.

The EC diagram for the pressure source is shown in fig. 5.7 along with a symbol to be used for the pressure source in EC diagrams in the following chapters. This symbol, shown in panel (b), is to be understood to comprise eq. (5.9) as given in panel (a).

## 5.6 Pressure source performance

Rigorous testing of the developed pressure source has been completed to fully characterize its performance, and determine the values of the constants  $\mathcal{K}$ ,  $\mathcal{A}_{\text{eff}}$  and  $C_{\text{tent}}$ . It is shown in fig. 5.8(a) that the pressure source is capable of delivering a pulsatile pressure, in this case at 10 Hz.

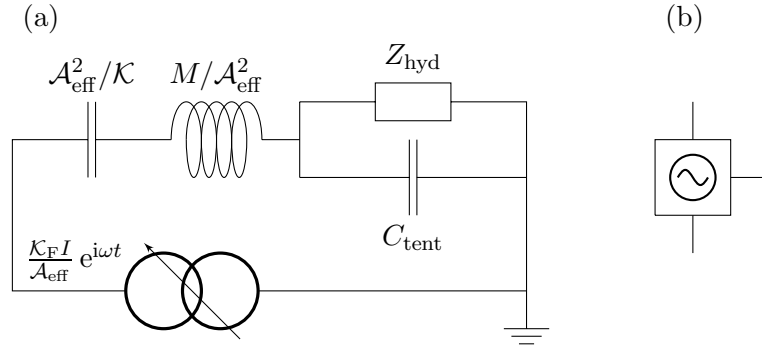


**Figure 5.7:** (a) EC diagram of the pressure source. The hydraulic inductance and compliance arising in the fluidic domain as a consequence of the moving plunger and membrane are included.  $Z_{\text{hyd}}$  is the “fluidic loading” of the system, i.e. the impedance of the fluidic system driven by the source. (b) Symbol for the pressure source to be used in EC diagrams in the rest of the thesis, shown with the three chamber outlets.

### 5.6.1 Frequency capability

Fig. 5.8(b) shows the over-pressure amplitude in the source chamber as a function of frequency, and gives an impression of the frequency capabilities of the pressure source. Filled with Milli-Q water, two of the chamber exits have been blocked and a pressure sensor (15 psi) is connected to the third via a teflon tube ( $\ell = 4.8$  cm,  $a = 0.125$  mm,  $h = 0.670$  mm). The figure shows the source delivers pulsatile pressures up to 800 Hz, with an attenuated resonance at  $f \approx 350$  Hz.

### 5.6.2 Effective area $\mathcal{A}_{\text{eff}}$

The pressure delivered by the source at different levels of coil electrical current has been measured using the same setup as above, but exposed to DC current. Upon specifying an upper current limit  $I_{\text{lim}}$  on the DC power generator, voltage was supplied to the actuator. The pressure was observed to build from atmospheric pressure to a constant value exceeding atmospheric pressure,  $p_{\text{end}}$ , see fig. 5.9(a), while the current rose to the specified limit. The experiment was conducted at several current limits, taking several measurements at each limit. The mean of  $p_{\text{end}}$  over all measurements made at the same  $I_{\text{lim}}$  depends linearly on said current as shown in fig. 5.9(b). It was shown in eq. (5.10) that the found corrections to the actuator force acts as transients (a hydraulic inductance and compliance, respectively), so at time  $t = \infty$  these effects will disappear and the generated over-pressure will satisfy  $\Delta p(t = \infty) = p_{\text{end}} = \mathcal{K}_F I_{\text{lim}} / \mathcal{A}_{\text{eff}}$ . Since the water cannot escape the system, all flowrates will be zero at  $t = \infty$ , so the pressure will be the same in the whole system.

Assuming the manufacturer-specified value of  $\mathcal{K}_F = 1.1 \text{ N A}^{-1}$  to be true, the effective area may be derived from the slope  $s$  of the curve in fig. 5.9(b), which satisfies  $s = \mathcal{K}_F / \mathcal{A}_{\text{eff}}$  (eq. (5.1)) with  $s = 1.45 \times 10^4 \text{ N A}^{-1} \text{ m}^{-2}$ . The effective area hence found to

$$\mathcal{A}_{\text{eff}} = \frac{\mathcal{K}_F}{s} = 76.10 \text{ mm}^2, \quad (5.11)$$

which corresponds to a radius of  $a_{\text{eff}} = 4.92$  mm. The chamber cavity radius is 4.50 mm

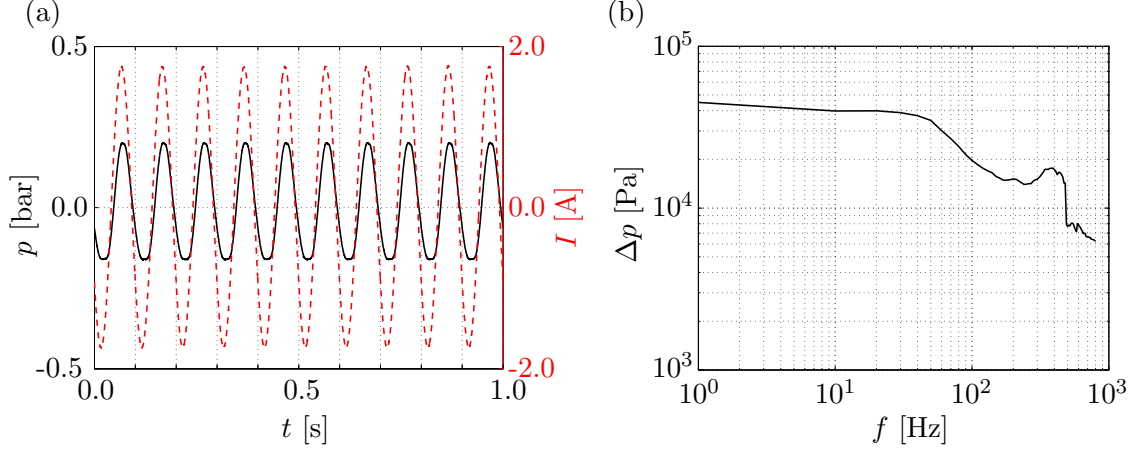


**Figure 5.8:** (a) Example of pressure source performance at  $f = 10$  Hz harmonically oscillating current, measured 4.8 cm from the chamber with the remaining two chamber exits closed. The pressure (solid curve) and current (dashed) oscillate slightly out of phase, but the generated pressure is clearly pulsatile. (b) Frequency dependence of pressure amplitude for pressure source operated at  $I = 1.7$  A. Resonance is found at  $f \approx 350$  Hz with a low Q-value suggesting much attenuation in the system. The pressure source is observed to deliver pressures in the kilopascal range for frequencies up to 0.8 kHz.

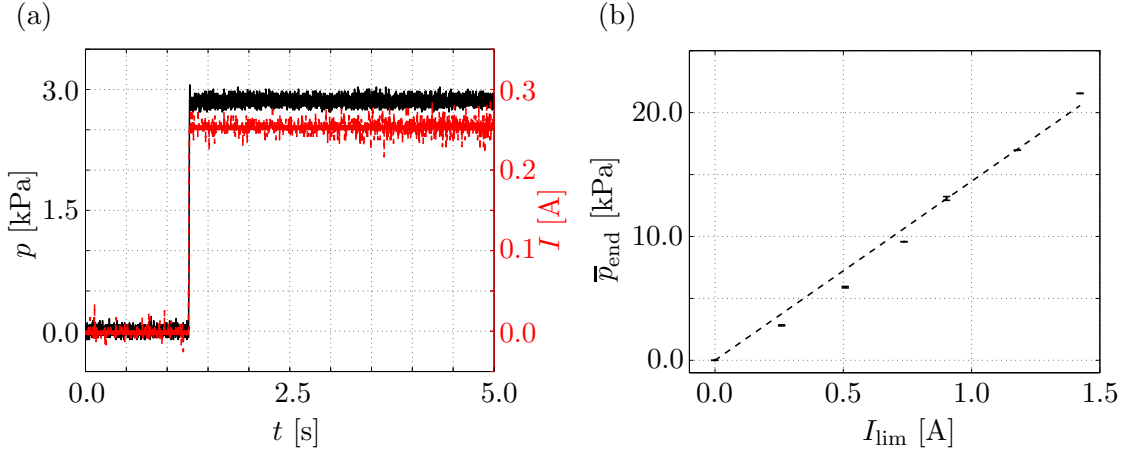


**Figure 5.9:** Measured pressure vs. DC coil current. (a) With a specified current limit  $I_{\text{lim}}$  on the DC power supply, the pressure source was switched on for a period of about 5 s. Pressure (solid) was observed to quickly built to a constant value  $p_{\text{end}}$  as current (dashed) built to the specified limit. The experiment was repeated at different current limits, conducting it several times at each current limit. (b) A linear dependence of the mean of the reached pressure  $p_{\text{end}}$  for all experiments at the same current limit on  $I_{\text{lim}}$  is observed. The slope of the linear curve fit (dashed) is  $s = 1.45 \times 10^4 \text{ N A}^{-1} \text{ m}^{-2}$ .

and the radius to the middle of the O-ring is 5.30 mm, so the effective radius is roughly the mean of the chamber cavity and center O-ring radii. This latter radius is where the membrane meets the actuator guide, so the effective area of eq. (5.11) is probable. The small deviations are likely inflicted since some of the applied pressure is absorbed in the sealing O-ring and some in the membrane, thus lowering the amount of pressure delivered to the fluid in the chamber.

### 5.6.3 Membrane spring stiffness $\mathcal{K}$

The membrane is assumed to work as a linear spring on the plunger, which is the crudest approximation that still captures the essentials of the phenomenon. The associated spring stiffness  $\mathcal{K}$  of the membrane is not easily found from theoretical considerations, as the plunger is attached at the middle of the membrane and the membrane shape changes during operation. It may, however, be determined from an easy experiment. Using a DC current with two of the three pressure source chamber exits blocked, the pressure source is used to displace a Milli-Q water front in a long transparent tube of radius  $a = 0.30$  mm connected to the third chamber exit. The results are given in fig. 5.10.

The water front stops when equilibrium is reached, which according to eq. (5.4) happens when

$$\mathcal{K}x = \mathcal{K}_F I. \quad (5.12)$$

The plunger displacement  $x$  is deduced from the displacement of the water front  $\Delta\ell$  since all volume changes in the pressure source chamber must exit through the tube, so  $\mathcal{A}_{\text{eff}}x = \pi a^2 \Delta\ell$ . The linear curve fit to the experimental data of fig. 5.10 thus obeys  $\Delta\ell = sI$  where  $s = 2.70 \times 10^{-2}$  m A<sup>-1</sup>, so the membrane stiffness is found from

$$\mathcal{K} = \frac{\mathcal{A}_{\text{eff}} \mathcal{K}_F}{\pi a^2 s}. \quad (5.13)$$

The value of the constant is  $\mathcal{K} = 1.10 \times 10^4$  N m<sup>-1</sup>, which is much higher than expected. A piece of silicone rubber of height 0.2 mm and length 16.0 mm with  $E = 2.05 \times 10^6$  Pa deforming the maximum stroke length of 2.03 mm has a spring constant of

$$\mathcal{K} \approx \frac{2.05 \times 10^6 \text{ Pa} \times 0.2 \times 10^{-3} \text{ m} \times 16.0 \times 10^{-3} \text{ m}}{2.03 \times 10^{-3} \text{ m}} \approx 6.6 \times 10^3 \text{ N m}^{-1}, \quad (5.14)$$

and since the membrane is not elongated in the axial direction, but at an angle, the spring constant is expected to be below the this. However, the two separate measurement series conducted on two separate dates strongly indicate otherwise.

### 5.6.4 Membrane compliance $C_{\text{tent}}$

The compliance of the pressure source membrane is difficult to characterize from theoretical considerations alone since, as shown above, there is a strong interdependence between fluid pressure, plunger displacement, and electrical current.  $C_{\text{tent}}$  may, however, be determined experimentally by use of the analogies to an electric circuit.

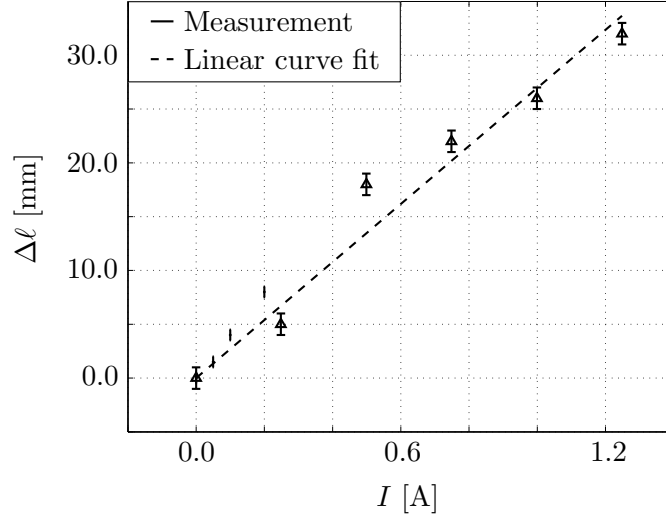


**Figure 5.10:** Displacement of water front as a function of DC current. The simple circuit model assumes the membrane acts as a linear spring, although this is probably not the case. However, a linear approximation to the data is used (dashed) which is a fair approximation. Two data sets are shown, taken at different dates (dots and triangles), which agree on the behavior. The slope of the fit is  $s = 2.70 \times 10^{-2} \text{ m A}^{-1}$ .

Mounting a pressure sensor to one of the chamber exits and a syringe filled with Milli-Q water to another chamber exit while blocking the remaining exit, an over-pressure is generated in the chamber by the syringe. This will decay exponentially to zero when the syringe piston is released, since the resistance thoroughly dominates in this setup, so the time constant of the decay is given by  $\tau = R_{\text{hyd}}C_{\text{tent}}$  by direct analogy to an electric  $RC$ -circuit. A thick-walled PEEK tube segment ( $\ell = 9.38 \text{ cm}$ ,  $a = 0.063 \text{ mm}$ ) of negligible compliance connected the syringe and chamber. An example of a pressure reading and the derived values for  $C_{\text{tent}}$  are given in fig. 5.11.

The compliance is found to decrease as the applied pressure difference increases, since it becomes increasingly more difficult to further expand the membrane. A second order polynomial fit to the data is

$$C_{\text{tent}}(\Delta p) \approx s_1 \Delta p^2 + s_2 \Delta p + s_3, \quad (5.15)$$

with  $s_1 = 1.6801 \times 10^{-23} \text{ m}^3 \text{ Pa}^{-3}$ ,  $s_2 = -3.1971 \times 10^{-18} \text{ m}^3 \text{ Pa}^{-2}$  and  $s_3 = 2.9927 \times 10^{-13} \text{ m}^3 \text{ Pa}^{-1}$ . However, given the small variation in  $C_{\text{tent}}$  and the level of approximation otherwise used, a mean value of  $C_{\text{tent}} \approx 2.0 \times 10^{-13} \text{ m}^3 \text{ Pa}^{-1}$  is used in the following chapters.

## 5.7 Summary

A pressure source has been constructed based on a linear voice coil actuator. The pressure source has been shown to work in both AC and DC, generating pulsatile pressure in the AC

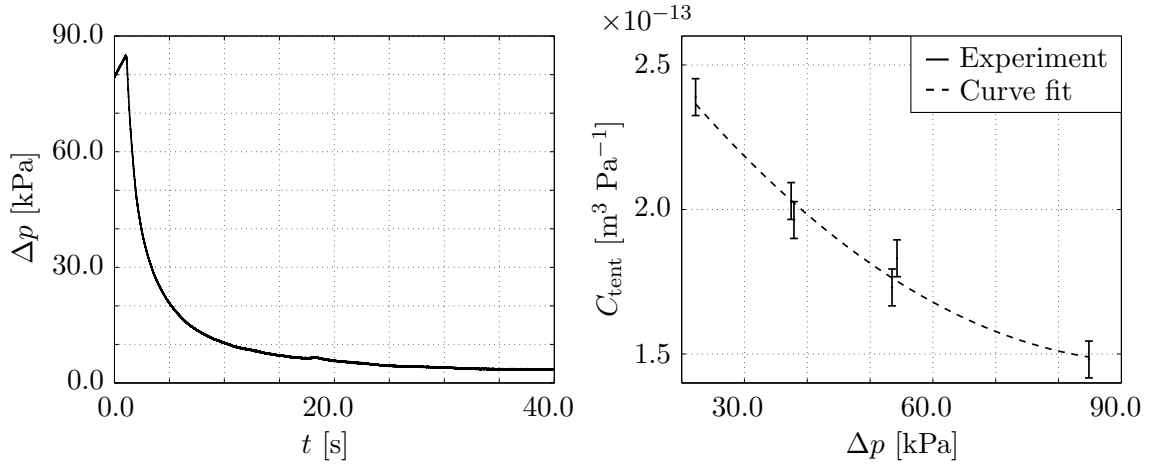


**Figure 5.11:** Experimental results for  $C_{\text{tent}}$  determined from the decay time of pressure. (a) A pressure reading shows the pressure decays exponentially, in this case with time constant  $\tau \approx 2.3$  s. (b) Computed values for  $C_{\text{tent}}$  for different pressure levels. The compliance decreases as pressure increases since it becomes increasingly more difficult to further expand the membrane. A second order curve fit (dashed) indicates the dependence with fitting parameters given in text.

case into the low kilohertz range as expected. A circuit model has been presented for the coupled electric, mechanic and microfluidic physics governing the pressure source. This model shows that not all actuator force is deposited as pressure in the fluid: some is used to accelerate the pressure source plunger and some is used to counteract the membrane elasticity. The compliance  $C_{\text{tent}}$  and spring constant  $\mathcal{K}$  of the membrane are determined experimentally along with the effective area of the plunger,  $\mathcal{A}_{\text{eff}}$ .





## Chapter 6

# Pulsatile flow detected by bubble motion

The motion of an air bubble in a water-filled tube exposed to a pulsatile pressure was studied to understand and quantify the agreement between experiment and systems-level modeling of a pulsatile flow, as well as to build confidence in the performance of the pressure source. The bubble motion was recorded using a high-speed camera.

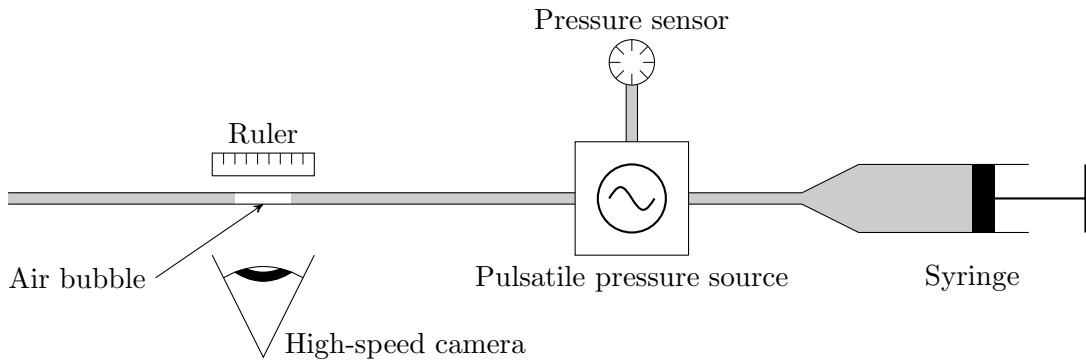


**Figure 6.1:** Schematic of the experimental setup. The pressure source is represented by the symbol introduced in chapter 5.

## 6.1 Experimental setup and method

### 6.1.1 Setup

A pressure sensor was connected to one of the three chamber outlets through a teflon tube ( $\ell_{\text{sens}} = 4.1$  cm,  $a_{\text{sens}} = 0.125$  mm,  $h_{\text{sens}} = 0.669$  mm) and a water-filled 10 mL syringe (filled to 8.1 mL) to another of the outlets via a teflon tube of dimensions  $\ell_{\text{syr}} = 17.5$  cm,  $a_{\text{syr}} = 0.125$  mm and  $h_{\text{syr}} = 0.669$  mm. A long transparent tube ( $\ell = 42.9$  cm,  $a = 0.254$  mm,  $h = 0.540$  mm) was connected to the last chamber outlet, allowing the tube to

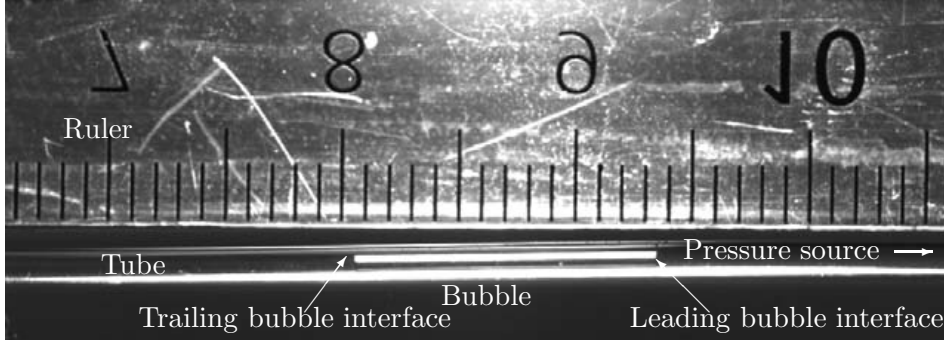


**Figure 6.2:** Example of raw bubble image from the camera showing part of the tube exiting the pressure source chamber; the right end of the tube is connected to the pressure source while the left end is left in atmospheric conditions. The bubble is found roughly in the middle of the tube. A mm-scale ruler (inverted and mirrored) is positioned above the tube.

exit into atmospheric conditions. The bubble (relaxed axial length  $\ell_{\text{bub}} = 1.35 \text{ cm}$ ) was placed in this tube, roughly halfway between the chamber and the tube outlet. A metric ruler was placed next to the tube and just above the bubble for scale. The pressure source is to the right in all pictures in the following and a schematic illustration of the setup is shown in fig. 6.1.

The bubble motion was detected using a high-speed camera fitted with a 1:2.8D lens, with dedicated software used for storage and movie generation. Individual gray scale images were stored in `tiff` format and movies in `avi` format, for a time interval comprising several oscillation periods. Pictures were framed at 1 kHz sampling rate for pressure oscillations up to 100 Hz. An example of an image is given in fig. 6.2. The photographic setup was designed by Ulrik Ullum of Novo Nordisk A/S.

The pressure source was operated with the equipment detailed in chapter 5, generating only sinusoidal pressures.

### 6.1.2 Instrumentation

**Tubing:** Upchurch Scientific (Upchurch Scientific Inc., Oak Harbor, Washington, USA) teflon tubing of various lengths and inner diameters but all of 1/16" (1.588 mm) outer diameter.

**Camera:** Photron (Photron USA Inc., San Diego, California, USA) Fastcam APX RS high-speed camera with dedicated Photron Fastcam software used for storage and movie generation.

**Lens:** Nikon (Nikon Corp., Imaging Company, Tokyo, Japan) AF Micro Nikkor 1:2.8D lens.

### 6.1.3 Method

The bubble position was adjusted using the syringe. Once in place and with a specified pressure frequency and framing rate, the AC generator and camera were activated almost simultaneously. Images were taken for 6 s, after which the supply voltage to the pressure source was turned off. The experiment was conducted at two different pressure amplitudes at the frequencies 1 Hz, 10 Hz, 15 Hz, 20 Hz, 30 Hz, 50 Hz and 100 Hz.

As the pressure source and camera were not activated at the exact same time, the pressure data and images were not directly correlated. However, the pressure amplitude at the sensor may be obtained from the pressure measurements, and the motion of the bubble interfaces may be related to the flowrates up- and downstream of the bubble, which in turn depend on said pressure amplitude. Hence, systems-level modeling and experimental data can be compared to test the applicability of the model.

## 6.2 Image processing routine

An image processing routine has been developed in MATLAB to deduce the motion of the air-water interfaces. Upon loading the raw `tiff` image and converting it to black/white (represented as 0 and 1, respectively), the routine searches for the first white pixel in a specified region. This first pixel of the bubble is approximately the position of the boundary and has the numerical value 1, see fig. 6.3, so the routine searches for the first pixel with value above 0.5. The position of this pixel is stored and the routine continues to the next image in the set. The search region is rectangular and specified by selecting the coordinates of the diagonal corners of the region in the black/white image.

This analysis is done for both left and right bubble interface, and finally, the positions of both interfaces are plotted versus time to yield a figure like those in fig. 6.5. A scale is found as the horizontal distance between two millimeter marks on the ruler in the first image of the set. The steps of the image processing routine are illustrated in fig. 6.3, where the found positions of the interface are shown for the first image of the data from the experiment with  $f = 20$  Hz.

### 6.2.1 Pixelation and resolution

When using a digital camera to record the bubble position as a function of time, the actual smooth bubble motion is recorded as a piece-wise constant motion with the step-size given by the resolution of the setup used. In general, the resolution along an coordinate direction  $x_i$  is given by

$$\Delta x_i = \frac{N}{\ell}, \quad (6.1)$$

where  $N$  is the total number of pixels in the direction, and  $\ell$  is the physical distance in the same direction, which is recorded in the image. For the present case, the horizontal resolution in the images is  $\Delta x_{\text{hor}} = 4.00 \times 10^{-2} \text{ mm pixel}^{-1}$  since  $\ell = 40.5 \text{ mm}$  and  $N = 1024 \text{ pixel}$ .

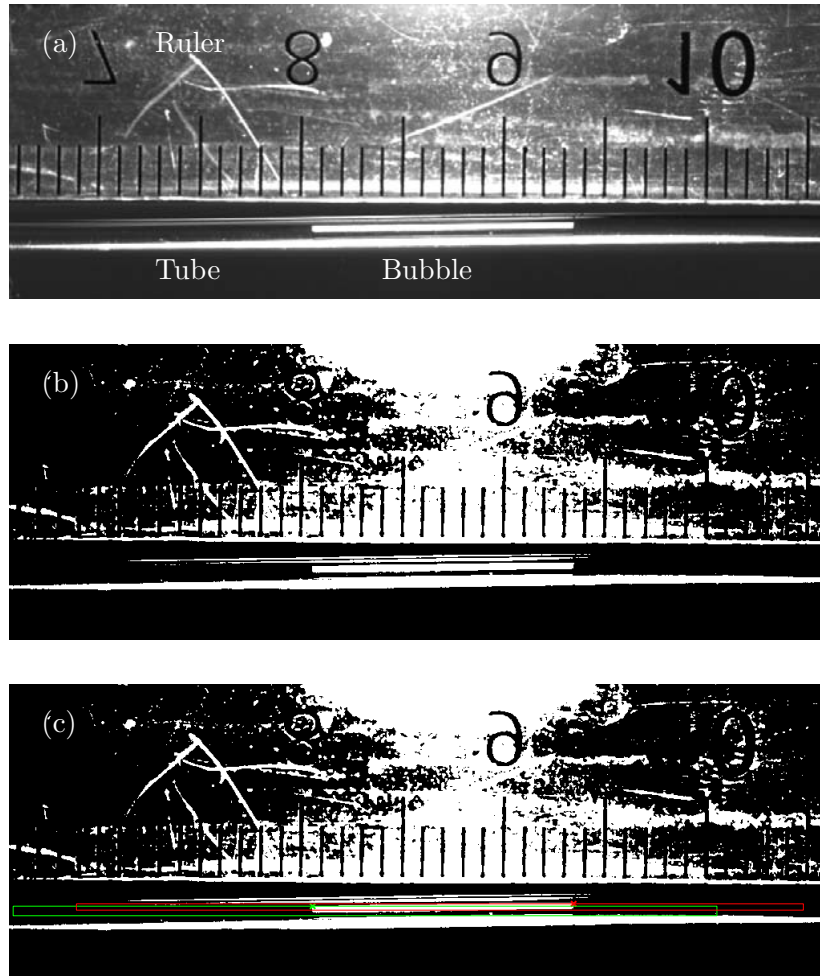


**Figure 6.3:** Steps of the image processing routine. (a) The grayscale `tiff` image is loaded into MATLAB and (b) converted to black/white. (c) The result of the routine: the left and right air-liquid interfaces are marked by green and red crosses. The boxes show the regions in which the routine searches for the interfaces, in the same color coding as the crosses.

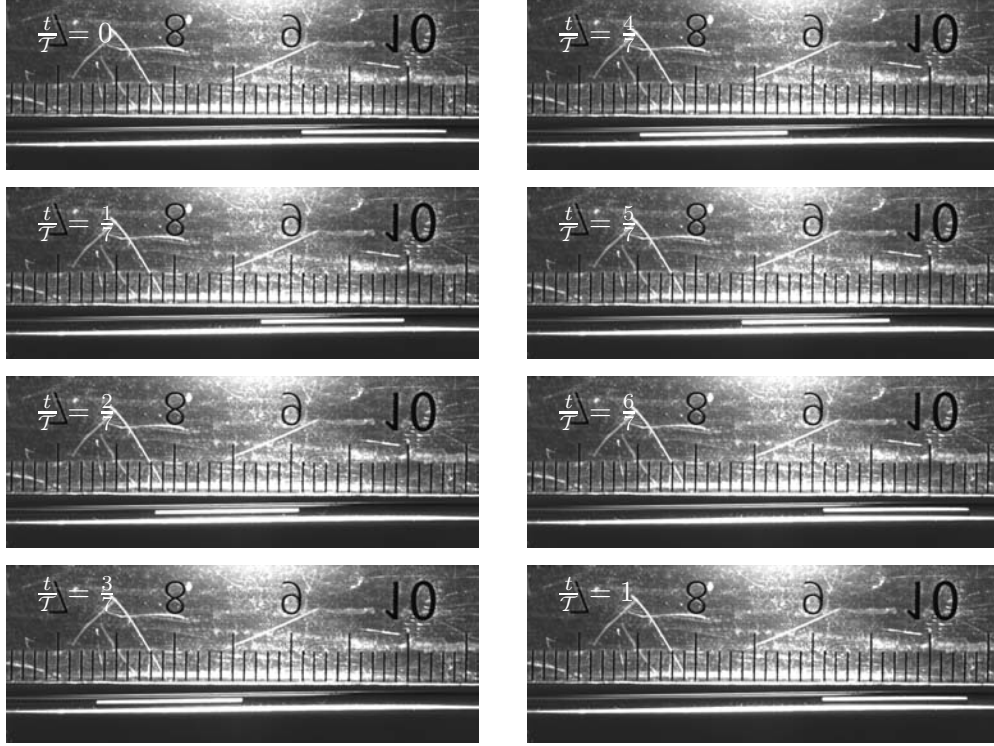


**Figure 6.4:** Selected snapshots of bubble motion during one oscillation period at  $f = 1$  Hz in steps of  $T/7$ . The bubble is displaced almost the entire length of tube in the field of view of the camera, during the period.

A digital image is said to be pixelated when the pixels become observable, [54]. For the present case, this would be the case when the displacements of the bubble interfaces become of the same order as the resolution.

### 6.3 Motion of air-water interfaces

A time-series of one period for the experiment at 1 Hz frequency is given in fig. 6.4. The bubble moves noticeably during the oscillation, but the bubble volume does not change substantially during one such period.

Fig. 6.5 shows the motion of the bubble boundaries for the frequencies 1 Hz, 30 Hz, 50 Hz and 100 Hz, as detected from the image processing routine. The bubble oscillates about an equilibrium position so the graphs show both the absolute motion as well as the relative motion of the boundaries about said position. The absolute motion is given in terms of the distance  $x_{\text{abs}}$ , which is the distance from the left image boundary, i.e. the left-most column of pixels in the images, to either of the two bubble interfaces. The

relative, or oscillatory motion, defined from the distance  $x_{\text{abs}}$  as

$$x_{\text{rel}}(t) = x_{\text{abs}}(t) - \bar{x}_{\text{abs}}(t), \quad (6.2)$$

where the mean is taken over the number of periods shown in the figures.

### 6.3.1 Observed motion

At  $f = 1$  Hz the leading and trailing interface move in phase and are displaced the same distance throughout the oscillation period, which is evident from fig. 6.5(a)-(b). The motion is almost sinusoidal, although a noticeable — and repeatable — deviation is observed at the regions of maximum positive displacement (i.e. at  $t \approx 1$  s and  $t \approx 2$  s in fig. 6.5(a)). Interestingly, the interfaces have a slightly larger displacement amplitude when moving backwards (i.e. when the pulsatile pressure component is negative); it is during the subsequent forward motion a kink is observed in the otherwise sinusoidal displacements.

The motion of both interfaces at 30 Hz actuation is still sinusoidal, and a phase-shift is observed between the two as well as a large amplitude difference, not only between the case of 1 Hz actuation and this present 30 Hz actuation, but also between the two interface displacements at 30 Hz. Of special note is that the trailing interface has the larger displacement amplitude (almost twice that of the leading interface displacement), indicating a resonance. A small drift in the bubble position is evident in panel (d), although only a total displacement of about 0.5 mm is observed over the 10 periods shown in the figure.

The occurrence of a resonance close to 30 Hz is further indicated by the dramatically diminishing trailing interface displacement at  $f = 50$  Hz, along with a phase-shift of almost  $\pi/2$ , while the leading interface displacement is roughly the same. At 100 Hz very little motion is detected by the leading interface and none by the trailing, as is the case at frequencies above resonance.

Pixelation is observed in the relative motion at 50 Hz and 100 Hz, in the latter case in both time and space. The resolution was found to  $0.04 \text{ mm pixel}^{-1}$  which is clearly observable in fig. 6.5(h). It cannot be ruled out that the trailing interface did oscillate, only that the motion must have been below 0.04 mm. The kinks on the trailing interface motion curve are a result of this, and not of motion exceeding the resolution, as is the flat apices on the leading interface motion curve. Since the images were framed at 1 kHz, there are only 10 images per period of the bubble motion at  $f = 100$  Hz, which is obvious in fig. 6.5(h), so temporal pixelation is also found in this case.

### 6.3.2 Physical interpretation of the observed motion

To interpret the observed resonance frequency at  $f_0 = 30$  Hz, the physical system of the bubble in the long, water-filled tube is analyzed as an electric *RCL*-circuit, just like the abruptly started Poiseuille flow of chapter 4, and therefore has the three regular resonance frequencies. Since  $f_0 \approx 30$  Hz, the critical Womersley number is  $\alpha_c = 1.45$  and inertia thus dominates, and consequently, the observed resonance is believed to be of the *LC*-type.

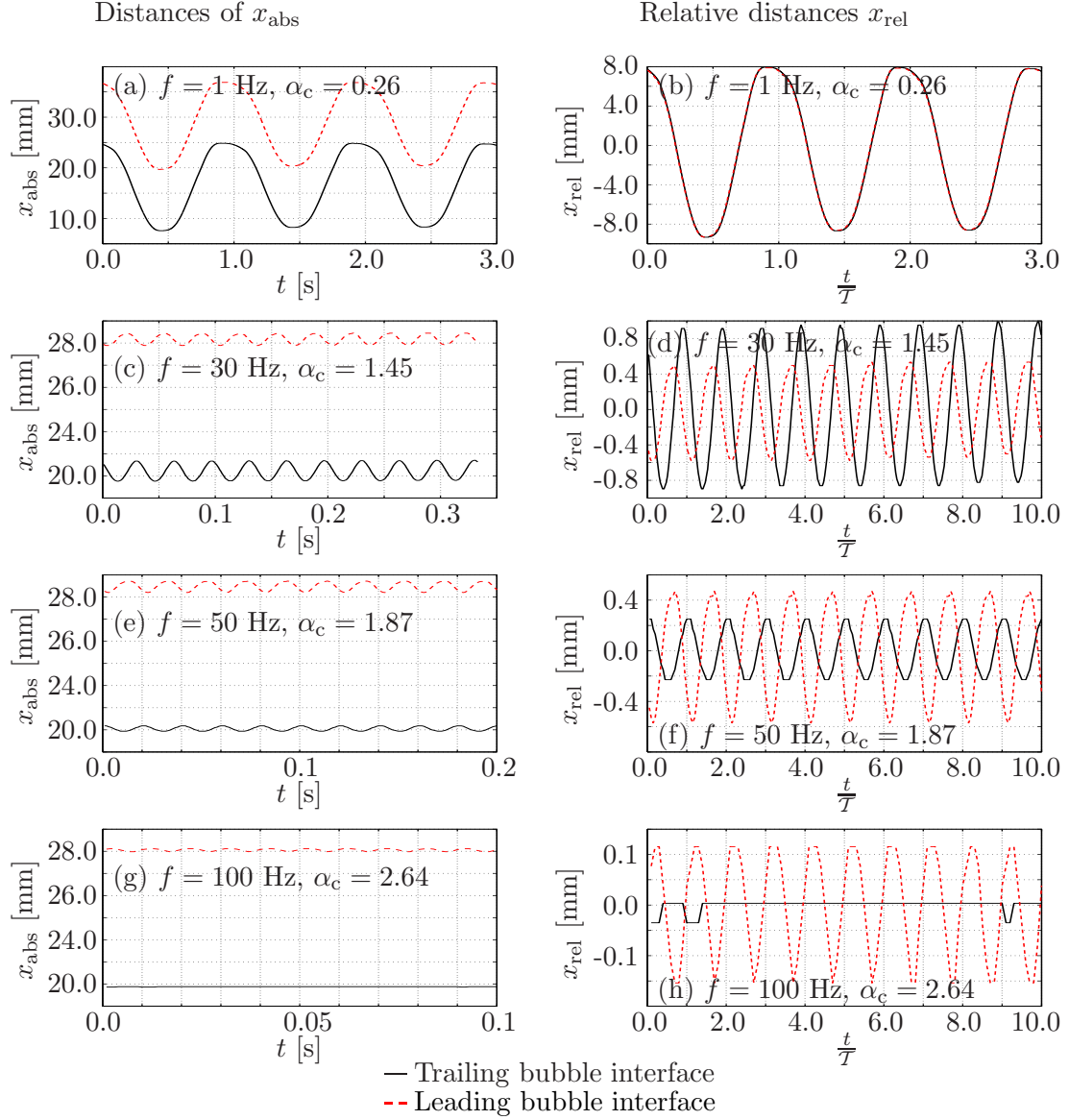


**Figure 6.5:** Motion of bubble interfaces as detected by the image processing routine for selected frequencies. Left column (panels (a), (c), (e) and (g)) gives the distance of the bubble interfaces from the distance of the left image boundary, while the right column (panels (b), (d), (f) and (h)) shows the same data only with the mean of the distance for each interface subtracted, and plotted versus normalized time. The effect of pixelation is observed in the trailing bubble interface (black line) in (h).

Using the simple expression for  $L_{\text{hyd}}$  of eq. (2.21)  $f_0$  is calculated to be

$$f_0 = \frac{1}{2\pi\sqrt{L_{\text{hyd}}C_{\text{bub}}}} = 30.86 \text{ Hz}, \quad (6.3)$$

which is in good agreement with the experimental observation of  $f_0 \approx 30 \text{ Hz}$ . The  $RC$ -resonance frequency of the system is

$$f_0 = \frac{1}{2\pi R_{\text{hyd}}C_{\text{bub}}} = 48.08 \text{ Hz}, \quad (6.4)$$

which will never be observed, since the critical Womersley number for the system at  $f = 48.08 \text{ Hz}$  is  $\alpha_c = 1.83$ , where the system is dominated by inertia and the resistance can be neglected. The  $LR$ -resonance is the inverse of the characteristic time which enters into the definition of  $\alpha_c$ . At  $\alpha_c = 1$  this relaxation time and  $\omega$  are identical, so only for  $\alpha_c < 1$  does the system have time for the  $LR$ -resonance to occur.

## 6.4 Equivalent circuit model

The motion of gas bubbles in liquids has been studied extensively in the literature. Most work fall in one of two categories: bubble motion as caused by liquid flow driven by a constant pressure gradient, [55, 56, 57, 58, 59], or cavitation of small bubbles when exposing a system to ultrasound pressure fluctuations, [60]. The current work falls under neither category, and will be modeled using EC theory.

The system consists of four parts: the pressure source, the syringe and connecting tubing, the pressure sensor and connecting tubing, and the tubing with the bubble. The pressure sensor is connected to the chamber through a teflon tube, as described in sec. 6.1.1. In addition to the regular Womersley-type impedance describing resistance and inertia in the tube, a compliance element  $C_{\text{wall}}$  must also be included in the model of the tubing due to the elastic behavior of the teflon wall. Moreover, the pressure sensor is also known to be compliant with the parameter  $C_{\text{sens}}$ , and the inertia of the water contained in the sensor is also included.

The elastic walls have been modeled as described in sec. 3.4.1 as two rigid tube segments with a compliant point placed between them, while the sensor has been modeled as a hydraulic inductance in series with the sensor compliance. The inductance is included since the flow must be accelerated to generated a detectable pressure difference at the sensor. The symbol  $Z_{\text{Wom}}$  is used instead of the more correct  $Z_{\text{Wom}}/2$  for convenience.

The syringe is connected to the pressure source chamber using the same teflon tubing as for the pressure sensor, which is modeled in accordance with the discussion above. In theory, the connecting tubing and the syringe should each be modeled using individual Womersley-type impedances and compliances, however, the syringe itself has a much larger radius than the tubing, so the syringe inertia and resistance may be neglected to a good approximation, but its compliance cannot. The wall compliance of eq. (3.13) depends on  $a^3$ , so while resistance and inertia can readily be neglected, syringe compliance cannot. Although care was taken in keeping the system free of air bubbles, a small bubble was



**Table 6.1:** Numerical values for the circuit elements in simple EC model at  $f = 1$  Hz computed from the parameters previously mentioned. The compliance of the pressure sensor has been estimated in sec. 5.4.3 and the inertia of the water in the sensor is estimated by setting the radius to 2.0 mm and the length to 8.0 mm. SI units have been used ( $[Z_{\text{Wom}}] = \text{Pa s m}^{-3}$ ,  $[L_{\text{hyd}}] = \text{Pa s}^2 \text{ m}^{-3}$ ,  $[C_{\text{hyd}}] = \text{m}^3 \text{ Pa}^{-1}$ ).

Element	Value	Element	Value
$Z_{\text{Wom}}^{\text{sens}}$	$3.40 \times 10^{11} + i 5.54 \times 10^9$	$C_{\text{wall}}^{\text{sens}}$	$1.90 \times 10^{-17}$
$Z_{\text{Wom}}^{\text{syrr}}$	$9.14 \times 10^{11} + i 1.49 \times 10^{10}$	$C_{\text{wall}}^{\text{syrr}}$	$5.12 \times 10^{-17}$
$Z_{\text{Wom}}^{\text{up}}$	$6.59 \times 10^{11} + i 4.43 \times 10^9$	$C_{\text{wall}}^{\text{up}}$	$2.84 \times 10^{-16}$
$Z_{\text{Wom}}^{\text{down}}$	$6.13 \times 10^{11} + i 4.13 \times 10^9$	$C_{\text{wall}}^{\text{down}}$	$2.65 \times 10^{-16}$
$L_{\text{bub}}$	$7.99 \times 10^4$	$C_{\text{bub}}$	$2.70 \times 10^{-14}$
$L_{\text{sens}}$	$1.25 \times 10^6$	$C_{\text{sens}}$	$1.67 \times 10^{-15}$
		$C_{\text{air}}$	$6.46 \times 10^{-16}$

observed in the syringe as the experiments were carried out. This bubble is included in the model.

The compliant bubble is trapped in the tubing, which itself is compliant. Upstream of the bubble, the flowrate entering the tube from the pressure source chamber can either flow downstream to the bubble or expand the tube wall. The former then branches off into a component compressing the air bubble and a component continuing downstream. This last flowrate finally branches into two: one continuing out of the tube and a second expanding the tube downstream of the trapped air bubble. In addition to compliance, bubble inertia  $L_{\text{bub}}$  is included in the model since at high frequencies, this may not be neglected. The full model may now be constructed from the submodels above; the diagram is given in fig. 6.6, while table 6.1 lists the values of the circuit elements at  $f = 1$  Hz.

In the experiments, the pressure  $p_{\text{sens}}(t)$  and the electric coil current is measured. Using systems-level analysis, this pressure may be related to the pressure in the pressure source chamber,  $p_c(t)$ , and subsequently to the pressure in the imaged air bubble,  $p_{\text{bub}}(t)$ . Assuming all pressures can be represented as  $p(t) = \Delta p e^{i\omega t} + p_0$ , the pressure amplitudes at the chamber and sensor are related by

$$\Delta p_c = \left[ (i\omega C_{\text{wall}}^{\text{sens}} Z_{\text{Wom}}^{\text{sens}} + 1) (i\omega C_{\text{sens}} Z_{\text{Wom}}^{\text{sens}} + 1 - \omega^2 C_{\text{sens}} L_{\text{sens}}) + i\omega C_{\text{sens}} Z_{\text{Wom}}^{\text{sens}} \right] \Delta p_{\text{sens}}. \quad (6.5)$$

Similarly, a relation may be established between the over-pressures at the chamber and the bubble:

$$\Delta p_c = [i\omega C_{\text{wall}}^{\text{up}} Z_{\text{Wom}}^{\text{up}} + 2] \Delta p_{\text{up}} - \Delta p_{\text{bub}}, \quad (6.6)$$

where

$$\Delta p_{\text{up}} = \left[ i\omega C_{\text{bub}} Z_{\text{Wom}}^{\text{up}} \left( 1 - \frac{\omega^2 L_{\text{bub}} C_{\text{bub}}}{\omega^2 L_{\text{bub}} C_{\text{bub}} - 1} \right) + \frac{Z_{\text{Wom}}^{\text{up}}}{Z_{\text{Wom}}^{\text{down}}} - \frac{Z_{\text{Wom}}^{\text{up}}}{i\omega C_{\text{wall}}^{\text{down}} Z_{\text{Wom}}^{\text{down}2} + 2 Z_{\text{Wom}}^{\text{down}}} + 1 \right] \Delta p_{\text{bub}}. \quad (6.7)$$

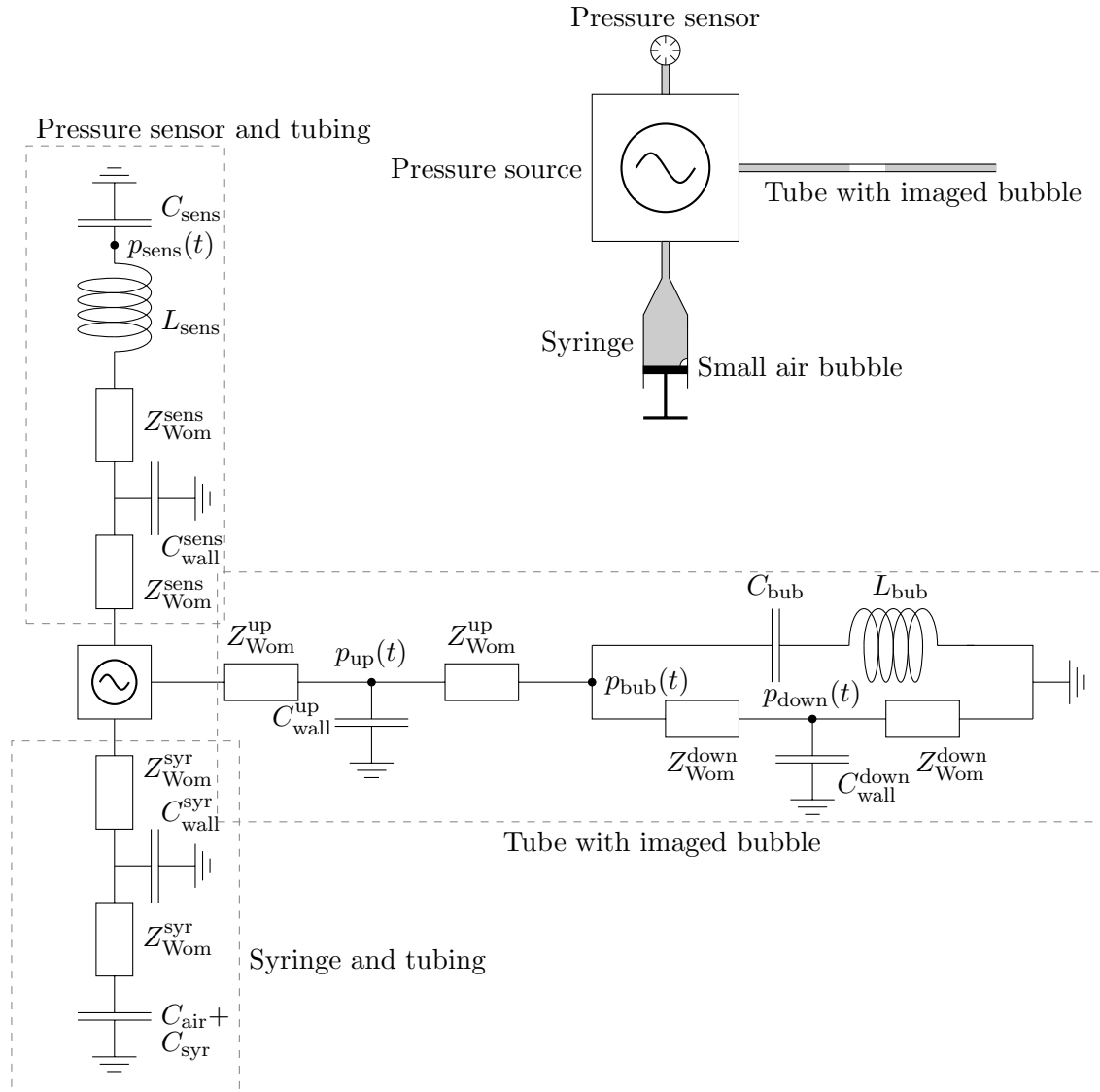


**Figure 6.6:** The full EC model of the bubble experiments. The elastic walls and the pressure source have been modeled as discussed previously, and the compliances of the syringe and the air bubble contained in it may be added due to the linearity of the governing equations. Inertia of the water in the pressure sensor and of the bubble has also been included.

The amplitudes of the flowrates  $Q_{\text{up}}(t)$  and  $Q_{\text{down}}(t)$  may be found from

$$Q_{\text{up}} = \frac{\Delta p_{\text{up}} - \Delta p_{\text{bub}}}{Z_{\text{Wom}}^{\text{up}}}, \quad (6.8a)$$

$$Q_{\text{down}} = \frac{\Delta p_{\text{bub}} - \Delta p_{\text{down}}}{Z_{\text{Wom}}^{\text{down}}}, \quad (6.8b)$$

once the pressures  $\Delta p_c$ ,  $\Delta p_{\text{bub}}$  have been determined along with the pressure

$$\Delta p_{\text{down}} = \frac{1}{i\omega C_{\text{wall}}^{\text{down}} Z_{\text{Wom}}^{\text{down}} + 2} \Delta p_{\text{bub}}. \quad (6.9)$$

The displacement of the bubble interfaces may be derived from these flowrates since  $\mathcal{V} = \int Q(t) dt$  and  $\mathcal{V} = \pi a^2 x_{\text{rel}}$ , where  $x_{\text{rel}}$  is the relative motion of the bubble interface as discussed in sec. 6.3

$$x_{\text{rel}}^{\text{LI}} = \frac{Q_{\text{up}}}{i\omega \pi a_{\text{up}}^2}, \quad (6.10a)$$

$$x_{\text{rel}}^{\text{TI}} = \frac{Q_{\text{down}}}{i\omega \pi a_{\text{down}}^2}. \quad (6.10b)$$

The superscript ‘LI’ is used for the leading interface and similarly ‘TI’ for the trailing interface.

Pressure sensing and image capturing was done independently of each other during experimentation, so the predicted phase-lags between pressure and bubble interface displacements of the model cannot be tested versus the experiments. However, the phase-shifts between the bubble interfaces can, and it is expected that agreement in one such part of the model is associated with agreement in all parts of the model.

#### 6.4.1 Model shortcomings

All circuit elements depend linearly on the axial length  $\ell$  of the modeled quantity, e.g.  $R_{\text{hyd}} = 8\eta\ell/(\pi a^4)$ . These lengths are assumed constant in the model, but should be allowed to change due to the motion of the bubble. For the experiments at  $f = 1$  Hz the total bubble movement is about 2 cm while the axial lengths of the tubing up- and downstream of the bubble are roughly 20 cm, so significant deviation (about 10 %) of the numerical value of the circuit elements is expected. Thus, using constant lengths will introduce noticeable deviations between experiment and model result, although the order of magnitude will be the same. For the experiments at the higher frequencies, the total bubble motion is below 2 mm, so there will be only negligible changes in the circuit elements during an oscillation period. Hence, using constant lengths in the circuit elements is justifiable except for the case of  $f = 1$  Hz. The constant axial length is also a concern for the air bubble. As the experiments indicate, the bubble length is only constant for low frequencies, but has been modeled as such for all frequencies.

### 6.4.2 Extending the model

The model may be extended by using the continuum limit for the EC models of the elastic tubes, as discussed in chapter 3. The overall model does not change substantially but the mathematics become a little more elaborate. Most notably is the departure from the regular linear interdependence of flowrates and pressure amplitudes. Using the model outlined above and the relations of sec. 3.4.3, one may arrive at the equations below. The usual subscripts (e.g. ‘sens’) are used on the wave numbers  $k$  for distinction, the circuit elements per unit length are indicated by a hat as usual, and the flowrates and pressures are evaluated at the same positions as in the model above, e.g.  $Q_{\text{down}}$  below is evaluated at the bubble and is hence the same as the flowrate  $Q_{\text{down}}$  of eq. (6.8b):

$$\Delta p_c = \left[ \cos(k_{\text{sens}}\ell_{\text{sens}}) (1 - \omega^2 C_{\text{sens}} L_{\text{sens}}) + \frac{\hat{Z}_{\text{Wom}}^{\text{sens}} \sin(k_{\text{sens}}\ell_{\text{sens}})}{k_{\text{sens}}} i\omega C_{\text{sens}} \right] \Delta p_{\text{sens}}, \quad (6.11a)$$

$$\Delta p_c = \left[ \cos(k_{\text{up}}\ell_{\text{up}}) - \frac{\hat{Z}_{\text{Wom}}^{\text{up}} \sin(k_{\text{up}}\ell_{\text{up}})}{k_{\text{up}}} \frac{i\omega C_{\text{bub}}}{\omega^2 L_{\text{bub}} C_{\text{bub}} - 1} + \frac{\hat{Z}_{\text{Wom}}^{\text{up}}}{\hat{Z}_{\text{Wom}}^{\text{down}}} \frac{k_{\text{down}}}{k_{\text{up}}} \sin(k_{\text{up}}\ell_{\text{up}}) \cot(k_{\text{down}}\ell_{\text{down}}) \right] \Delta p_{\text{bub}}, \quad (6.11b)$$

$$Q_{\text{up}} = \frac{k_{\text{up}}}{\hat{Z}_{\text{Wom}}^{\text{up}}} \left[ \Delta p_{\text{bub}} \cot(k_{\text{up}}\ell_{\text{up}}) - \frac{\Delta p_c}{\sin(k_{\text{up}}\ell_{\text{up}})} \right], \quad (6.11c)$$

$$Q_{\text{down}} = -\frac{k_{\text{down}}}{\hat{Z}_{\text{Wom}}^{\text{down}}} \cot(k_{\text{down}}\ell_{\text{down}}) \Delta p_{\text{bub}}. \quad (6.11d)$$

As in the simple model above, all axial lengths entering into the expression for circuit elements are assumed constant.

## 6.5 Comparison

### 6.5.1 First attempt

Using the measured pressure at the sensor as the input, the model is used to predict the motion of the bubble interfaces. The model results for the same four frequencies as fig. 6.5 are given in fig. 6.7.

The model predicts the correct dynamics. At 1 Hz the displacement amplitudes are identical with (almost) no phase-lag, while at 30 Hz the displacement of the trailing interface is larger than that of the leading interface and a phase-lag of roughly  $\pi/4$ . The phase-lag is close to the experimental results, but the amplitude difference is roughly a factor of 3/2 in the model while the experiments show a factor of 2. At 50 Hz the model predictions of almost  $\pi/2$  phase-lag and larger leading interface displacement of a factor of approximately 5/2 is in good agreement with the experiments, as is the prediction of much larger leading interface displacement at 100 Hz. However, the model prediction of numerical values of said displacements become increasingly worse as the frequency is increased: at

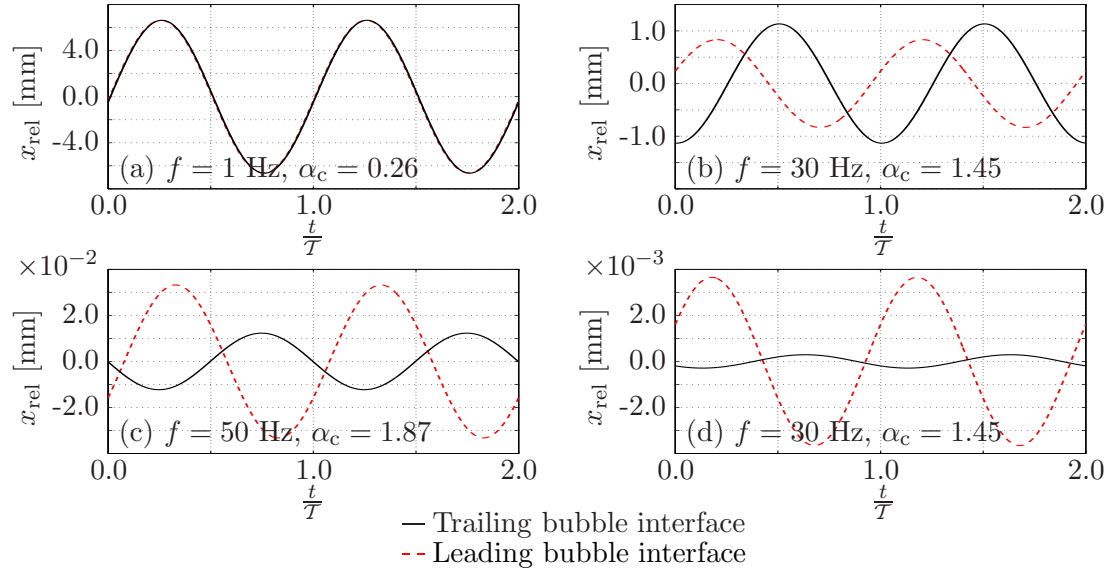


**Figure 6.7:** Modeled bubble displacements using  $C_{\text{sens}}$  estimated in sec. 5.4.3 ( $C_{\text{sens}} = 1.67 \times 10^{-15} \text{ m}^3 \text{ Pa}^{-1}$ ). Comparing to the experimental data of fig. 6.5 panels (b), (d), (f) and (g), the model is observed to capture the dynamics but its numerical values become increasingly worse as the frequency is increased.

100 Hz the experiments show a leading interface displacement amplitude of nearly 0.1 mm while the model predicts the same displacement amplitude to  $3.65 \times 10^{-3} \text{ mm}$ .

The slight undershooting of the displacement amplitudes at  $f = 1 \text{ Hz}$  by the model are a result of the constant axial lengths used in the circuit elements, as discussed in sec. 6.4.1 above. Whereas the model predicts displacements of about  $\pm 6.5 \text{ mm}$  the experimental results show these to be  $\pm 8.5 \text{ mm}$ . The discrepancy of the displacement amplitude ratio at 30 Hz cannot, however, be attributed to the constancy of the axial lengths, but is an artifact of the model.

The good qualitative agreement of the model and the experimental data suggest the correct model has been developed, but one or more of the circuit elements has an incorrect numerical value. Since the model predictions worsen with increasing frequency the culprit is a transient circuit element.

### 6.5.2 Correcting the model

The circuit element whose numerical value is most likely to be incorrect is the compliance of the sensor  $C_{\text{sens}}$ , since an air bubble easily could have been trapped inside the sensor during experimentation. If this was the case,  $C_{\text{sens}}$  would exceed the estimate in sec. 5.4.3, which in turn would mean that much of the flowrate entering the sensor would be used to compress the bubble. This would not be of consequence at low frequencies since the system at all times would be in quasi-equilibrium, but at higher frequencies at or above resonance, much of the flowrate would be absorbed in the bubble and the flowrates in the rest of the system would be correspondingly lower. This notion is backed by the good agreement of

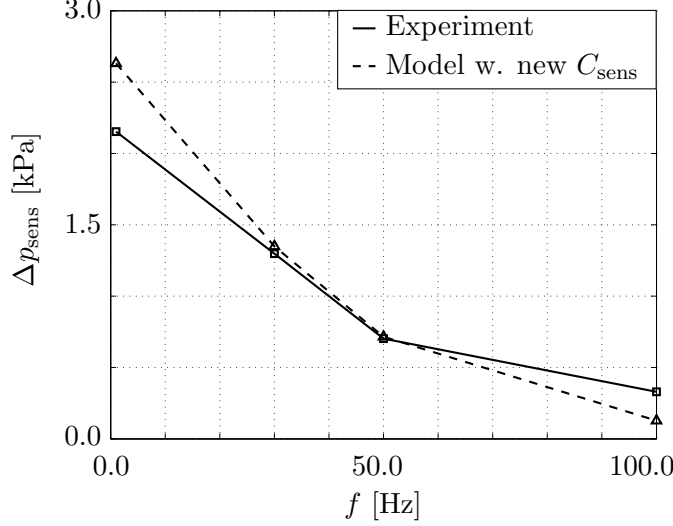


**Figure 6.8:** Sensor pressure computed from EC model using electrical current while letting  $C_{\text{sens}}$  be a fitting parameter. The best agreement (shown) is found for  $C_{\text{sens}} = 4.10 \times 10^{-14} \text{ m}^3 \text{ Pa}^{-1}$ , corresponding to the presence of a small air bubble of radius  $a = 0.98 \text{ mm}$ .

the experiment and model below resonance at 1 Hz ( $\alpha_c = 0.26$ ) where the system is in quasi-equilibrium and the observed increase in model deviation with increasing frequency. The correct numerical value of  $C_{\text{sens}}$  is determined from the EC model using the measured electrical coil current as input. The sensor pressure is computed and compared to the measured ditto, and  $C_{\text{sens}}$  is used as a fitting parameter. The best agreement for all four frequencies is found when  $C_{\text{sens}} = 4.10 \times 10^{-14} \text{ m}^3 \text{ Pa}^{-1}$  (instead of  $C_{\text{sens}} = 1.67 \times 10^{-15} \text{ m}^3 \text{ Pa}^{-1}$ ), as shown in fig. 6.8, while fig. 6.9 shows that the bubble interface displacements predicted by the EC model coincide with the experimental data for this choice of  $C_{\text{sens}}$ .

Assuming the estimated value of  $C_{\text{sens}} = 1.67 \times 10^{-15} \text{ m}^3 \text{ Pa}^{-1}$  to be correct, the additional compliance of  $3.94 \times 10^{-14} \text{ m}^3 \text{ Pa}^{-1}$  must be attributed to air. The volume of this amount of air is  $3.99 \times 10^{-9} \text{ m}^3$ , which is roughly twenty times lower than the estimated internal volume of the pressure sensor of  $1.0 \times 10^{-7} \text{ m}^3$ . This, coupled with the annoying ability of air bubbles to get stuck in microfluidic systems and the inherent sensor priming difficulties makes it very likely that an air bubble was trapped in the sensor during these experiments. Assuming the bubble to be spherical, its radius would be 0.98 mm, which could easily be have been stuck in the sensor.

The model and experiments now agree on both dynamics and numerical values through the whole probed frequency range. The model still undershoots at  $f = 1 \text{ Hz}$ , but this is to be expected as already discussed. Overall, the model predicts the leading interface displacement slightly better than the trailing interface, but becomes increasingly better in this regard as the frequency is increased, which is of course associated with a general trend of decreasing trailing interface displacement. The model predicts a non-zero trailing interface displacement at  $f = 100 \text{ Hz}$ , contrary to the experimental data. However,

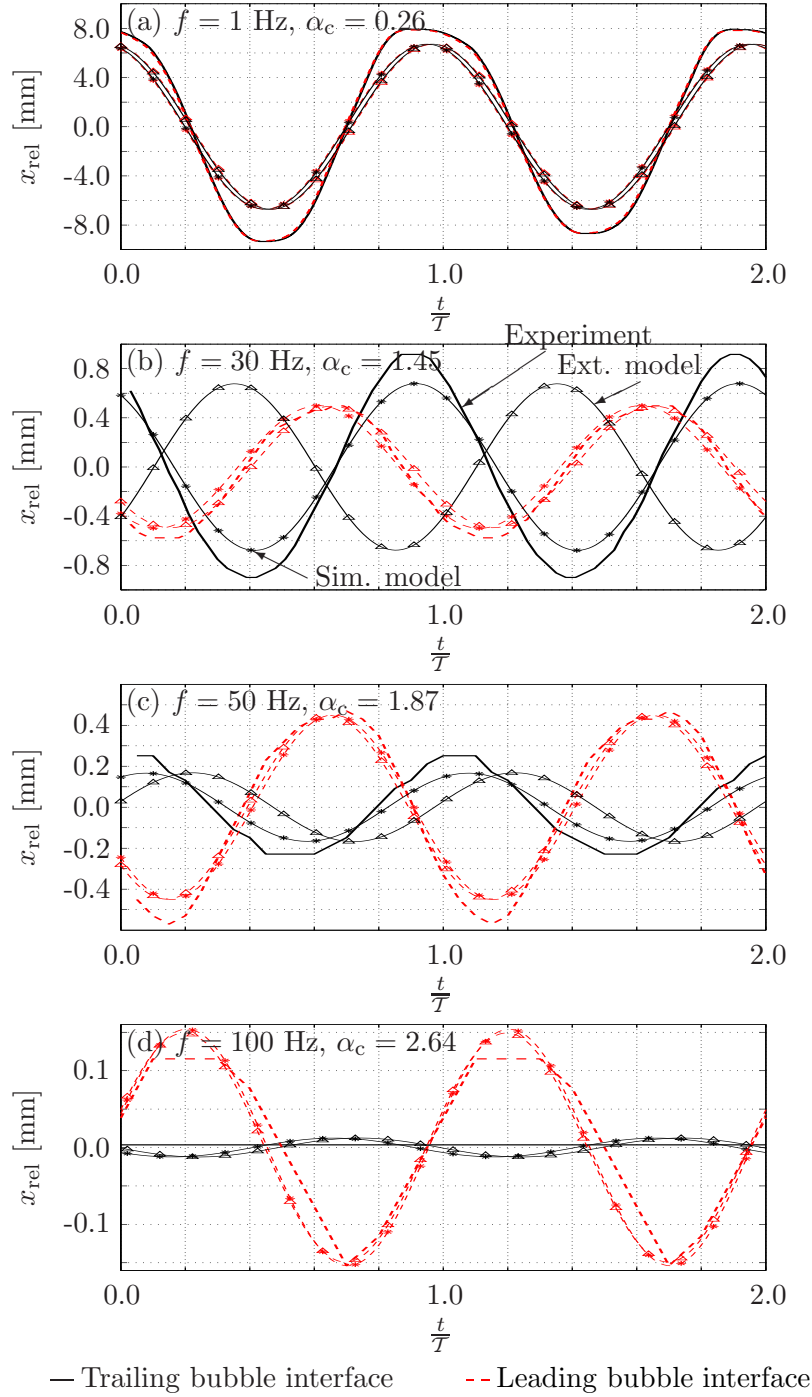


**Figure 6.9:** Modeled bubble displacements (simple model: starred thin lines, extended model: thin lines with triangles) with an added air bubble ( $C_{\text{sens}} = 4.10 \times 10^{-14} \text{ m}^3 \text{ Pa}^{-1}$ ) and experimental results (thick lines). Very good agreement is found between the models and the experiments through the entire frequency range, but the simple model predicts displacement amplitudes and phase-lags better. Both models capture the leading interface displacement slightly better than the displacement of the trailing interface.

the predicted displacement is below the resolution along the horizontal image axis of  $4.00 \times 10^{-2}$  mm pixel<sup>-1</sup>, so the results of the model are trustworthy. The results of the extended model based on the continuum limit of the EC equations are also given in fig. 6.9. This model still captures the dynamics, but its results are inferior to those of the simple model, which better captures both phase-lags and displacement amplitudes. The wave speed is related to the wave number through  $c = \omega/\text{Re}[k]$ , and a pressure wave traverses the tube from the pressure source chamber to the atmosphere in  $t = \ell/c$ . This time ranges from about 1.1 ms at 1 Hz to about  $5.0 \times 10^{-2}$  ms at 100 Hz, so the pressure waves can be neglected and the pressure is in quasi-equilibrium at all times. However, the continuum model should still reproduce the results of the simple model. The biggest deviation by far is found for the case at  $f = 30$  Hz close to the resonance frequency, and it is thought that it is related to the resonance, but the reasons for this disagreement have not been investigated further due to a lack of time.

In the experiments, a Young-Laplace pressure drop was present at the water-air interface at the outlet of the tube downstream of the imaged bubble, which was not included in the models. This pressure drop is estimated as

$$\Delta p_{\text{YP}} \approx \frac{72.9 \times 10^{-3} \text{ N m}^{-1}}{2 \times 0.254 \times 10^{-3} \text{ m}} \approx 1.44 \times 10^2 \text{ Pa}, \quad (6.12)$$

while the pressure amplitude at the bubble is the case of  $f = 100$  Hz is  $\Delta p_{\text{bub}} = 1.20 \times 10^3$  Pa, or approximately one order of magnitude greater. The Young-Laplace pressure has thus been excluded for simplicity, and the model still capture the observed physics.

## 6.6 Summary

Using the developed pressure source, a trapped air bubble was exposed to pulsatile conditions at the frequencies 1 Hz, 30 Hz, 50 Hz and 100 Hz. The motion was recorded via a digital photography setup, and the bubble interface motion was obtained from a simple image processing routine developed in MATLAB. An EC model was developed to describe the system which captured the dynamics but underpredicted the displacements of the bubble interfaces increasingly poor as the frequency — and thus the system's dependence on inertial effects — was increased. Using the measured electrical coil current as input, it was demonstrated that the experimentally observed behavior of the system was retrieved if a small air bubble had been trapped in the sensor. Considering the persistence of air bubbles trapped in microfluidic systems, the inherent priming difficulties of the sensor and the fact that changing this one parameter yielded agreement in the entire probed frequency range, the presence of such an air bubble is very likely. A more elaborate continuum model was also presented for the system, which did not yield better results than the simple model. The physics is thus well described by the simple low-order model, and there is no physical reason to use the mathematically more cumbersome extended model.



## Chapter 7

# Characterization of component dynamics

The presented EC models have so far proven effective in describing the behavior of the dynamic systems modeled, capturing both phase-shifts and amplitudes of the pressure and flowrate for the pulsatile case and correctly predicting the start-up of a fairly complex transient system. In this chapter, the predictive capabilities of the models will be used for the characterization of the dynamics of microfluidic components using only simple DC characteristics of the component as input. The method is applied to a commercially available duckbill valve for illustration, but may be applied to any passive yet time-dependent component.

### 7.1 Proposed method

The dynamic characteristics of some components may easily be deduced from theoretical considerations, e.g. the behavior in an elastic tube as discussed in chapter 3, since well-known solutions to the governing equations may be extended to accommodate the elastic walls. In other cases, however, the dynamics are not easily predicted from theoretical considerations, since complex interplay between solids and fluids inside the component is difficult to quantify and often extremely shape-dependent.

Due to the similarity to electric circuits, time-dependent microfluidic components exposed to pulsatile pressure will have inherent cutoff-frequencies<sup>1</sup>. Above this frequency the component never reaches steady state and very little flowrate, and consequently pressure, is transmitted downstream. As an example, consider a compliance exposed to a pulsatile pressure which oscillates so fast that the compliance never inflates to the level required by the pressure amplitude; in this case almost all incoming flowrate is absorbed in the compliance leaving very little to continue downstream. In the simplest exploitation of the electric circuit analogy, the compliance of a component can be deduced from the cutoff-frequency as described in [6], or alternatively from the decay time of an over pressure as

---

<sup>1</sup>The cutoff-frequency is usually defined as the frequency at which the transmitted amplitude is 90 % of the passband amplitude.

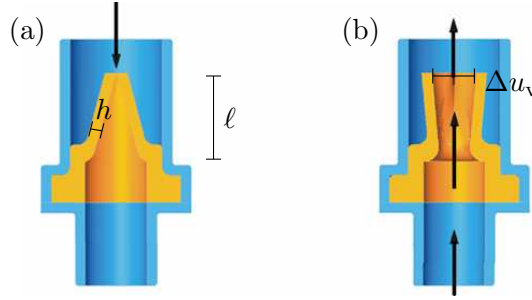


**Figure 7.1:** Duckbill valve with flow direction indicated by the arrows. Also shown are the dimensions for the EC model. (a) The valve is closed in the negative flow direction by design. (b) In the positive flow direction, the pressure difference across the valve opens it. Courtesy of Minivalve International, [61].

demonstrated for  $C_{\text{tent}}$  in chapter 5. However, the approach can be used to derive more complex dynamic characteristics, as long as an adequate EC model of these exists. An example of this was the use of the EC model to predict the presence of an air bubble in the pressure sensor during experimentation in the previous chapter. Only one free parameter, such as the compliance, is allowed if the method is to determine a unique value of the parameter.

The proposed method simply consists of applying a pulsatile pressure while measuring pressure up- and downstream of the component in question to locate the cutoff-frequency since this is a manifestation of the dynamic response of the component. The parameter value which fits the results of an EC model of the system to experimental data is then deduced from this, while taking the remaining parameters for this model from theoretical considerations or DC experiments. The approach applies to all passive components exhibiting temporal dependence e.g. elastic tubes, valves, nozzles, etc., and will be applied to a passive valve in the following for illustration.

## 7.2 An introduction to microvalves

A valve allows fluid to flow in one direction and impedes flow in the opposite direction. Valves that stop backward flow are known as check valves or rectifying valves, and valves for microfluidics are known as microvalves. A short introduction to microvalves is given below while more thorough introductions may be found in [61, 62].

A valve opens when a pressure difference exists in its positive direction as shown in fig. 7.1(b), and it is imperative that it closes when no or a negative pressure difference is applied. Due to the small inertial forces of microfluidics, fluid cannot be counted on to close the valve in backflow so the valves are closed by design when no pressure difference is applied. Valve opening is realized in positive flow by elastic deformation, which depends on the applied pressure difference, so a non-zero pressure difference  $\Delta p_{\text{open}}$  is required to open the valve. Moreover, a characteristic opening volume of fluid  $\mathcal{V}_{\text{open}}$  must pass into the valve before it opens, which may be thought of as a compliance in the EC framework, henceforth denoted  $C_{\text{hyd}}^{\text{valve}}$ .

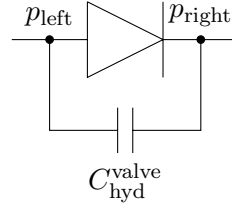


**Figure 7.2:** EC model of generic elastomeric valve. A compliance is coupled in parallel to the diode, since a characteristic volume of fluid must enter, before the valve opens. Flow enters from the left and leaves to the right.  $p_{\text{left}}$  and  $p_{\text{right}}$  will be used in this chapter to denote the pressure just up- and downstream of the valve as shown here.

The valves used in this work are of the duckbill type (DU 027.001 made of silicone rubber by Minivalve International, Oldenzaal, The Netherlands), named for the resemblance of the closed valve to the bill of the duck, see fig. 7.1(a).

### 7.2.1 EC model

Valves are the microfluidic equivalent of a diode: a circuit element that only allows flow in one direction. However, the elastomeric duckbill valve does not behave as an ideal diode since a certain volume of liquid must be supplied before it opens, so the valve is modeled as an ideal diode and a capacitor in parallel, see fig. 7.2. This model is due to industrial supervisor Laurits Højgaard Olesen.

If opened, the valve is modeled as a rectangular slit<sup>2</sup>, which is justifiable since the length to width ratio of the valve is small and inertial effects are negligible. The hydraulic resistance of the valve is then given by, [1]

$$R_{\text{valve}} = \frac{12\eta\ell}{1 - 0.63\frac{\Delta u_v}{w}} \frac{1}{\Delta u_v^3 w}, \quad (7.1)$$

where  $\Delta u_v$  and  $w$  are the opening height and width of the slit, respectively, with  $w \gg \Delta u_v$  and  $\ell$  is the length of the valve in the flow direction, i.e. the length of the bill, see fig. 7.1. The opening height of the valve depends on the flowrate passing through it, which in turn depends on the pressure difference across the valve  $\Delta p$ , so it is a good assumption that  $\Delta u_v = \Delta u_v(\Delta p)$ . Said pressure difference must exceed  $\Delta p_{\text{open}}$  (otherwise the resistance is infinite), so it is posited that

$$\Delta u_v(\Delta p) = \max\{0, \kappa(\Delta p - \Delta p_{\text{open}})\}, \quad (7.2)$$

which will ensure an infinite resistance when the pressure difference does not exceed  $\Delta p_{\text{open}}$ . The constant  $\kappa$  is an elastic parameter of unit  $\text{m Pa}^{-1}$  measuring the valve opening per unit pressure difference, and is the valve parameter to be deduced from the dynamic response. The value of  $\kappa$  may be estimated by considering the valve as consisting

<sup>2</sup>The shape of the valve orifice depends on the pressure difference across it, but is almost rectangular when the slit height  $\Delta u_v$  is small.

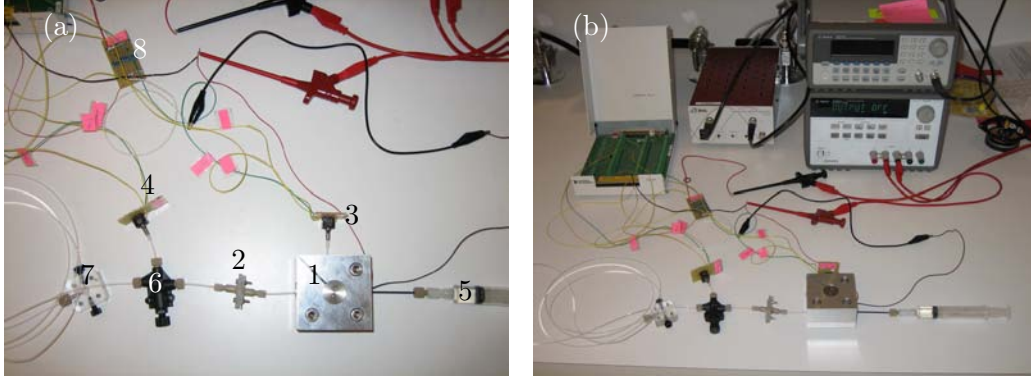


**Figure 7.3:** Experimental setup for pulsatile valve tests. (a) Close-up of the fluidic system seen from above. (b) The full setup with electronics. **Legend** (1): Pressure source, (2): Valve holder, (3): Upstream pressure sensor, (4): Downstream pressure sensor, (5): Syringe, (6): T-junction, (7): Outlet chamber and (8): Electrical resistance.

of two elastic beams, one for each part of the bill. Although very crude, this is expected to capture the basics of dynamics. The deflection of a simple linear beam of rectangular cross section  $h \times w$ , axial length  $\ell$  and Young's Modulus  $E$  exposed to a pressure difference is given by Tvergaard in [63], and since two beams deflect in the case of the valve,  $\kappa$  is estimated to

$$\kappa = 3 \left( \frac{\ell}{h} \right)^3 \frac{\ell}{E}. \quad (7.3)$$

The valve dimensions are estimated to  $\ell \approx 4 \text{ mm}$  and  $h = 0.5 \text{ mm}$ , where this latter is the manufacturer specified thickness of the bill. Using these values one finds  $\kappa = 7.49 \times 10^{-7} \text{ m Pa}^{-1}$ .

## 7.3 Experimental method and setup

### 7.3.1 Method

To experimentally detect its dynamic response, the valve is exposed to a pulsatile pressure and flowrate, while measuring the pressure up- and downstream of it. The experiment is conducted at different frequencies spanning two orders of magnitude. Appropriate component characteristics are determined from simple DC experiments (detailed below), which for a duckbill valve are compliance and the opening pressure. Data acquisition was carried similarly to the pressure measurements of the previous chapter.

### 7.3.2 Setup for pulsatile experiments

The setup is much akin to that of the previous chapter, only now the pressure is measured downstream of the valve in addition to the pressure reading at the chamber. A 15 psi pressure sensor is connected to one of the pressure source chamber exits (its pressure denoted  $p_{\text{sens1}}$ ) through a teflon tube ( $\ell_{\text{sens1}} = 4.1 \text{ cm}$ ,  $a_{\text{sens1}} = 0.125 \text{ mm}$ ,  $h_{\text{sens1}} = 0.669$

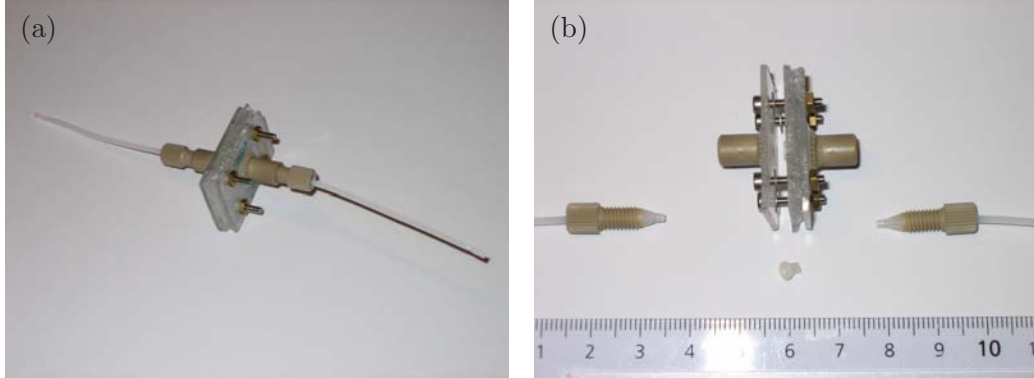


**Figure 7.4:** Duckbill valve holder. (a) The assembled holder with tubing. (b) The individual holder parts with a centimeter ruler. A valve is placed below the holder.

mm) and a syringe filled with Milli-Q water is connected to the chamber exits using a PEEK tube ( $\ell_{\text{sy}} = 9.4$  cm,  $a_{\text{sy}} = 6.25 \times 10^{-2}$  mm,  $h_{\text{sy}} = 0.731$  mm); a small air bubble of radius  $a \approx 0.5$  mm was observed in the syringe. The component of interest — in this case a valve fastened in a holder to be detailed below — is connected to the last chamber exit via a teflon tube ( $\ell_{\text{up}} = 6.1$  cm,  $a_{\text{up}} = 0.125$  mm,  $h_{\text{up}} = 0.669$  mm), downstream of which the tube branches into two via a T-junction: one for measuring the pressure  $p_{\text{sens2}}$  downstream of the valve (teflon tube of  $\ell_{\text{down}} = 6.3$  cm,  $a_{\text{down}} = 0.125$  mm and  $h_{\text{down}} = 0.669$  mm) and another exiting into atmospheric conditions via yet another piece of teflon tubing of length  $\ell_{\text{exit}} = 2.1$  m, radius  $a_{\text{exit}} = 0.254$  mm and wall thickness  $h_{\text{exit}} = 0.540$  mm. Pictures of the setup are given in fig. (7.3).

### 7.3.3 Valve holder

The valve was mounted in a holder fabricated of layered polymer sheets. Three layers of polycarbonate of roughly 2 mm thickness are glued together, with the valve fixed between the stack and an additional sheet. The stack and extra sheet were held together by four screws and the valve was placed in a throughhole of radius 1.0 mm which is wide enough that the valve could open fully yet narrow enough that it was not swept downstream. The resistance, hydraulic inductance and compliance of the holder have been neglected since polycarbonate is stiff ( $E \approx 30$  GPa according to [28]) and the throughhole radius exceeds the tubing radius of roughly one order of magnitude. The holder is shown in fig. 7.4.

### 7.3.4 Steady state experiments leading to valve characteristics

#### Opening pressure

Using the pressure source to generate a DC pressure difference and the same setup as described above, the pressure is measured from the source chamber exit and downstream of the valve at the T-junction. The pressure in the source is ramped up to about 10 kPa before ramping down to zero again, all in a time interval of roughly 30 s. With the pressure

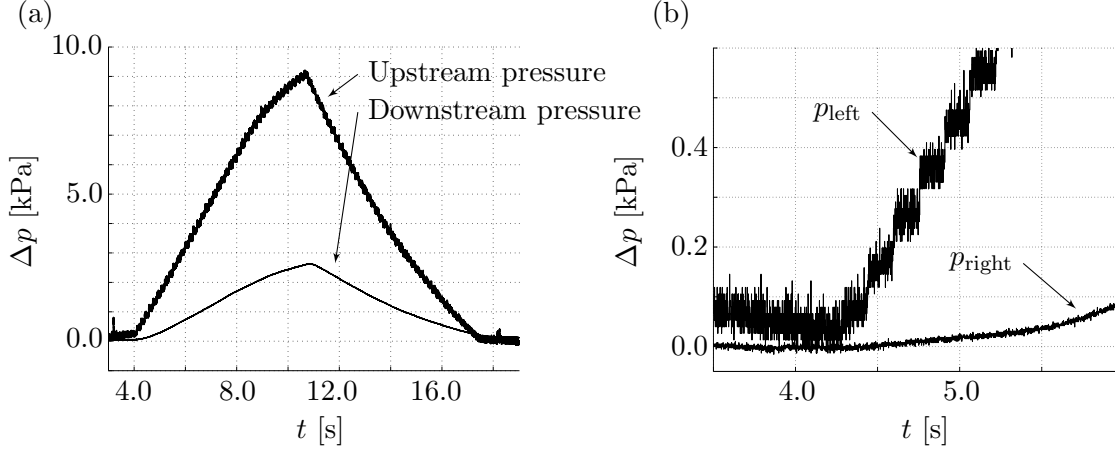


**Figure 7.5:** Typical measurement of opening pressure. (a) The ramping segment of the experiment with the pressures measured at the sensors. (b) Close-up showing the first few seconds after the pressure ramp-up has begun, with pressures now given at the valve. The first downstream pressure measurement is at  $t = 4.5$  s signifying the opening of the valve with  $\Delta p_{\text{open}} \approx 250$  Pa.

measured on both sides of the valve, the pressure at the valve is found from the EC model using the estimated value of  $\kappa$  from eq. (7.3) and the opening pressure can be determined. A typical measurement is given in fig. 7.5, which shows that the opening pressure is  $\Delta p_{\text{open}} \approx 250$  Pa, a value that agrees with the manufacturer specified  $\Delta p_{\text{open}} < 500$  Pa.

### Compliance

$C_{\text{hyd}}^{\text{valve}}$  is estimated by noting the volume of water stored in the valve at a given applied pressure difference as indicated by the motion of an air bubble in the valve tubing, which is the same method as already discussed for the estimates of the compliance of the pressure sensors, see sec. 5.4.3. Since the valves open when the pressure difference surpasses  $\Delta p_{\text{open}}$ , hydrostatic pressures were used in the estimates as they allow for better resolution than a manually operated syringe, and care was taken in not exceeding the opening pressure. In backflow, the valve will act as a compliant element even though no flow passes through, and consequently, negative compliance, i.e. compliance when a under-pressure is applied, is also estimated. The results are given in fig. 7.6.

Due to the blocking of the flow, a non-symmetric behavior of  $C_{\text{hyd}}^{\text{valve}}$  about the origin is expected, and the backflow compliance is found to noticeably exceed the compliance in the positive flow direction, so more liquid is stored in the valve at a given negative pressure difference, when it cannot open. Assuming a linear compliance is justified as long as one considers only the positive or negative flow direction. The numerical value of this compliance is then

$$C_{\text{hyd}}^{\text{valve}} = \begin{cases} 1.21 \times 10^{-13} \text{ m}^3 \text{ Pa}^{-1} & \text{for } \Delta p > 0 \\ 9.01 \times 10^{-13} \text{ m}^3 \text{ Pa}^{-1} & \text{for } \Delta p < 0. \end{cases} \quad (7.4)$$

Given the found value of  $\Delta p_{\text{open}} \approx 250$  Pa, it is surprising to find the pressure differences of  $\Delta p \approx 1.2$  kPa reached in the compliance experiments without detecting an opening

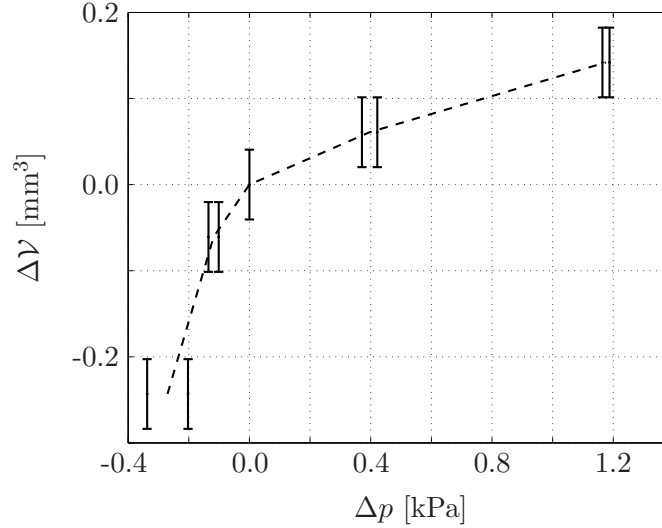


**Figure 7.6:**  $\Delta p - \Delta V$  results for the duckbill valve; as usual, the compliance is the slope of the curve. A non-symmetric compliance is found with backflow compliance exceeding  $C_{\text{hyd}}^{\text{valve}}$  in the positive flow direction.

of the valve. Although care was taken, the valve might have opened slightly during the experiments, which in turn would require additional experimental determination of  $C_{\text{hyd}}^{\text{valve}}$  for  $0 \leq \Delta p \leq \Delta p_{\text{open}}$ . However, the manufacturer sets the opening pressure for the first use to  $\Delta p_{\text{open}} \leq 5$  kPa, so the results might reflect this effect. The experiment was not redone, and the values of eq. (7.4) will be used in the following.

## 7.4 EC model

The pressure source was driven with pulsatile electric current, but the flow in the system is not entirely pulsatile since the valve transmits positive pressures (as long as the pressure drop across it exceeds its opening pressure), but blocks negative pressures. However, it is assumed that the pressure source delivers pulsatile pressures to the sensor and syringe connected to the chamber, while the rest of the system is exposed to transient phenomena rather than pulsatile. Thus, this sensor and syringe connected to the pressure source chamber are modeled just as in the bubble experiments of the previous chapter using simple AC fluidic elements, while the rest of the system is modeled with the regular DC elements. An inductor for the inertia of the water in the downstream sensor (sensor 2) is included similarly to the sensor at the chamber. The tubing from the chamber to the valve and from the valve and to the T-junction are both about 5 cm long and made of thick-walled teflon, so their compliances are nominal, and it makes little physical difference if the compliance of the entire wall is placed downstream of the resistance and inductance, rather than in the middle as previously done. Since the former is mathematically more convenient, this approach has been used for these two tube segments. A Womersley-type

**Table 7.1:** Circuit elements for characterization of valve dynamic response in SI units ( $[Z_{\text{hyd}}] = \text{Pa s m}^{-3}$ ,  $[R_{\text{hyd}}] = \text{Pa s m}^{-3}$ ,  $[L_{\text{hyd}}] = \text{Pa s}^2 \text{ m}^{-3}$ ,  $[C_{\text{hyd}}] = \text{m}^3 \text{ Pa}^{-1}$ ).

Element	Value	Element	Value	Element	Value
$Z_{\text{Wom}}^{\text{sens1}}$	$2.14 \times 10^{11} + i 3.49 \times 10^9$	$R_{\text{sens2}}$	$3.66 \times 10^{11}$	$C_{\text{wall}}^{\text{syr}}$	$8.97 \times 10^{-19}$
$L_{\text{sens1}}$	$6.35 \times 10^5$	$L_{\text{tube}}^{\text{sens2}}$	$7.12 \times 10^8$	$C_{\text{wall}}^{\text{up}}$	$1.78 \times 10^{-17}$
$Z_{\text{Wom}}^{\text{syr}}$	$7.84 \times 10^{12} + i 3.20 \times 10^{10}$	$L_{\text{sens2}}$	$6.35 \times 10^5$	$C_{\text{wall}}^{\text{down}}$	$1.84 \times 10^{-17}$
$R_{\text{Wom}}^{\text{up}}$	$6.38 \times 10^{11}$	$R_{\text{exit}}$	$6.44 \times 10^{11}$	$C_{\text{wall}}^{\text{exit}}$	$2.58 \times 10^{-15}$
$L_{\text{up}}$	$1.24 \times 10^9$	$L_{\text{exit}}$	$5.17 \times 10^{11}$	$C_{\text{air}}$	$4.14 \times 10^{-14}$
$R_{\text{down}}$	$6.58 \times 10^{11}$	$C_{\text{wall}}^{\text{sens1}}$	$1.20 \times 10^{-17}$	$C_{\text{syr}}$	$2.51 \times 10^{-13}$
$L_{\text{down}}$	$1.28 \times 10^9$	$C_{\text{wall}}^{\text{sens2}}$	$1.02 \times 10^{-17}$		

resistance of sec. 2.5.1 is used for the tube segment from the chamber to the valve, as the flow here is assumed to be almost pulsatile and the valve compliance is given by eq. (7.4) and thus changes value when the pressure difference changes sign. The EC model for the whole system is presented in fig. 7.7. The continuum model has not been included in the modeling of these experiments, as it has not proven superior to the simple EC models in the cases previously studied.

The system has several inherent time scales due to the many circuit elements, whose values are listed in table 7.1 for  $f = 1 \text{ Hz}$  actuation. The resulting ODEs must be solved numerically to capture the valve dynamics, so the presence of these different time scales renders the problem stiff<sup>3</sup>. The model is solved using MATLAB's `ode15s` ODE solver, which handles stiff problems, but to speed up the solution time, the compliances of the tube from the chamber to the valve and from the T-junction to the downstream sensor have been left out; the  $RC$  times for these tube segments are of  $\mathcal{O}(10^{-6} \text{ s})$  while the valve dynamics were studied for  $f \leq 30 \text{ Hz}$ , so these omissions are justified.

## 7.5 Comparison

The level of agreement between experimental data and model results are somewhat poor for this characterization of component dynamics. As already shown in the previous chapter, elimination of air bubbles in the pressure sensors is very difficult, which in turn means that there are three fitting parameters,  $C_{\text{sens1}}$ ,  $C_{\text{sens2}}$  and  $\kappa$ , all to be determined from one experiment. At best, one is left with a non-unique solution, but arriving at this solution requires much trial-and-error tuning of the parameters. Secondly, the order of magnitude of the sensor compliances required to somewhat recreate the experimental data turned out to be so large that these thoroughly dominate the system, with only nominal effects of changes of  $\kappa$ , the one parameter describing the valve, whose value was hoped to be

<sup>3</sup>A stiff problem contains several time scales, and the numerical method employed to solve the problem must resolve the finest of these scales. If the problem has a very fast inherent time scale — several orders faster than the time scale of the studied dynamics — the solver must take many more time steps, which is very time consuming but does not yield additional insight to the studied dynamics, [64].



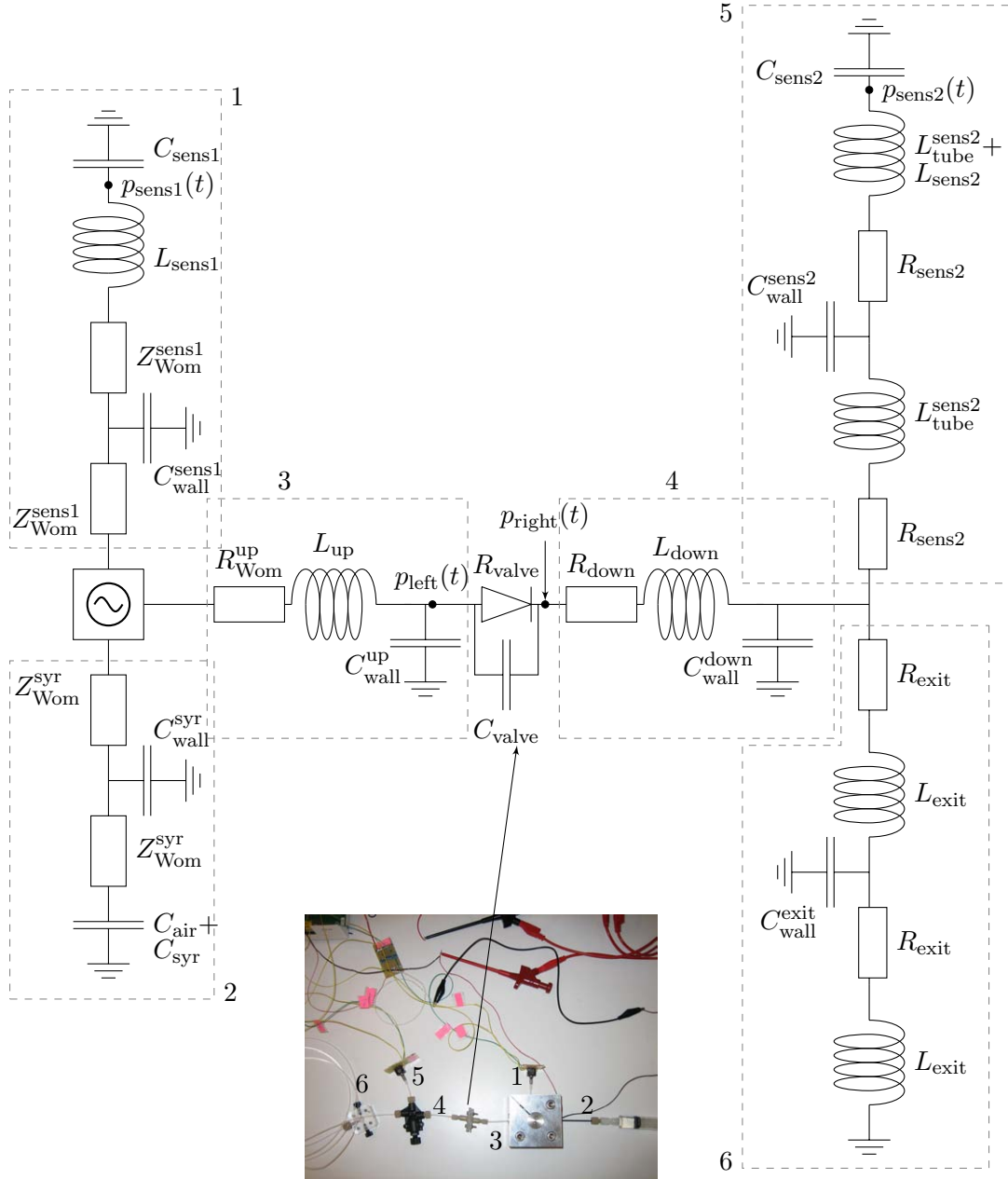


**Figure 7.7:** EC model of pulsatile setup for component dynamics characterization. The elastic walls are modeled as usual, except for tubing connecting the chamber to the valve and from the valve to the T-junction, where the compliance has been placed downstream of the inductance and resistance for mathematical simplicity. Since the thick-walled teflon is only a little compliant, this does not introduce much error.  $L_{\text{sens2}}$  is the inertia of the liquid inside sensor 2, not to be confused with  $L_{\text{tube}}^{\text{sens2}}$  which is the inertia of the water in the tubing, connecting sensor 2 and the T-junction. Due to the mathematical properties of the governing equations,  $L_{\text{sens2}}$  and  $L_{\text{tube}}^{\text{sens2}}$  are superposed and therefore represented by only one symbol, as are  $C_{\text{air}}$  and  $C_{\text{syr}}$ . **Legend** (1): Pressure sensor 1 and tubing, (2): syringe and tubing, (3): tube connecting pressure source and valve holder, (4): tube from holder to T-junction, (5): pressure sensor 2 and tubing, (6): tube exiting to atmospheric conditions.

deduced from the model. The observed valve dynamics is found to be in accordance with the experimental data, but the pressure amplitudes are poorly captured.

### 7.5.1 Valve dynamics

Using the pressure recorded by the sensor connected to the chamber as input, the pressure at the downstream sensor is computed from the model with two examples given in fig. 7.8. The figure displays the best coincidence of the model and the experimental data, which is found at  $C_{\text{sens1}} = 1.67 \times 10^{-15} \text{ m}^3 \text{ Pa}^{-1}$ ,  $C_{\text{sens2}} = 8.0 \times 10^{-13} \text{ m}^3 \text{ Pa}^{-1}$  and  $\kappa = 7.49 \times 10^{-7} \text{ m Pa}^{-1}$ , corresponding to the presence of a air bubble of  $\mathcal{V} = 8.05 \times 10^{-8} \text{ m}^3$  in sensor 2 which is roughly the entire internal volume of this sensor. As the figure clearly shows, the model poorly predicts the pressure level.

The experimental data and model both display the same dynamics: the valve opens as the pressure difference across it exceeds the opening pressure and pressure is transmitted from the valve to the downstream sensor. The valve closes again once  $\Delta p < \Delta p_{\text{open}}$  letting no flow through, but since  $p_{\text{left}}$  continues to decay because of the pulsatility, a negative pressure difference arises across the valve. A volume is stored in the valve due to this pressure difference as a consequence of the compliant nature of the valve, causing a small negative flowrate downstream of the valve, even though it is closed. Since the pressure outside the system is atmospheric, this negative flowrate requires a pressure drop to occur downstream of the valve. The amplitude of this negative pressure is smaller than the positive pressure amplitude which arises, when the valve opens. The negative pressure is observable in figs. 7.8(a) and (c).

A small knee is observed in both measurement and model results as the valve pressure difference  $\Delta p = p_{\text{left}} - p_{\text{right}}$  reaches zero when increasing from maximum negative pressure, most obvious in fig. 7.8(b). At this point when  $p_{\text{left}} = p_{\text{right}}$ , the compliance of the valve decreases with almost one order of magnitude as stipulated by eq. (7.4) which means that the valve suddenly can store a much smaller volume of fluid at the same pressure difference. The incoming flowrate from the chamber is unaffected by this sudden change in valve compliance, so the pressure drop across the valve is increased according to  $\Delta p = \Delta \mathcal{V} / C_{\text{hyd}}^{\text{valve}}$  to accommodate the volume of fluid no longer stored in the valve compliance. Since  $p_{\text{left}}$  is given by the chamber pressure<sup>4</sup>, this increase of  $\Delta p$  forces a rapid decrease of  $p_{\text{right}}$ , which continues until  $\Delta p > \Delta p_{\text{open}}$  where the valve opens and pressure again begins to increase downstream of it.  $p_{\text{sens2}}$  obviously depends on  $p_{\text{right}}$ , so the presence of such a knee in  $p_{\text{right}}$  will also show up in  $p_{\text{sens2}}$ . The reverse effect is observed when the valve closes, although to a much lesser extend. The model results for 1 Hz actuation (panels (c) and (d)) display the same sharp increase for  $p_{\text{left}}$  and  $p_{\text{right}}$  although after the apex of the pulsatility, but no knee is observed in  $p_{\text{sens2}}$ .

Although the predictions of the model are fair in terms of dynamics, the deviations in numerical value are roughly a factor of 1 to 2 throughout the probed frequency range of 0.1-30 Hz.

---

<sup>4</sup> $p_{\text{left}}$ , of course, also depends on the system downstream of the valve, but it is found that this dependence is weaker than the dependence on the chamber pressure.

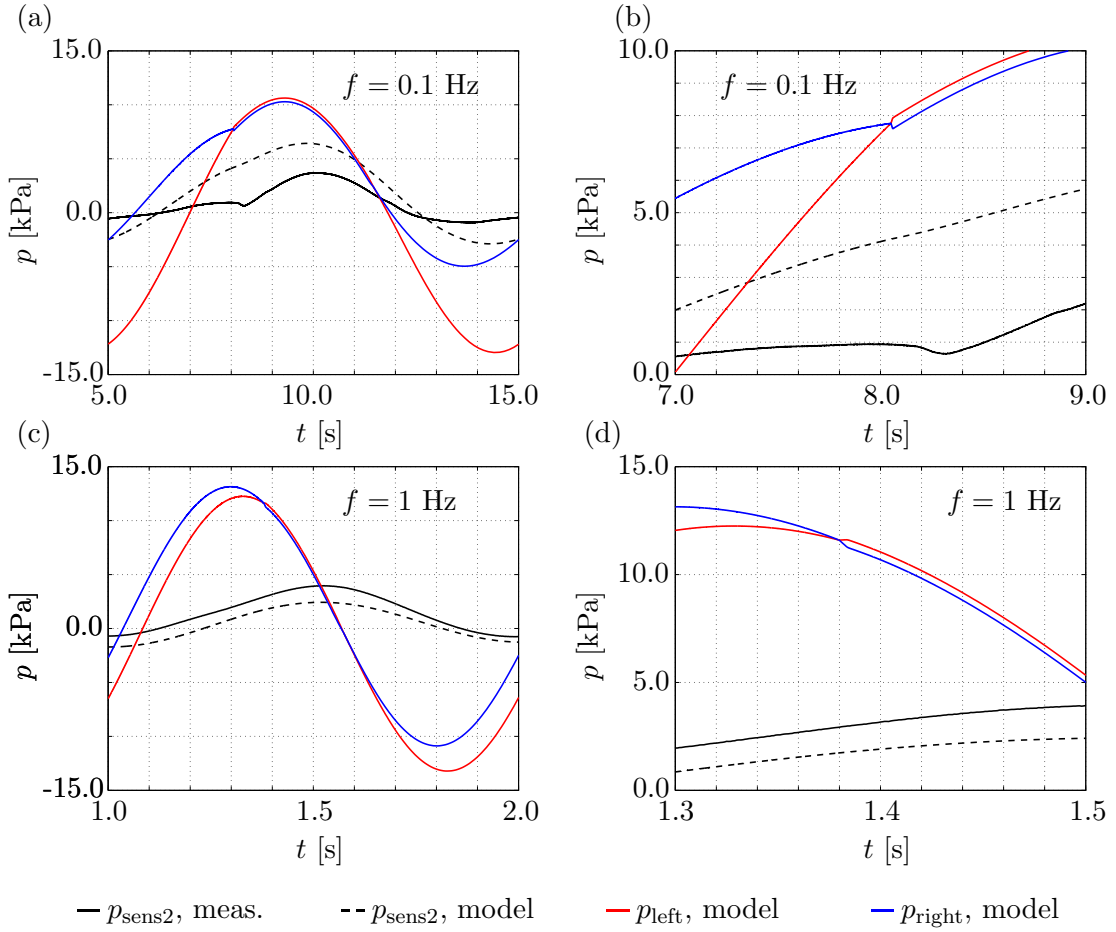


**Figure 7.8:** Measured (solid black) and predicted (dashed black) pressure at downstream sensor during one period, along with the pressure just around the valve as predicted by the model ( $p_{\text{right}}$  is blue while  $p_{\text{left}}$  is red). The compliances of the system are  $C_{\text{sens1}} = 1.67 \times 10^{-15} \text{ m}^3 \text{ Pa}^{-1}$  and  $C_{\text{sens2}} = 8.0 \times 10^{-13} \text{ m}^3 \text{ Pa}^{-1}$  with  $\kappa = 7.49 \times 10^{-7} \text{ m Pa}^{-1}$ . (a) At 0.1 Hz actuation showing a full period. (b) Zoom in (a) showing the jump in pressure in both measurements and model data as the valve opens. (c) 1 Hz actuation shows no sign of knee in neither modeled nor measured pressure  $p_{\text{sens2}}$ . (d) A small knee is observed when zooming in even for 1 Hz actuation, although only in the model results.

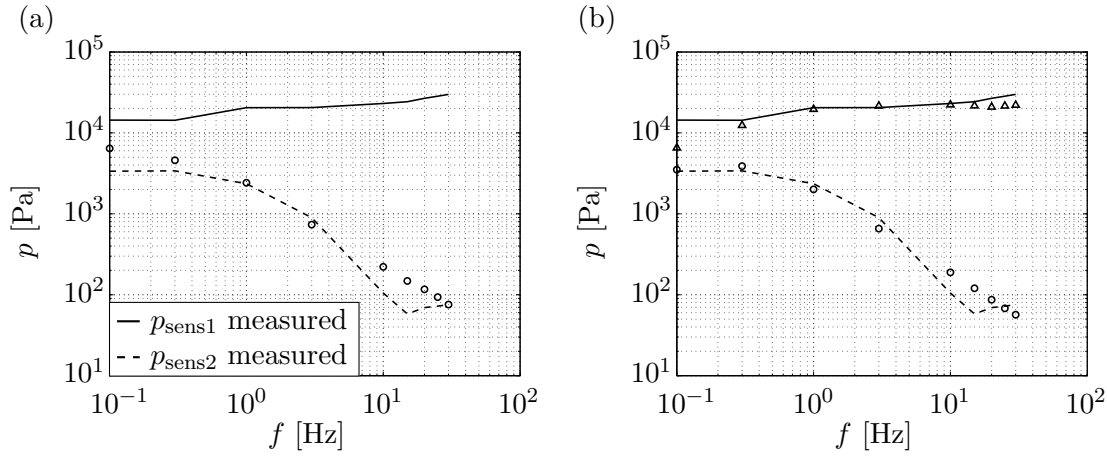


**Figure 7.9:** Maximum sensor pressure as a function of frequency, where as usual  $p_{\text{sens1}}$  and  $p_{\text{sens2}}$  are the pressures in the up- and downstream sensors, respectively. The compliances are  $C_{\text{sens1}} = 1.67 \times 10^{-15} \text{ m}^3 \text{ Pa}^{-1}$  and  $C_{\text{sens2}} = 8.0 \times 10^{-13} \text{ m}^3 \text{ Pa}^{-1}$ , i.e. the same value of  $C_{\text{sens2}}$  as in fig. 7.8. (a) Using the measured pressure in sensor 1 as input, the pressure in the downstream sensor is computed from the EC model (circles). The two agree reasonably well except at  $f = 0.1 \text{ Hz}$  and  $f = 20 \text{ Hz}$ . (b) With the actuator coil electrical current as input, the pressure at both sensors are computed from the EC model; triangles are  $p_{\text{sens1}}$  and circles  $p_{\text{sens2}}$ . The model is found to also reproduce the pressure using the current as input.

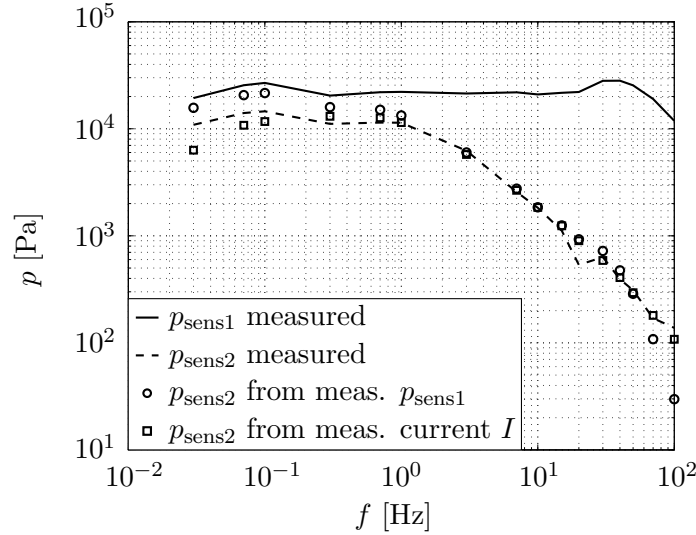
### 7.5.2 Frequency dependence

Fig. 7.9 shows the maximum value of the downstream pressure computed from the chamber pressure for  $C_{\text{sens1}} = 1.67 \times 10^{-15} \text{ m}^3 \text{ Pa}^{-1}$ ,  $C_{\text{sens2}} = 8.0 \times 10^{-13} \text{ m}^3 \text{ Pa}^{-1}$  and  $\kappa = 7.49 \times 10^{-7} \text{ m Pa}^{-1}$ , the same sensor compliances and  $\kappa$  as in the previous section. Using the measured actuator coil electrical current, the idea was to use the elastic parameter  $\kappa$  to fit the pressures at the sensors to the measured values. This has not been possible, however, as no value of  $\kappa$  has been found which applies in the entire frequency range 0.1-30 Hz. Moreover, the sensor compliances required for the model to reproduce the experimental data makes  $\kappa$  insignificant, as long as  $\kappa \leq 0.1 \text{ m Pa}^{-1}$ , while at and above this value, the model results deviate by several orders of magnitude. Thus, the one parameter hoped to be determined by the experiment has been voided.

The overall behavior of the experimental data is recreated from the model with the same values of sensor compliances and  $\kappa$ , using either the actuator electric current or the measured pressure at the sensor by the chamber as input. The distinct kink in the measurements of  $p_{\text{sens2}}$  at  $f = 20 \text{ Hz}$  is not reproduced by the model, and noticeable deviations between the two approaches are found at the lowest frequencies, when the system is quasi-static. This, along with the insignificance of  $\kappa$ , suggests a flaw in the EC model.

### 7.5.3 Validation of method

Due to the previous success with EC modeling of pulsatile flow, a frequency sweep of the system without a valve has been conducted, and the system modeled using Womersley-



**Figure 7.10:** Frequency sweep of system without valve. The pressure at sensor may be found from the model using either electric coil current  $I$  or pressure at sensor 1 as input, if the compliances of these sensors are  $C_{\text{sens1}} = 1.67 \times 10^{-15} \text{ m}^3 \text{ Pa}^{-1}$  and  $C_{\text{sens2}} = 1.7 \times 10^{-13} \text{ m}^3 \text{ Pa}^{-1}$ .

type impedances with the regular method for modeling the elastic tubes throughout. Using either the coil electric current or the measured pressure in the upstream sensor as input, the pressures at the downstream sensor was fairly well captured for  $f > 0.3 \text{ Hz}$  if no bubble was present in the sensor by the chamber ( $C_{\text{sens1}} = 1.67 \times 10^{-15} \text{ m}^3 \text{ Pa}^{-1}$ ) and a spherical bubble of radius 1.6 mm was present in the sensor at the T-junction ( $C_{\text{sens1}} = 1.7 \times 10^{-13} \text{ m}^3 \text{ Pa}^{-1}$ ), see fig. 7.10. In addition to the already observed disagreement at low frequencies, the kink at 20 Hz is also found from these measurements, and is thus thought to be a feature of the setup and not just a false measurement. The reason for this has not been studied.

The overall agreement between EC model and experimental data in the absence of valves, using either electric current or pressure as input, suggests that this model is correct, and that the discrepancies observed when the valve is included arise due to an insufficient EC model of the valve or flawed values of  $C_{\text{hyd}}^{\text{valve}}$  or  $\Delta p_{\text{open}}$ . As already discussed, the found value of  $C_{\text{hyd}}^{\text{valve}}$  is doubtful. However, the presented EC model for the valve is observed to recreate the dynamics found from the measurements, suggesting that at least the basics of the model are correct. Moreover, since the model results for the whole system deviate the most in the quasi-static limit of  $f < 0.3 \text{ Hz}$ , and such deviations are found even when no valves are present in the system, it is thought that these deviations are features of the system rather than the valve model, possibly caused by non-linearities in the behavior of the pressure source. Furthermore, nothing has been found which suggests the proposed method of using the predictions of an AC EC model to infer component characteristics from experiments is not valid, only that the developed experimental setup is not ideal due to seemingly constant presence of air bubbles in the sensors.

## 7.6 Summary

A method has been presented for deducing the dynamic characteristics of a time-dependent microfluidic component based on the analogies making up EC theory. Exposing the component to pulsatile pressure and flowrate at different frequencies, the dynamic response of the component in conjecture with an AC EC model can be used to determine the time-dependent parameter of the component. The method was applied to a soft elastomeric duckbill valve, and although a cutoff-frequency was indeed discovered, the EC model was unable to consistently reproduce experimental data. Given the proof of the modeling technique presented in the previous chapters and the good accordance found for certain parameter values in the present case in the absence of the valve, it is believed the discrepancies are caused by an insufficient model of the valve. This, however, has not been studied due to a lack of time.

## Chapter 8

# Conclusion and outlook

### 8.1 Conclusion

This thesis has extended and demonstrated the applicability of a lumped-parameter modeling technique known as equivalent circuit (EC) modeling to inertially dominated microfluidics, while also developing an experimental setup to deliver a pulsatile pressure difference into the low kilohertz range. This setup was used to study the motion of an air bubble exposed to pulsatile pressure and flow, and it was used in an attempt to derive the dynamic response of a commercially available duckbill valve.

Having introduced the simple method, it was showed that pulsatile flow may also be included in the method. A corrected dimensionless parameter  $\alpha_c$  was derived whose value determines the relative importance of inertia and resistance in the flow: resistance dominates for  $\alpha_c < 1$  while inertia prevails for  $\alpha_c > 1$ . Moreover, a frequency dependence of the resistance unlike regular steady state pressure driven flow was found and quantified. All tubing used in experimental microfluidics are compliant due to their elasticity, so the time-dependent (pulsatile or transient) pressure driven fluid flow in elastic tubes has several inherent time scales, and the quantification of these time scales is imperative if one is to fully understand and correctly model the system. To this end, an expression for the compliance of an elastic wall has been derived along with the compliance of an air bubble while ensuring the validity of these expressions even for pulsatile flow in the low kilohertz range. Following a discussion of EC modeling of flow in elastic tubes, continuum equations for pressure and volume flowrate were derived for both pulsatile and transient flow.

When studying time-dependent phenomena experimentally one automatically introduces a plethora of potential sources of error, so much care has been taken in addressing the most likely of these. To this end the experimental verification of the Hagen–Poiseuille law was used as evidence that the highest attainable accuracy is given by the manufacturer-specified tolerances on the tubing, while the effects of temperature variations on the rheological parameters were shown to be of no importance.

No current setup is capable of delivering pulsatile pressures into the low kilohertz range while also delivering stroke volumes of about  $0.1 \text{ mm}^3$ . Such a setup has been developed

based on a linear voice coil actuator acting on an elastomeric membrane, which separates the water from the actuator. A circuit model was developed for this setup, coupling it to the EC equations. The setup was operated using standardized laboratory equipment and data acquisition was done with the software LABVIEW.

The motion of an air bubble exposed to a pulsatile pressure was studied to test the performance of the setup and quantify the agreement between the developed EC models and the experimental data. Assuming the presence of a small air bubble, model and experiment yielded the same results through the entire probed frequency range of 1-100 Hz. The build-up of pressure in a transient Poiseuille flow problem was also studied experimentally and its results compared to EC model predictions, again to good agreement. The continuum models were also tested against this experimental data, but their performance was not superior to the mathematically simpler EC models, and was thus abandoned.

With the good agreement found between EC models and experiments, it was suggested to use the experimentally determined dynamic response of a component to deduce a characteristic parameter for said component, and the proposed method was illustrated using a commercially available elastomeric duckbill valve. The agreement between model and experimental data was not convincing, and the characteristic elastic valve parameter was insignificant compared to the influence of air bubbles. Removal of the valve resulted in good agreement between model and experiment, suggesting the proposed model of the valve to be insufficient or that wrong input parameters were used. This has not been studied further due to a lack of time.

## 8.2 Outlook

The current proof of the applicability of EC modeling to transient and pulsatile flows builds further confidence in the method as a predictive tool for microfluidics. Even fairly disparate systems such as those studied in this thesis are hence sufficiently described by the approach, which in itself is remarkable, but which also renders analysis of complex microfluidic systems very easy as long as care is taken in accounting for all elements. Many numerical tools have been developed specifically for solving such lumped-parameter systems, e.g. MATLAB's SIMULINK, and any of these can be employed to solve the governing equations, greatly reducing the computational time and effort.

The predictive capabilities studied in chapter 7 of exposing a component to a pulsatile pressure and deducing its characteristics from the transmitted pressure amplitudes can be taken much further, although changes must be made if the developed setup is used, as a method for eliminating the presence of air bubbles in the sensors is required. The time-dependence of any component may be studied using the approach as long as a said component can be modeled within the EC framework. It is imperative for the ultimate success of the method that only one free parameter is to be deduced from the pulsatile measurements, as one is otherwise not certain of the uniqueness of the solution found.



## Appendix A

# Mathematical derivations for $Z_{\text{Wom}}$

The mathematical derivation of various properties relating to the behavior of  $Z_{\text{Wom}}$  will be given in this appendix. The Womersley impedance is given by eq. (2.26), but is restated here for convenience:

$$Z_{\text{Wom}} = \frac{\rho\omega\ell}{\pi a^2} i \left[ 1 - \frac{2 J_1 \left( \alpha i^{\frac{3}{2}} \right)}{i^{\frac{3}{2}} \alpha J_0 \left( \alpha i^{\frac{3}{2}} \right)} \right]^{-1} \quad (\text{A.1})$$

### A.1 Asymptotic behavior of $Z_{\text{Wom}}$

It is argued in sec. 2.5 that  $Z_{\text{Wom}} \rightarrow i\omega L_{\text{hyd}}$  for  $\alpha \rightarrow \infty$  where  $L_{\text{hyd}}$  is the regular hydraulic inductance of eq. (2.21); the mathematical arguments were left out of the main text, but are given here.

The Bessel functions  $J_n(x)$  may for large  $x$  be approximated by, [65]

$$J_n(x) \approx \sqrt{\frac{2}{\pi x}} \cos \left( x - \frac{\pi}{2}n - \frac{\pi}{4} \right) \quad (\text{A.2})$$

From the series expansion of cosine have to second order accuracy, [65]

$$\cos(x) \approx 1 - \frac{x^2}{2} \quad (\text{A.3})$$

Thus, to second order for large  $x$  find

$$J_n(x) \approx \sqrt{\frac{2}{\pi x}} \left( 1 - \frac{x^2}{2} \right) \quad (\text{A.4})$$

Hence, the fraction in the bracket in the definition of  $Z_{\text{Wom}}$ , eq. (A.1) is to second order accuracy given by

$$\frac{2 J_1 \left( \alpha i^{\frac{3}{2}} \right)}{i^{\frac{3}{2}} \alpha J_0 \left( \alpha i^{\frac{3}{2}} \right)} \approx \frac{2}{\alpha i^{\frac{3}{2}}} \quad (\text{A.5})$$

Noting that the prefactor to eq. (A.1) is in fact  $i\omega L_{\text{hyd}}$  for a tube of circular cross section, the full equation for  $Z_{\text{Wom}}$  may now be rewritten as

$$Z_{\text{Wom}} = i\omega L_{\text{hyd}} \frac{1}{1 - \frac{2}{\alpha i^{\frac{3}{2}}}} \quad (\text{A.6})$$

The fraction tends to unity as  $\omega \rightarrow \infty$  since  $\alpha \propto \sqrt{\omega}$  so  $Z_{\text{Wom}} \rightarrow i\omega L_{\text{hyd}}$  in this limit, meaning that inertia dominates for high frequencies.

## A.2 Dependence of $R_{\text{hyd}}^{\text{Wom}}$ on $\alpha$

It was shown in sec. 2.5.1 that the time-averaged hydraulic resistance of Womersley flow over an oscillation period can be obtained from the hydraulic impedance, eq. (2.35) as

$$R_{\text{hyd}}^{\text{Wom}} = \frac{1}{\text{Re} \left[ \frac{1}{Z_{\text{Wom}}} \right]} \quad (\text{A.7})$$

and it was observed that  $R_{\text{hyd}}^{\text{Wom}} \propto \alpha^3$  in fig. 2.4. The origin of this relation will be revealed in this appendix.

As argued above, the fraction from the definition of  $Z_{\text{Wom}}$  eq. (A.1) becomes to second order accuracy

$$\frac{2 J_1 \left( \alpha i^{\frac{3}{2}} \right)}{i^{\frac{3}{2}} \alpha J_1 \left( \alpha i^{\frac{3}{2}} \right)} \approx \frac{2}{\alpha i^{\frac{3}{2}}}. \quad (\text{A.8})$$

$\alpha$  depends on  $\sqrt{\omega}$ , so by rewriting the prefactor to the parenthesis in the expression for  $Z_{\text{Wom}}$ , one obtains

$$R_{\text{hyd}}^{\text{Wom}} \approx \frac{1}{\text{Re} \left[ \frac{\pi a^4}{\ell \eta} \left[ \frac{1}{i \alpha^2} - \frac{2}{\alpha^3 i^{\frac{5}{2}}} \right] \right]}. \quad (\text{A.9})$$

From complex analysis one finds  $i^{\frac{5}{2}} = \frac{\sqrt{2}}{2} (-1 + i)$ , and the prefactor in the denominator is recognized as a fraction of the hydraulic resistance of Poiseuille flow,  $\frac{\pi a^4}{\ell \eta} = \frac{8}{R_{\text{hyd}}^{\text{Pois}}}$ , by comparison to eq. (2.9). Inserting these into the equation above and taking the real value, one reaches the sought expression as

$$R_{\text{hyd}}^{\text{Wom}} \approx \frac{1}{\text{Re} \left[ \frac{8}{R_{\text{hyd}}^{\text{Pois}}} \left[ -\frac{i}{\alpha^2} - \frac{\sqrt{2}(1+i)}{\alpha^3} \right] \right]} \quad (\text{A.10a})$$

$$\approx \frac{R_{\text{hyd}}^{\text{Pois}}}{\sqrt{2}} \left( \frac{\alpha}{2} \right)^3 \quad (\text{A.10b})$$

Since  $\alpha_c = \alpha/\gamma_1$ , eq. (2.17), this result is also valid for  $\alpha_c$ .

## Appendix B

# Additional topics in elastic tube flow

The work on flow in elastic tubes has yielded theoretical results which have not been used for the work presented in the thesis. These results include derivation of the famed Moens-Korteweg PDE for flow in elastic tubes (which is a special case of the result stated in eq. (3.21)), a method for including (small) liquid compliance in the EC framework and an attempted full solution to the coupled elastodynamic and fluid dynamics equations for pulsatile flow. These results are included in this appendix in no particular order for the future use of other students.

### B.1 Liquid compliance

As stated in sec. 2.1, the liquid may for most purposes of this work be considered incompressible to a high level of approximation. If one was to deviate from this notion, liquid compressibility may easily be included into the EC framework as a compliance. Consider the definition of the bulk modulus  $K$ :

$$K = -\mathcal{V} \frac{\partial p}{\partial \mathcal{V}} \quad (\text{B.1})$$

where  $\mathcal{V}$  is the volume of liquid and  $p$  its pressure. From the definition of compliance, eq. (2.23), it is evident that liquid compressibility is given by:

$$C_{\text{hyd}} = \frac{\mathcal{V}}{K} \quad (\text{B.2})$$

The bulk modulus for water at 20 °C and standard atmospheric conditions is  $K = 2.2 \times 10^9$  Pa, so for a 10 cm tube of inner radius 0.1 mm the compliance from liquid compressibility is  $C_{\text{hyd}} = 1.43 \times 10^{-18}$  m<sup>3</sup> Pa<sup>-1</sup>. If the tube is made of silicone rubber (which has Young's Modulus of  $E = 2.05 \times 10^6$  Pa) and has a wall thickness of 0.1 mm the wall compliance is  $C_{\text{hyd}} = 3.06 \times 10^{-15}$  m<sup>3</sup> Pa<sup>-1</sup>, two to three thousand times greater than the liquid compliance which hence is negligible. Contrarily, if the tube was made of

teflon with  $E = 5 \times 10^8$  Pa the wall compliance would be  $C_{\text{hyd}} = 1.26 \times 10^{-17} \text{ m}^3 \text{ Pa}^{-1}$ , only about 8 to 10 times greater than the liquid compliance which then cannot readily be neglected.

## B.2 The Moens-Korteweg pressure equation

The first analytical model of the arterial pulse pressure<sup>1</sup> was presented in 1878 by Moens, [34], and Korteweg, [35]. Neglecting viscous effects and using the thin-wall approximation in the wall compliance, eq. (3.13) (i.e.  $\beta = 1$ ), the much-celebrated Moens-Korteweg pressure equation may be read off eq. (3.21) immediately

$$\partial_x^2 p(x, t) = \frac{1}{c_{\text{MK}}^2} \partial_t^2 p(x, t) \quad (\text{B.3})$$

with  $c_{\text{MK}} = \sqrt{\frac{Eh}{2\rho a}}$ . Since viscosity has been omitted, no losses are inflicted to the pressure which thus travels undamped throughout the tube. This equation is often stated in biophysical textbooks, e.g. [67]; although theoretical and experimental results disagree with its predictions, it does hint at the correct dynamics.

## B.3 Full solution to the governing fluid and solid equations

A solution to the full coupled problem of viscous flow in elastic tubes has been attempted, although in vain. The attempted solution is detailed in the following.

### B.3.1 Governing equations

In the absence of external body forces and under the assumption of negligible heat exchange in the solid during times on the order of oscillatory motions, the equation of motion of the solid - the so-called elastodynamic equation - is given by, [26]

$$\rho_w \partial_t^2 \mathbf{u} = \mu_w \nabla^2 \mathbf{u} + (\lambda_w + \mu_w) \nabla (\nabla \cdot \mathbf{u}) \quad (\text{B.4})$$

The governing equations for the fluid motion are the Stokes and continuity equations in their incompressible forms, eqs. (2.4) and (2.3).

Due to the geometry of the problem a cylindrical reference frame  $(r, \phi, x, t)$  is chosen, with  $x$  placed along the axis of the tube. As for the problem of pulsatile fluid flow in a fully rigid tube of sec. 2.3, the present problem may be simplified by introduction of rotational symmetry. No further simplifications may readily be made, so all fields must depend on  $r$ ,  $x$  and  $t$ . Thus without angular dependence, the components of the equation

---

<sup>1</sup>The first analytical expression for pulsatile flow in elastic vessels was derived by Witzig, [66].

of motion of the tube in cylindrical coordinates are

$$\begin{aligned} \rho_w \partial_t^2 u_r(r, x, t) = & \mu_w \left[ \partial_r^2 u_r(r, x, t) + \frac{1}{r} \partial_r u_r(r, x, t) - \frac{u_r(r, x, t)}{r^2} + \partial_x^2 u_r(r, x, t) \right] \\ & + (\lambda_w + \mu_w) \left[ \frac{1}{r} \partial_r u_r(r, x, t) - \frac{u_r(r, x, t)}{r^2} + \partial_r^2 u_r(r, x, t) + \partial_r \partial_x u_x(r, x, t) \right] \end{aligned} \quad (\text{B.5a})$$

$$\begin{aligned} \rho_w \partial_t^2 u_x(r, x, t) = & \mu_w \left[ \partial_r^2 u_x(r, x, t) + \frac{1}{r} \partial_r u_x(r, x, t) + \partial_x^2 u_x(r, x, t) \right] \\ & + (\lambda_w + \mu_w) \left[ \frac{1}{r} \partial_x u_r(r, x, t) + \partial_x \partial_r u_r(r, x, t) + \partial_x^2 u_x(r, x, t) \right] \end{aligned} \quad (\text{B.5b})$$

The simplified equations of motion for the fluid flow are similar to those governing the Womersley problem with one notable exception: due to the dilatation of the walls, a radial velocity component  $v_r(r, x, t)$  must be included. As a result, the simplified Stokes equation is non-zero in two coordinate directions as opposed to the one dimensionality of the simplified Womersley problem. The velocity components are

$$\partial_t v_r(r, x, t) = -\frac{1}{\rho} \partial_r p(r, x, t) + \nu \left[ \partial_r^2 v_r(r, x, t) + \frac{1}{r} \partial_r v_r(r, x, t) - \frac{v_r(r, x, t)}{r^2} + \partial_x^2 v_r(r, x, t) \right] \quad (\text{B.6a})$$

$$\partial_t v_x(r, x, t) = -\frac{1}{\rho} \partial_x p(r, x, t) + \nu \left[ \partial_r^2 v_x(r, x, t) + \frac{1}{r} \partial_r v_x(r, x, t) + \partial_x^2 v_x(r, x, t) \right] \quad (\text{B.6b})$$

and the continuity equation becomes

$$\partial_x v_x(r, x, t) + \partial_r v_r(r, x, t) + \frac{v_r(r, x, t)}{r} = 0 \quad (\text{B.7})$$

### B.3.2 Boundary conditions

The boundary conditions coupling the fluid and wall motions involve the continuity of stress and velocity at the interface and boundedness of the velocity and pressure fields; the conditions may be specified as:

1. Fluid velocity components and pressure are finite at  $r = 0$ .
2. The no-slip boundary condition requires the radial and axial velocity components of the tube and the fluid to be continuous at  $r = a$ .
3. The fluid and tube stresses at  $r = a$  are continuous.
4. The wall stresses at  $r = b$  are zero.

By use of the incompressible fluid stress tensor (see [1]) along with the wall stress tensor (see [26]), each evaluated under the assumption of rotational symmetry, these conditions

are equivalent to

$$v_r(0, x, t) = 0 \quad (\text{B.8a})$$

$$|p(r, x, t)| < \infty \quad (\text{B.8b})$$

$$\partial_r v_x(0, x, t) = 0 \quad (\text{B.8c})$$

$$v_r(a, x, t) = \partial_t u_r(a, x, t) \quad (\text{B.8d})$$

$$v_x(a, x, t) = \partial_t u_x(a, x, t) \quad (\text{B.8e})$$

$$\eta [\partial_x v_r(a, x, t) + \partial_r v_x(a, x, t)] = \mu_w [\partial_x u_r(a, x, t) + \partial_r u_x(a, x, t)] \quad (\text{B.8f})$$

$$-p(a, x, t) + 2\eta \partial_r v_r(a, x, t) = 2\mu_w \partial_r u_r(a, x, t) + \lambda_w \left[ \frac{u_r(a, x, t)}{a} + \partial_r u_r(a, x, t) + \partial_x u_x(a, x, t) \right] \quad (\text{B.8g})$$

$$0 = \mu_w [\partial_x u_r(b, x, t) + \partial_r u_x(b, x, t)] \quad (\text{B.8h})$$

$$0 = 2\mu_w \partial_r u_r(b, x, t) + \lambda_w \left[ \frac{u_r(b, x, t)}{b} + \partial_r u_r(b, x, t) + \partial_x u_x(b, x, t) \right] \quad (\text{B.8i})$$

### B.3.3 Solving the fluid problem

The pressure and velocity components are assumed to be of the form

$$p(r, x, t) = \sum_{n=0}^{\infty} P^n(r) e^{i(n\omega t - k_n x)} \quad (\text{B.9a})$$

$$v_r(r, x, t) = \sum_{n=0}^{\infty} V_r^n(r) e^{i(n\omega t - k_n x)} \quad (\text{B.9b})$$

$$v_x(r, x, t) = \sum_{n=0}^{\infty} V_x^n(r) e^{i(n\omega t - k_n x)} \quad (\text{B.9c})$$

where  $\omega$  is the angular frequency of the oscillations,  $n$  is the harmonic number and  $k_n$  is the propagation constant (wave number) of the  $n^{\text{th}}$  harmonic. The superscript  $n$  in the functions  $P^n(r)$ ,  $V_r^n(r)$  and  $V_x^n(r)$  is used to indicate that a distinct function exists for each harmonic. Contrary to regular Womersley flow in rigid confinement, a radial dependence on the pressure is assumed.

Plugging these guesses into the simplified fluid equations, eqs. (B.6a), (B.6b) and (B.7), yields for all  $n$

$$in\omega V_r^n(r) = -\frac{1}{\rho} \partial_r P^n(r) + \nu \left[ \partial_r^2 V_r^n(r) + \frac{1}{r} \partial_r V_r^n(r) - \frac{V_r^n(r)}{r^2} - k_n^2 V_r^n(r) \right] \quad (\text{B.10a})$$

$$in\omega V_x^n(r) = \frac{ik_n}{\rho} P^n(r) + \nu \left[ \partial_r^2 V_x^n(r) + \frac{1}{r} \partial_r V_x^n(r) - k_n^2 V_x^n(r) \right] \quad (\text{B.10b})$$

$$0 = -ik_n V_x^n(r) + \partial_r V_r^n(r) + \frac{1}{r} V_r^n(r) \quad (\text{B.10c})$$

The solution to this set of two Bessel-type ODEs with the additional constraint imposed by the continuity equation may be solved using any of the readily available symbolic manipulation software such as Maple or Mathematica. The general solution to this problem is for all  $n$  given by

$$V_r^n(r) = C_1 I_1(k_n r) + C_2 K_1(k_n r) + C_3 J_1(i\kappa_n r) + C_4 K_1(\kappa_n r) \quad (\text{B.11a})$$

$$V_x^n(r) = -iC_1 I_0(k_n r) + iC_2 K_0(k_n r) - \frac{i\kappa_n}{k_n} [C_3 J_0(i\kappa_n r) + C_4 K_0(\kappa_n r)] \quad (\text{B.11b})$$

$$P^n(r) = -\frac{in\omega\rho}{k_n} [C_1 I_0(k_n r) - C_2 K_0(k_n r)] \quad (\text{B.11c})$$

where as usual  $J_s$  is the Bessel function of the first kind of order  $s$ , while  $I_s$  and  $K_s$  are the modified Bessel functions of the first and second kind, respectively, both of order  $s$ . The constant  $\kappa_n$  is given by

$$\kappa_n^2 = k_n^2 + \frac{in\omega}{\nu} \quad (\text{B.12})$$

and  $C_1$ ,  $C_2$ ,  $C_3$  and  $C_4$  are complex constants of integration.

Boundedness on the pressure, eq. (B.8b), requires  $C_2 = 0$  since  $K_0(x) \rightarrow \infty$  as  $x \rightarrow 0$  while  $I_0(x) \rightarrow 1$  as  $x \rightarrow 0$ , so the sum inside the square bracket of eq. (B.11c) would go towards  $-\infty$  as  $r \rightarrow 0$  unless  $C_2 = 0$ .

At  $r = 0$  the radial velocity component becomes

$$V_r^n(0) = C_2 K_1(0) + C_4 K_0(0) \quad (\text{B.13})$$

since  $I_1(0) = J_1(0) = 0$ . Satisfaction of the condition  $v_r(0, x, t) = 0$  therefore requires  $C_2 = -C_4$  which implies  $C_4 = 0$  since it was just found that  $C_2 = 0$ .

Thus, the temporary solution to the fluid problem is given by

$$v_r(r, x, t) = \sum_{n=0}^{\infty} [-iC_1 J_1(ik_n r) + C_3 J_1(i\kappa_n r)] e^{i(n\omega t - k_n x)} \quad (\text{B.14a})$$

$$v_x(r, x, t) = \sum_{n=0}^{\infty} \left[ -iC_1 J_0(ik_n r) + \frac{\kappa_n}{k_n} C_3 J_0(i\kappa_n r) \right] e^{i(n\omega t - k_n x)} \quad (\text{B.14b})$$

$$p(r, x, t) = \sum_{n=0}^{\infty} \left[ -\frac{in\omega\rho}{k_n} C_1 J_0(ik_n r) \right] e^{i(n\omega t - k_n x)} \quad (\text{B.14c})$$

where use have been made of the following relationship, [65]:  $I_s(x) = i^{-s} J_s(ix)$ .

### B.3.4 Solving the wall problem

A general theorem of vector analysis states that any vector may be decomposed into the sum of a rotation free vector and a divergence free vector. As noted by Landau and Lifshitz in [26], by using the decomposition technique on the displacement vector  $\mathbf{u}$ , the PDEs for radial and axial displacements, eqs. (B.5a) and (B.5b), may be decoupled into two ODEs, one for each direction. Thus, the displacement vector is reformulated as

$$\mathbf{u} = \nabla\psi + \nabla \times \mathbf{H} \quad (\text{B.15})$$

Substituting this into eqs. (B.5a) and (B.5b) using the results of [68] one obtains the equations

$$\partial_r^2 \psi + \frac{1}{r} \partial_r \psi + \partial_x^2 \psi - \frac{\rho_w}{\lambda_w + 2\mu_w} \partial_t^2 \psi = 0 \quad (\text{B.16a})$$

$$\partial_r^2 H_\phi + \frac{1}{r} \partial_r H_\phi - \frac{H_\phi}{r^2} + \partial_x^2 H_\phi - \frac{\rho_w}{\mu_w} \partial_t^2 H_\phi = 0 \quad (\text{B.16b})$$

where  $H_\phi$  is the component of  $\mathbf{H}$  in the azimuthal direction<sup>2</sup>.

Assuming solutions in the same form as the fluid fields

$$\psi(r, x, t) = \sum_{n=0}^{\infty} \Psi^n(r) e^{i(n\omega t - k_n x)} \quad (\text{B.17a})$$

$$H_\phi(r, x, t) = \sum_{n=0}^{\infty} h^n(r) e^{i(n\omega t - k_n x)} \quad (\text{B.17b})$$

and inserting these into eqs. (B.16a) and (B.16b) one obtains a regular Bessel pseudo-ODE in each unknown for each harmonic  $n$

$$\partial_r^2 \Psi^n(r) + \frac{1}{r} \partial_r \Psi^n(r) - k_n^2 \Psi^n(r) + \frac{n^2 \omega^2 \rho_w}{\lambda_w + 2\mu_w} \Psi^n(r) = 0 \quad (\text{B.18a})$$

$$\partial_r^2 h^n(r) + \frac{1}{r} \partial_r h^n(r) - \frac{h^n(r)}{r^2} - k_n^2 h^n(r) + \frac{n^2 \omega^2 \rho_w}{\mu_w} h^n(r) = 0 \quad (\text{B.18b})$$

The general solutions to  $\Psi^n(r)$  and  $h^n(r)$  for all  $n$  are

$$\Psi^n(r) = C_5 J_0(\mathbb{Y}_n r) + C_6 Y_0(\mathbb{Y}_n r) \quad (\text{B.19a})$$

$$h^n(r) = C_7 J_1(\mathbb{M}_n r) + C_8 Y_1(\mathbb{M}_n r) \quad (\text{B.19b})$$

where  $Y_s(x)$  are used for Bessel functions of the second kind of the  $s^{\text{th}}$  order,  $C_5$ ,  $C_6$ ,  $C_7$  and  $C_8$  are complex constants of integration and the constants  $\mathbb{Y}_n$  and  $\mathbb{M}_n$  are given by

$$\mathbb{Y}_n^2 = \frac{n^2 \omega^2 \rho_w}{\lambda_w + 2\mu_w} - k_n^2 \quad (\text{B.20a})$$

$$\mathbb{M}_n^2 = \frac{n^2 \omega^2 \rho_w}{\mu_w} - k_n^2 \quad (\text{B.20b})$$

The displacement components  $u_r$  and  $u_x$  are determined from eq. (B.15) as

$$u_r(r, x, t) = \partial_r \psi(r, x, t) - \partial_x H_\phi(r, x, t) \quad (\text{B.21a})$$

$$u_x(r, x, t) = \partial_x \psi(r, x, t) + \partial_r H_\phi(r, x, t) + \frac{H_\phi(r, x, t)}{r} \quad (\text{B.21b})$$

---

<sup>2</sup>Only the displacement vector  $\mathbf{u}$  is assumed zero in the azimuthal direction, no such assumptions are made on the divergence and rotation free decomposites of  $\mathbf{u}$ .



Plugging in eqs. (B.17a) and (B.17b) with the expressions for  $\Psi^n(r)$  and  $h^n(r)$  from eqs. (B.19a) and (B.19b), one finds

$$u_r(r, x, t) = \sum_{n=0}^{\infty} \left( -\mathbb{P}_n [C_5 J_1(\mathbb{P}_n r) + C_6 Y_1(\mathbb{P}_n r)] + i k_n [C_7 J_1(\mathbb{M}_n r) + C_8 Y_1(\mathbb{M}_n r)] \right) e^{i(n\omega t - k_n x)} \quad (\text{B.22a})$$

$$u_x(r, x, t) = \sum_{n=0}^{\infty} \left( -i k_n [C_5 J_0(\mathbb{P}_n r) + C_6 Y_0(\mathbb{P}_n r)] + \mathbb{M}_n [C_7 J_0(\mathbb{M}_n r) + C_8 Y_0(\mathbb{M}_n r)] \right) e^{i(n\omega t - k_n x)} \quad (\text{B.22b})$$

Using the remaining boundary conditions of eqs. (B.8d)-(B.8i), a system of six homogeneous equations for the integration constants  $C_1$ ,  $C_3$ ,  $C_5$ ,  $C_6$ ,  $C_7$  and  $C_8$  is obtained. In theory, this system may be solved to yield a closed solution to the problem.

### B.3.5 Determining the propagation constant $k_n$

As noted above, inserting the solutions to the fluid and wall problems into the remaining boundary conditions, one finds a system of six homogeneous equations for the integration constants. It is known from mathematics that the determinant for this system must be zero for the system to have non-trivial solutions. From this determinant, given in eq. (B.24), it is possible to determine the propagation constant  $k_n$  as a function of frequency, harmonic number and system parameters. The variable  $\mathbb{K}_n$  is introduced for notational convenience in eq. (B.24) and is given by

$$\mathbb{K}_n = 2\mu_w \mathbb{P}_n^2 + \lambda_w (k_n^2 + \mathbb{P}_n^2) \quad (\text{B.23})$$

Determining the value of  $k_n$ , for which the determinant is 0 is not a trivial task due to the non-linearity of the Bessel and modified Bessel functions. A solution may be found for each harmonic  $n$  using a numerical root finding algorithm such as the Newton-Raphson algorithm or its more sophisticated relatives.

$$\begin{array}{cccccc}
-I_1(k_n a) & -iI_1(\kappa_n a) & -i\omega n \mathbb{P}_n J_1(\mathbb{H}_n a) & -i\omega n \mathbb{P}_n Y_1(\mathbb{P}_n a) & -\omega n k_n J_1(\mathbb{H}_n a) & -\omega n k_n Y_1(\mathbb{H}_n a) \\
iI_0(k_n a) & -\frac{\kappa_n}{k_n} I_0(\kappa_n a) & \omega n k_n J_0(\mathbb{P}_n a) & \omega n k_n Y_0(\mathbb{P}_n a) & i\omega n \mathbb{H}_n J_0(\mathbb{H}_n a) & i\omega n \mathbb{H}_n Y_0(\mathbb{H}_n a) \\
2i\eta k_n I_1(k_n a) & -\eta \kappa_n \left(1 + \frac{\kappa_n^2}{k_n^2}\right) I_1(\kappa_n a) & 2i\mu_w k_n \mathbb{P}_n J_1(\mathbb{P}_n a) & 2i\mu_w k_n \mathbb{P}_n Y_1(\mathbb{P}_n a) & \mu_w (k_n^2 - \mathbb{H}_n^2) J_1(\mathbb{H}_n a) & \mu_w (k_n^2 - \mathbb{H}_n^2) Y_1(\mathbb{H}_n a) \\
\frac{2\eta}{a} I_1(k_n a) & 2i\eta \left[ \kappa_n I_0(\kappa_n a) \right. & \frac{2\mu_w \mathbb{P}_n}{a} J_1(\mathbb{P}_n a) & \frac{2\mu_w \mathbb{P}_n}{a} Y_1(\mathbb{P}_n a) & 2i\mu_w k_n \left[ \mathbb{H}_n J_0(\mathbb{H}_n a) \right. & 2i\mu_w k_n \left[ \mathbb{H}_n Y_0(\mathbb{H}_n a) \right. \\
- \left( 2\eta k_n + \frac{i n \omega \rho}{k_n} \right) I_0(k_n a) & \left. - \frac{I_1(\kappa_n a)}{a} \right] & -\mathbb{A}_n J_0(\mathbb{P}_n a) & -\mathbb{A}_n Y_0(\mathbb{P}_n a) & \left. - \frac{J_1(\mathbb{H}_n a)}{a} \right] & \left. - \frac{Y_1(\mathbb{H}_n a)}{a} \right] \\
0 & 0 & 2i\mu_w k_n \mathbb{P}_n J_1(\mathbb{P}_n b) & 2i\mu_w k_n \mathbb{P}_n Y_1(\mathbb{P}_n b) & \mu_w (k_n^2 - \mathbb{H}_n^2) J_1(\mathbb{H}_n b) & \mu_w (k_n^2 - \mathbb{H}_n^2) Y_1(\mathbb{H}_n b) \\
0 & 0 & \frac{2\mu_w \mathbb{P}_n}{b} J_1(\mathbb{P}_n b) & \frac{2\mu_w \mathbb{P}_n}{b} Y_1(\mathbb{P}_n b) & 2i\mu_w k_n \left[ \mathbb{H}_n J_0(\mathbb{H}_n b) \right. & 2i\mu_w k_n \left[ \mathbb{H}_n Y_0(\mathbb{H}_n b) \right. \\
& & -\mathbb{A}_n J_0(\mathbb{P}_n b) & -\mathbb{A}_n Y_0(\mathbb{P}_n b) & \left. - \frac{J_1(\mathbb{H}_n b)}{b} \right] & \left. - \frac{Y_1(\mathbb{H}_n b)}{b} \right]
\end{array} \tag{B.24}$$

## B.4 The motion of the liquid

The fluid problem is a function of the two constants  $C_1$  and  $C_3$ , but may be reformulated using only one arbitrary constant as follows. The six boundary conditions that gives rise to the determinant of eq. (B.24) may formally be written as a linear and homogeneous system of equations as

$$\mathbb{A}\mathbf{C} = \mathbf{0} \quad (\text{B.25})$$

where  $\mathbb{A}$  is the  $6 \times 6$  coefficient matrix to which eq. (B.24) is the corresponding determinant,  $\mathbf{C} = [C_1, C_3, C_5, C_6, C_7, C_8]^T$  is the vector of unknown constants and  $\mathbf{0}$  is a  $6 \times 1$  vector of zeros. Normalizing all equations by the variable  $C_3$  results in the following system of equations

$$\tilde{\mathbb{A}}\tilde{\mathbf{C}} = \mathbf{b} \quad (\text{B.26})$$

where

$$\tilde{\mathbb{A}} = \begin{bmatrix} A_{1,1} & A_{1,3} & A_{1,4} & A_{1,5} & A_{1,6} \\ A_{2,1} & A_{2,3} & A_{2,4} & A_{2,5} & A_{2,6} \\ A_{3,1} & A_{3,3} & A_{3,4} & A_{3,5} & A_{3,6} \\ A_{4,1} & A_{4,3} & A_{4,4} & A_{4,5} & A_{4,6} \\ 0 & A_{5,3} & A_{5,4} & A_{5,5} & A_{5,6} \\ 0 & A_{6,3} & A_{6,4} & A_{6,5} & A_{6,6} \end{bmatrix} \quad \tilde{\mathbf{C}} = \frac{1}{C_3} \begin{bmatrix} C_1 \\ C_5 \\ C_6 \\ C_7 \\ C_8 \end{bmatrix} \quad \mathbf{b} = \begin{bmatrix} -A_{1,2} \\ -A_{2,2} \\ -A_{3,2} \\ -A_{4,2} \\ 0 \\ 0 \end{bmatrix} \quad (\text{B.27})$$

The indices on the entries  $A_{i,j}$  refer to the original coefficient matrix  $\mathbb{A}$ . This system of equations may be solved for the new constants  $\tilde{C}_i$  to establish the following correlation between the two constants of the fluid problem:

$$\frac{C_1}{C_3} = -\frac{A_{4,2}}{A_{4,1}} = -\frac{2i\eta \left[ \kappa_n I_0(\kappa_n a) - \frac{I_1(\kappa_n a)}{a} \right]}{\frac{2\eta}{a} I_1(k_n a) - \left( 2\eta k_n + \frac{i n \omega \rho}{k_n} \right) I_0(k_n a)} = -\mathbb{X}_n \quad (\text{B.28})$$

With the propagation constants from eq. (B.24) for each  $n$  in hand, the motion of the liquid is fully determined by eqs. (B.14a)-(B.14c) and the interdependence of the constants  $C_1$  and  $C_3$  stated above. Expressed in only one constant, the  $n^{\text{th}}$  harmonic of the velocity components in the liquid are

$$V_r^n(r) = -C_1 \left[ iJ_1(ik_n r) + \frac{1}{\mathbb{X}_n} J_1(i\kappa_n r) \right] \quad (\text{B.29a})$$

$$V_x^n(r) = -C_1 \left[ J_0(ik_n r) + \frac{\kappa_n}{k_n} \frac{1}{\mathbb{X}_n} J_0(i\kappa_n r) \right] \quad (\text{B.29b})$$

The axial flowrate is found as the integral of  $v_x(r, x, t)$  across the tube cross section; the  $n^{\text{th}}$  harmonic of this parameter is given by<sup>3</sup>

$$Q^n = -n\omega\rho C_1 J_0(ik_n a) \left[ \frac{2J_1(ik_n a)}{n\omega\rho k_n a J_0(ik_n a)} - \frac{2i}{\mathbb{X}_n} \frac{J_1(i\kappa_n a)}{n\omega\rho k_n a J_0(ik_n a)} \right] \pi a^2 \quad (\text{B.30})$$

<sup>3</sup>The summation and integration operations may be interchanged since the integral over the tube cross section reduces to an integral in  $r$ ; this last property arises as a consequence of the assumption of no azimuthal dependence.

The prefactor outside the bracket is recognized as the axial pressure gradient, so for each harmonic, the flowrate depends linearly on the pressure gradient. Thus, the  $n^{\text{th}}$  harmonic of the hydraulic impedance is given by

$$Z_{\text{hyd}}^n = \left( \left[ \frac{2J_1(\mathrm{i}k_n a)}{n\omega\rho k_n a J_0(\mathrm{i}k_n a)} - \frac{2\mathrm{i}}{\aleph_n} \frac{J_1(\mathrm{i}k_n a)}{n\omega\rho k_n a J_0(\mathrm{i}k_n a)} \right] \pi a^2 \right)^{-1} \quad (\text{B.31})$$

#### B.4.1 Problems

Although this theory appears flawless, numerical solutions to the determinant explode yielding very un-physical results, subsequently leading to the abandoning of the theory. A thorough investigation of the reasons for this shortcoming has not been conducted to save to time, but is left to any reader of these pages.

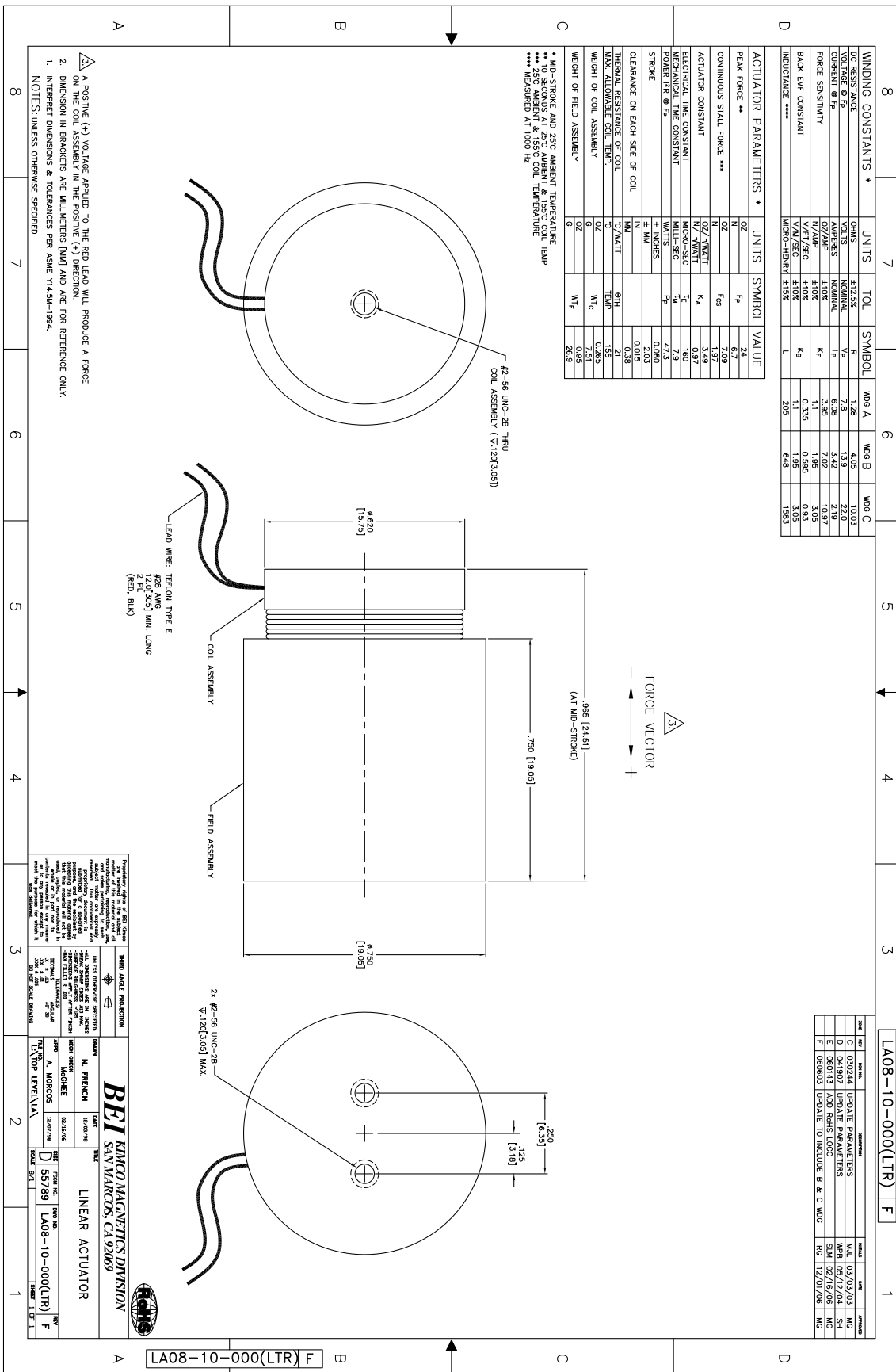
#### B.4.2 A note on turbulent pipe flow

It is an experimentally well-documented fact that pipe flow for  $Re \gtrsim 2300$ , the flow will first become unstable a certain distance downstream of the inlet before breaking up into fully chaotic turbulent flow further downstream. To the knowledge of this author, theoretical explanations for this phenomenon have not been presented. However, as shown in this chapter, when one includes the elasticity of the pipe walls, a radial velocity component is introduced; this component is not present in the Poiseuille solution which is purely axial. At values of  $Re$  around 2000 where inertia dominates, this velocity component will introduce disturbances to the flow which conceivably could spur turbulence. Since the pipe of any experiment is elastic, this may explain the discrepancy between experiment and theory.

## Appendix C

# BEI Kimco LA08-10-000A data sheet

The data sheet for the actuator used as the driving mechanism of the pressure source is shown here for good measure. It may be found online at  
[http://www.beikimco.com/pdf/LA08-10-000%20\(LTR\).pdf](http://www.beikimco.com/pdf/LA08-10-000%20(LTR).pdf)



# Bibliography

- [1] H. Bruus, *Theoretical Microfluidics*. Oxford: Oxford University Press, 2008.
- [2] P. Skafte-Pedersen, “Acoustic forces on particles and liquids in microfluidic systems,” Master’s thesis, Technical University of Denmark, Department of Micro- and Nanotechnology, 2008.
- [3] L. H. Olesen, *AC electrokinetic micropumps*. PhD thesis, Technical University of Denmark, Department of Micro- and Nanotechnology, 2006.
- [4] T. Thorsen, S. Maerkl, and S. R. Quake, “Microfluidic large-scale integration,” *Science*, vol. 298, pp. 580–584, 2002.
- [5] D. Lo Jacono, F. Plouraboué, and A. Bergeon, “Weak-inertial flow between two rough surfaces,” *Phys. Fluids*, vol. 17, 2005.
- [6] D. Kim, N. C. Chesler, and D. J. Beebe, “A method for dynamic system characterization using hydraulic series resistance,” *Lab on a Chip*, vol. 6, pp. 639–644, 2006.
- [7] A. Sinclair, V. Timchenko, J. Reizes, G. Rosengarten, and E. Leonardi, “An experimental and numerical study of a micro-synthetic jet in a shallow cavity,” in *Proceedings of the Sixth International ASME Conference on Nanochannels, Microchannels and Minichannels, ICNMM*, 2008.
- [8] C. J. Morris and F. K. Forster, “Low-order modeling of resonance for fixed-valve micropumps based on first principles,” *J. MEMS*, vol. 12, pp. 325–334, 2003.
- [9] C. J. Morris and F. K. Forster, “Oscillatory flow in microchannels - Comparison of exact and approximate impedance models with experiments,” *Exp. Fluids*, vol. 36, pp. 928–937, 2004.
- [10] A. Olsson, G. Stemme, and E. Stemme, “A numerical design study of the valveless diffuser pump using a lumped-mass model,” *J. Micromech. Microeng.*, vol. 9, no. 1, pp. 34–44, 1999.
- [11] T. Zhang and Q.-M. Wang, “Performance evaluation of a valveless micropump driven by a ring-type piezoelectric actuator,” *IEEE Transactions on Ultrasonics, Ferroelectrics and Frequency Control*, vol. 53, pp. 463–473, February 2006.

- [12] A. Brask, "Principles of electroosmotic pumps," Master's thesis, Technical University of Denmark, MIC - Department of Micro and Nanotechnology, 2003.
- [13] T. Bourouina and J.-P. Grandchamp, "Modeling micropumps with electrical equivalent networks," *J. Micromech. Microeng.*, vol. 6, pp. 398–404, 1996.
- [14] Q. Lin, B. Yang, J. Xie, and Y.-C. Tai, "Dynamic simulation of a peristaltic micropump considering coupled fluid flow and structural motion," *J. Micromech. Microeng.*, vol. 17, pp. 220–228, 2007.
- [15] R. Zengerle and M. Richter, "Simulation of microfluidic systems," *J. Micromech. Microeng.*, vol. 4, pp. 192–204, 1994.
- [16] L. D. Landau and E. M. Lifshitz, *Fluid Mechanics*. volume 6 of A Course of Theoretical Physics, Oxford: Butterworth-Heinemann, 2<sup>nd</sup> ed., 2006.
- [17] G. Batchelor, *An introduction to fluid dynamics*. Cambridge: Cambridge University Press, 2000.
- [18] F. M. White, *Viscous Fluid Flow*. NY: McGraw-Hill, 3<sup>rd</sup> ed., 2006.
- [19] J. R. Womersley, "Method for the calculation of velocity, rate of flow and viscous drag in arteries when the pressure gradient is known," *J. Physiol.*, vol. 127, pp. 553–563, 1955.
- [20] S. Uchida, "The pulsating viscous flow superposed on the steady laminar motion of incompressible fluid in a circular pipe," *Zeitschrift für Angewandte Mathematik und Physik (ZAMP)*, vol. 7, pp. 403–422, 1956.
- [21] P. Lambossy, "Forced oscillations of an incompressible, viscous liquid in a rigid, horizontal pipe. Calculation of the friction," *Helv. Phys. Acta*, vol. 25, pp. 371–386, 1952.
- [22] T. Sævi, "Über den von E. G. Richardson entdeckten "Annulareffekt",", *Z. Phys.*, vol. 61, pp. 349–362, 1930.
- [23] B. Elbek, *Elektromagnetisme*. University of Copenhagen: Niels Bohr Institute, 1997. Lecture notes.
- [24] W. Zielke, *Frequency dependent friction in transient pipe flow*. PhD thesis, University of Michigan, Department of Civil Engineering, 1966.
- [25] W. L. Brown, D. G. Fabricant, and D. A. Boyd, "Thermal considerations in modern spectrograph design: the Binospec spectrograph," *Proc. SPIE - Int'l Society for Optical Engineers*, vol. 4841, pp. 1265–72, 2003.
- [26] L. D. Landau and E. M. Lifshitz, *Theory of Elasticity*. volume 7 of A Course of Theoretical Physics, Oxford: Pergamon Press, 3<sup>rd</sup> ed., 1986.
- [27] T. A. Osswald, E. Baur, S. Brinkmann, K. Oberbach, and E. Schmachtenberg, *International Plastics Handbook*. Munich: Carl Hanser Verlag, 2006.



- [28] B. Sundström (editor), *Handbok och formelsamling i Hållfasthetslära*. Stockholm: Institutionen för hållfasthetslära, KTH, 2<sup>nd</sup> ed., 1999.
- [29] B. Lautrup, *Physics of continuous matter: Exotic and everyday phenomena in the macroscopic world*. New York: CRC Press, 2004.
- [30] S. P. Timoshenko and S. Woinowsky-Krieger, *Theory of Plates and Shells*. New York: McGraw-Hill, 2<sup>nd</sup> ed., 1959.
- [31] J. R. Womersley, “An elastic tube theory of pulse transmission and oscillatory flow in mammalian arteries,” tech. rep., Wright Air Development Center (WADC-TR) 56-614, 1957.
- [32] G. W. Morgan and J. P. Kiely, “Wave propagation in a viscous liquid contained in a flexible tube,” *J. Acoust. Soc. Am.*, vol. 26, pp. 323–28, 1954.
- [33] G. W. Morgan and W. R. Ferrante, “Wave propagation in elastic tubes filled with streaming liquid,” *J. Acoust. Soc. Am.*, vol. 27, pp. 715–25, 1955.
- [34] A. I. Moens, *Die Pulskurve*. 1878.
- [35] D. J. Korteweg, “Über die fortpflanzungsgeschwindigkeit des schalles in elastiichen rohren,” *Ann. Phys. Chem. (NS)*, vol. 5, pp. 52–537, 1878.
- [36] R. H. Cox, “Wave propagation through a newtonian fluid contained within a thick-walled, viscoelastic tube,” *Biophysical Journal*, vol. 8, pp. 691–709, 1968.
- [37] E. O. Attinger (editor), *Pulsatile blood flow*. New York: McGraw-Hill, 1964.
- [38] R. Cox, “Comparison of linearized wave propagation models for arterial blood flow analysis,” *J. Biomechanics*, vol. 2, pp. 251–265, 1969.
- [39] A. S. Iberall, “Attenuation of oscillatory pressures in instrument lines,” *J. Res. Nat. Bur. Stand.*, vol. 45, pp. 85–108, 1950.
- [40] J. H. Olsen and A. H. Shapiro, “Large-amplitude unsteady flow in liquid-filled elastic tubes,” *J. Fluid Mech.*, vol. 29, pp. 513–38, 1967.
- [41] M. G. Taylor, “An experimental determination of the propagation of fluid oscillations in a tube with viscoelastic wall; together with an analysis of the characteristics required in an electrical analogue,” *Phys. Med. Biol.*, vol. 4, pp. 63–82, 1959.
- [42] B. Schaaf and P. Abbrecht, “Digital computer simulation of human systemic arterial pulse wave transmission: a nonlinear model,” *J. Biomechanics*, vol. 5, pp. 345–364, 1972.
- [43] J. Mäkinen, R. Piché, and A. Ellman, “Fluid transmission line modelling using a variational method,” *J. Dyn. Sys. Meas. Control*, vol. 122, pp. 153–162, 2000.

- [44] G. D. C. Kuiken, "Wave propagation in fluid lines," *Appl. Scien. Res.*, vol. 41, pp. 69–91, 1984.
- [45] D. R. Lide (editor-in-chief), *CRC Handbook of Chemistry and Physics*. New York, NY: CRC Press, 1993.
- [46] R. K. Shah and A. L. London, *Laminar Flow Forced Convection in ducts*. New York, NY: Academic Press, 1978.
- [47] L. C. Passarini and P. R. Nakajima, "Development of high-speed solenoid valve: an investigation of the importance of armature mass on the dynamic response," *J. Braz. Soc. Mech. Sci. & Eng.*, vol. 25, pp. 329–335, 2003.
- [48] Lee LFPA High Speed Piezo Electric Valves. <http://www.theleeco.com/EFSWEB2.NSF/4c8c908c6ad08610852563a9005dae17/be7364660b4157f7852563d2007a2706!OpenDocument>, Last accessed 26 January, 2009.
- [49] Yuken High Speed Servo Valves. [http://www.yuken.org/Brochures/EL-0610\\_LSV\(H\)G.pdf](http://www.yuken.org/Brochures/EL-0610_LSV(H)G.pdf), Last accessed 26 January, 2009.
- [50] A. V. Oppenheim and R. W. Schaffer, *Digital Signal Processing*. New Jersey: Prentice-Hall, 1975.
- [51] R. G. Gilbertson and J. D. Busch, "A survey of micro-actuator technologies for future spacecraft missions," *The Journal of The British Interplanetary Society*, vol. 49, pp. 129–138, 1996.
- [52] D. J. Laser and J. G. Santiago, "A review of micropumps," *J. Micromech. Microeng.*, vol. 14, pp. R35–R64, 2004.
- [53] A. Andersson. Parameter AB, Private communication.
- [54] Wikipedia, "Pixelation." <http://en.wikipedia.org/wiki/Pixelation>, Last accessed 5 January, 2009.
- [55] F. Bretherton, "The motion of long bubbles in tubes," *J. Fluid Mech.*, vol. 10, pp. 166–188, 1961.
- [56] C.-W. Park and G. M. Homsy, "Two-phase displacement in Hele-Shaw cells: theory," *J. Fluid Mech.*, vol. 139, pp. 291–308, 1984.
- [57] L. W. Schwartz, H. M. Princen, and A. D. Kiss, "On the motion of bubbles in capillary tubes," *J. Fluid Mech.*, vol. 172, pp. 259–275, 1986.
- [58] J. Ratulowski and H.-C. Chang, "Transport of gas bubbles in capillaries," *Phys. Fluids A*, vol. 1, pp. 1642–1655, 1989.
- [59] M. J. Jensen, *Numerical Simulations of Interface Dynamics in Microfluidics*. PhD thesis, Technical University of Denmark, Department of Micro and Nanotechnology, 2005.

- 
- [60] C. E. Brenner, *Cavitation and Bubble Dynamics*. New York: Oxford University Press, 1995.
- [61] Minivalve International. <http://www.minivalve.com>, Last accessed 16 January, 2009.
- [62] A. Brask, *Electroosmotic micropumps*. PhD thesis, Technical University of Denmark, Department of Micro and Nanotechnology, 2005.
- [63] V. Tvergaard, *Styrkelære: statik og bjælketeori*. Technical University of Denmark: Department of Mechanical Engineering, 2004. Lecture notes.
- [64] U. M. Ascher and L. R. Petzold, *Computer Methods for Ordinary Differential Equations and Differential-Algebraic Equations*. Philadelphia, USA: Society for Industrial and Applied Mathematics, 1998.
- [65] M. R. Spiegel and J. Liu, *Mathematical Handbook of Formulas and Tables*. Schaum's Outlines, NY: McGraw-Hill, 2<sup>nd</sup> ed., 1999.
- [66] K. Witzig, *Über erzwungene wellenbewegungen zaber, inkompressibler Flüssigkeiten in elastischen Rohren*. PhD thesis, University of Bern, 1914.
- [67] C. Kleinstreuer, *Biofluid dynamics: Principles and selected applications*. New York: CRC Press, 2006.
- [68] E. Sternberg, "On the integration of the equations of motion in the classical theory of elasticity," *Arch. Ratio. Mech. Analysis*, vol. 6, pp. 34–50, 1960.